

Contents

1	The Regional and Urban Air Mobility Ecosystem	1
1.1	Introduction	1
1.2	Regional and Urban Air Mobility	2
1.2.1	RUAM Applications	2
1.2.2	Challenges to Realizing a Fully-Integrated RUAM Transportation Ecosystem	3
1.2.3	RUAM Potential Business Cases	5
1.3	Categorizing Electric Aircraft Intended For RUAM Applications	9
1.4	RUAM Mission Specifications and Vehicle Requirements	11
1.5	Chapter Summary	13
2	Aircraft Computational Modeling	14
2.1	Introduction	14
2.2	Code Architecture	16
2.2.1	Energy Networks	18
2.2.2	Mission Structure and Solving	20
2.2.3	Optimization	23
2.3	Computational Analysis Methods and System Component Models	24
2.3.1	Aerodynamics	24
2.3.1.1	Vortex Lattice Method	25
2.3.1.2	Blade Element Vortex-Wake Method	30
2.3.1.3	Airfoil Panel Method	33
2.3.2	Propulsion	37

2.3.2.1	Energy Storage Models	38
2.3.2.2	Rotor Model	38
2.3.2.3	Motor Model	39
2.3.3	Aeroacoustics	41
2.3.4	Physics-Based Weight Estimation	42
2.4	Chapter Summary	43
3	Aircraft Noise Prediction	44
3.1	Introduction	44
3.2	Fundamentals of Sound and Governing Acoustics Equation	45
3.2.1	Governing Acoustics Equation	46
3.3	Frequency Domain Acoustic Formulation	47
3.3.1	Harmonic Noise: Thickness and Loading Noise	47
3.3.2	Broadband Noise: Trailing-Edge Noise	56
3.3.3	Total Vehicle Noise	60
3.4	Computational Model Validation	61
3.4.1	Harmonic Noise	61
3.4.2	Broadband Noise	63
3.4.3	Total Isolated Rotor Noise	64
3.4.4	Comparison of Noise Prediction Approach: Time-Domain vs. Frequency Domain	64
3.5	A-Weighting Noise Metric	66
3.6	Chapter Summary	68
4	Battery Modeling	69
4.1	Introduction	69
4.2	Categorizing Lithium-ion Batteries	70
4.3	Current State of Lithium-Ion Battery Modeling	72
4.4	Electrification Within the Aerospace Industry	75
4.5	Lithium-Ion Battery Modeling for Electric Aircraft Architectures	76

CONTENTS	3
4.5.1 Electrical Discharge/Charge Model	76
4.5.2 Thermal Model	78
4.5.3 Aging Model	84
4.6 Validation of Battery Model	85
4.7 Chapter Summary	86
5 RUAM Aircraft Baseline Studies	88
5.1 Introduction	88
5.2 Electric Aircraft Configurations	89
5.2.1 Vehicle Component Sizing	91
5.2.1.1 Aerodynamics and Stability: Wing Sizing	91
5.2.1.2 Energy Network: Rotor Sizing	93
5.2.1.3 Energy Network: Motor Sizing	94
5.2.1.4 Energy Network: Battery Pack Sizing	95
5.2.2 Aircraft Weight Breakdown	96
5.3 Vehicle Flight Profiles	97
5.4 Assessment of Mission Simulations: Single-Flight Comparisons	100
5.4.1 Battery Pack Performance System	102
5.4.2 Rotor Performance	106
5.4.3 Aerodynamics and Flight Mechanics	108
5.4.4 Noise Footprint	111
5.5 Assessment of Mission Simulations: Extended Operation Comparisons	116
5.5.1 Battery Capacity	120
5.5.2 Maximum Instantaneous C-Rate	122
5.5.3 Maximum Cell Temperature	123
5.5.4 Comparison with Traditional Electric Aircraft Performance Metrics	125
5.6 Chapter Summary	127
6 Design Trade Studies	129
6.1 Introduction	129

6.2	Rotor Design Blade Optimization	130
6.3	The Impact of Rotor Geometry and Performance Parametric on Radiated Noise and Aerodynamic Efficiency Spectrum	132
6.3.1	Parameterization Shape Functions	137
6.4	Lift-Rotor Design	139
6.4.1	Formulation of Lift-Rotor Design Problem	139
6.4.2	Lift-Rotor Design Optimization Results	140
6.5	Prop-Rotor Design	143
6.5.1	Formulation of Prop-Rotor Design Problem	143
6.5.2	Prop-Rotor Optimization Results: Case 1 - Alpha Variation	144
6.5.3	Prop-Rotor Optimization Results: Case 2 - Beta Variation	148
6.6	Mission Simulation Case: Stopped-Rotor EVTOL Aircraft Touch-and-Go Mission	151
6.7	Chapter Summary	155
	Bibliography	156

List of Tables

1.1	UAM destinations in four major metropolitan areas within the U.S.	7
1.2	UAM destinations in four major international cities around the world.	8
1.3	New Vertiport Codes.	9
2.1	X-57 Mod.-II Simulation Parameters.	27
2.2	X-57 Mod. Mod.-III Simulation Parameters.	30
3.1	Parameters for wall pressure spectrum model.	60
4.1	Properties of the Panasonic NCR18650G cell [1].	77

4.2	Geometry and coolant (air) flow conditions of the battery module.	83
5.1	Vehicle parameters.	92
5.2	NMC 18650 cell properties.	96
5.3	Electric aircraft flight segments.	98
5.4	Flight segment kinematics.	100
5.5	Flight profile parameters and engine settings for electric aircraft	101
5.6	Simulation settings and computation times used in electric aircraft noise footprint study	114
5.7	Simulated ranges of the electric aircraft.	119
6.1	Summary of optimized rotor blade characteristics at design conditions for the first prop-rotor design case.	145
6.2	Summary of optimized rotor blade characteristics at design conditions for the second prop-rotor design case.	148

List of Figures

1.1	Dominant challenges of the future regional and urban air mobility ecosystem.	4
1.2	Potential UAM routes in four major metropolitan areas within the U.S.	6
1.3	Potential UAM routes in four major metropolitan areas within the U.S.	8
1.4	Classification of EVTOL configurations.	10
1.5	Design considerations for RUAM aircraft.	12
2.1	High-level SUAVE repository.	17
2.2	Component sub-repository in SUAVE.	18
2.3	Electric aircraft energy networks in SUAVE.	19
2.4	Stopped-rotor EVTOL aircraft mission with reserve leg.	22

2.5	Vortex Lattice Method theory.	26
2.6	X-57 Modification II Aircraft.	28
2.7	X-57 Modification-II Validation.	29
2.8	X-57 Modification III Aircraft.	30
2.9	X-57 Modification-III Validation.	31
2.10	Sectional forces on propeller blade.	31
2.11	Validation of isolated TUD F29 propeller performance for $\alpha = 0^\circ$.	33
2.12	Nomenclature for the analysis by surface singularity distribution [2].	35
2.13	Definition of nodes and panels.	36
2.14	NACA 4412 C_p distribution at $Re = 1 \times 10^5$ for $\alpha = 0^\circ$ and 4°	37
2.15	NACA 4412 trailing edge boundary layer properties at $Re = 1 \times 10^5$ for $\alpha = 0^\circ$ and 4° .	37
2.16	Electric motor model.	40
2.17	Methodology of Fidelity-One aircraft noise computation in SUAVE.	42
2.18	Noise source-observer diagram.	42
3.1	TEXT.	49
3.2	Sound emission reference frames.	54
3.3	TEXT [3]	57
3.4	Local blade section coordinate system.	58
3.5	Comparison of SUAVE prediction with PAS and data for windtunnel test cases [4].	62
3.6	Tonal noise directivity validation study.	63
3.7	Trailing-edge broadband noise validation study.	64
3.8	One-third octave band acoustic spectrum at RPM = 4800.	65
3.9	Noise computation modeling fidelity comparisons.	66
3.10	Text.	67
4.1	Components of a cylindrical jelly-rolled lithium-ion battery cell.	71
4.2	Comparison of lithium-ion battery chemistries [5].	72
4.3	Thevenin Equivalent Circuit.	78
4.4	Comparison of land and air EV battery pack.	79

4.5	Battery module design.	82
4.6	NMC cell validation.	86
5.1	Electric aircraft models.	90
5.2	Weight fractions of RUAM Aircraft.	97
5.3	Flight profile of an ECTOL aircraft.	99
5.4	Flight profile of an EVTOL aircraft.	99
5.5	Altitude profiles of electric aircraft for a single-leg mission.	102
5.6	Vehicle range and battery pack discharge characteristics on board electric aircraft for a single-leg mission.	104
5.7	Battery cell characteristics on board electric aircraft for a single-leg mission.	107
5.8	Rotor performance of electric aircraft for a single-leg mission.	109
5.9	Aerodynamic characteristics of electric aircraft for a single-leg mission.	112
5.10	Stopped-rotor aircraft touch and go scenario.	113
5.11	SPL_{Amax} of electric aircraft for a single-leg mission at microphone location $y = 0 \forall t$	114
5.12	SPL_{Amax} footprint contours of touch-and-go scenarios for electric aircraft.	118
5.13	Battery cell capacity TAPOOL contours of electric aircraft.	121
5.14	Maximum instantaneous C-rate TAPOOL contours of electric aircraft.	123
5.15	Maximum temperature TAPOOL contours of electric aircraft.	124
5.16	Comparison of Aircraft Endurance Trends Using Battery Degradation Modeling and Traditional Electric Range Equation.	127
6.1	Rotor Blade Design. Adapted from Scherer [6]	131
6.2	Rotor blade parameterization shape functions with $c_r = 0.3$ and $c_t = 0.1$. Markers: ■ for $p = 0.25$, ● for $p = 0.5$, + for $p = 1$, ♦ for $p = 2$. Lines: red for $q = 0.25$, green for $q = 0.5$, blue for $q = 1$, black for $q = 1.5$	138
6.3	Objective weight and RPM distribution of optimized rotors.	140
6.4	1/3 Octave-band spectrum comparison of optimized rotor designs.	141
6.5	Comparison of rotor blade designs from $0 \geq \alpha \leq 1$	142
6.6	Optimized rotor blade designs constant β of 0.3.	146

6.7	Geometry of two rotor blade designs. Rotor A (black) with $\alpha = 1.0$, $\beta = 0.3$ and Rotor B (dark red) with $\alpha = 5.0$, $\beta = 0.3$	146
6.8	Performance of two rotor blade designs. Rotor A (black and gray) with $\alpha = 1.0$, $\beta = 0.3$ and Rotor B (dark red and red) with $\alpha = 5.0$, $\beta = 0.3$	147
6.9	1/3 Octave-band spectrums of two rotor blade designs. Rotor A (black) with $\alpha = 1.0$, $\beta = 0.3$ and Rotor B (dark red) with $\alpha = 0.5$, $\beta = 0.3$	147
6.10	Prop-rotor blade designs at constant α of 1.0.	149
6.11	Geometry of two rotor blade designs. Rotor A (black) with $\alpha = 1.0$, $\beta = 0.1$ and Rotor B (dark red) with $\alpha = 1.0$, $\beta = 0.9$	149
6.12	Performance of two rotor blade designs. Rotor A (black and gray) with $\alpha = 1.0$, $\beta = 0.1$ and Rotor B (dark red and red) with $\alpha = 1.0$, $\beta = 0.9$	150
6.13	1/3 Octave-band spectrums of two rotor blade designs. Rotor A (black) with $\alpha = 1.0$, $\beta = 0.1$ and Rotor B (dark red) with $\alpha = 1.0$, $\beta = 0.9$	150
6.14	Touch-and-go noise contour comparisons of stopped-rotor aircraft with two different rotors of $\alpha = 0.0$ (left column) and 1.0 (right column).	152
6.15	Comparisons of system performance of stopped-rotor aircraft with two different rotors of $\alpha = 1.0$ and 0.0.	154

Chapter 1

Regional and Urban Air Mobility

1.1 Introduction

The way in which we perceive commuter transportation, movement of cargo and access to essential services has rapidly evolved over the last two decades. This growth can be attributed to several factors that arise as global economies expand and new markets blossom. To fully appreciate the potential impacts of this work, it is imperative that we understand the motivating factors of this research. In this chapter, we explore these catalysts and how they complement, or sometimes contradict one another. Additionally, this chapter cements the motives behind this research and provide context to the decisions made in subsequent chapters as it pertains to vehicle design and component optimizations carried out.

This chapter is organized into three main sections which collectively, seek to construct a foundation the models developed and studies conducted in this thesis. These sections also provided justification to the parameters chosen for the flight profiles for the aircraft simulated in Chapter 5 as well as the trade-studies preformed in Chapter 6. Below, we begin with a review of the applications followed by a discussion on the most significant challenges that proponents of RUAM have to overcome are provided in Section 1.2.2. Potential business cases for RUAM in domestic and international cities are then summarized with the aide of routed maps to highlight the connection between realistic scenarios and the parameterized routes that are simulated in Chapter 6. This is

followed by a general breakdown the categories vehicles concepts proposed for RUAM services in Section 1.3 along with the a brief summary of the key players in the sector, both large corporate entities as well as small startups, who are presently developing aircraft. Finally, Section 1.4 summarizes high-level requirements that stakeholders, namely governmental agencies and airline businesses have *mostly*¹ agreed upon. These requires are then used to outline high level operating details such as range and cruise altitude.

1.2 Regional and Urban Air Mobility

1.2.1 RUAM Applications

From the turn of the 21st century, RUAM has garnered significant traction. This can be attributed to an assortment of factors; overburdened and under-maintained infrastructure; the lack of real estate upon which to expand roads and railways; a growing concern over greenhouse gas emissions; and the rising passenger dissatisfaction stemming from traffic gridlock. It was therefore not a matter of if but when will RUAM become part of the discussion of future transportation infrastructure within large cities around the world. Thus far, several studies have sought to outline roadmaps for making this a reality. The fraction of these studies that focus on market valuation has attempted to theorize potential applications, identify ideal vertiport locations, estimate total journey and wait times, quantify cost per seat mile, and forecast the point of net-positive profit among others. Specifically on the topic of use cases, Booz Allen Hamilton [7] identified three that have widely been accepted as the most promising. These are: 1) last-mile delivery of packages from local distribution hubs; 2), air-shuttles resembling other transit options such as buses and subways, with regularly scheduled, predetermined routes; and 3), ridesharing air-taxis allowing commuters to request pick-up and drop-off destinations. These views were somewhat amended the recent report by the National Academies of Sciences, Engineering, and Medicine [8] which suggested that due to slow public acceptance, the de facto adopters would be other peripheral applications such as air ambulances, search and rescue missions, surveillance and commercial cargo delivery.

¹The initialization of this workd was purposely done to stress the point that one of the main goals of this thesis is to try and answer the question of how can we construct a more comprehensive and inclusive, yet robust set of requirements for evaluating vehicle configurations

Another study by Goyal et al. [9] utilized Monte-Carlo simulations to study the scale of UAM operations required to realize an annual market valuation of 2.5 billion U.S. dollars. Of course, this rollout is expected to happen in phases over a period of time, first, affording market modelers the opportunity to collect consumer data and secondly, aircraft manufacturers the opportunity to iterate vehicle design while simultaneously expanding production. Furthermore, since the initial cost per mile is expected to be high, the placement of the first set of vertiports must be done judiciously. In response, some studies have integrated gross domestic product per capita into models predicting market growth [10, 11]. Others such as Robinson et al. [12] have factored in climate, urban density, the number of existing airports, traffic congestion and the presence of various economic clusters into the identification of potential locations for launching operations.

1.2.2 Challenges to Realizing a Fully-Integrated RUAM Transportation Ecosystem

Apart from public acceptance, issues concerning aircraft noise, pilot training, the degree of autonomy in the flight controls and the maturity of stored energy systems still linger. These aspects are all closely tracked by investors who are betting on large returns on their investments. Regulatory agencies are also tracking these technical domains, which, to varying degrees, all have an impact on the built and natural environment. Operating between the outer confines of suburbs and densely populated metropolises, ES/VTOL aircraft are expected to offer advantages in both speed and range compared to personal vehicles, rideshare services and public transportation [13, 14]. Despite recent technological advances providing the impetus for realizing regional and urban air mobility (RUAM), questions regarding vehicle design, supporting infrastructure, regulations and societal constraints remain unanswered. These challenges can be hierarchically grouped into the domains illustrated in Figure 1.1. Below, we expand on some of these areas to provide context to the design.

1. **Safety:** From cockpit simulation to vehicle deployment, ECTOL, ESTOL and EVTOL aircraft must demonstrate a level of safety comparable to present-day commuter aircraft of similar weight class, utility and service ceilings. According to the Bureau of Transportation Statistics [15], this equates to less than a 0.85 percent fatality rate. This rate is computed per 100,000 flight hours. As the public has seen with autonomous cars, any mishap or fatal

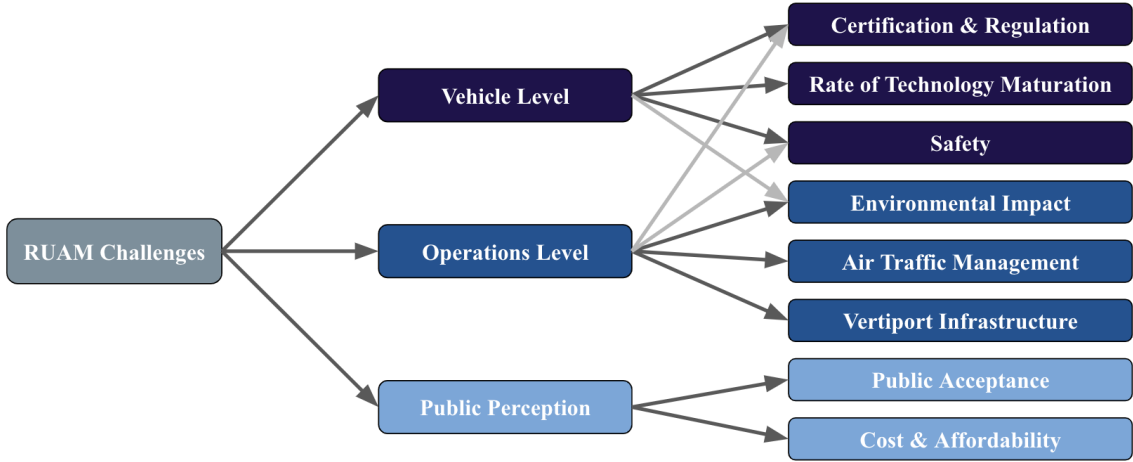


Figure 1.1: Dominant challenges of the future regional and urban air mobility ecosystem.

accident will garner significant attention and retard technology adoption [16].

2. **Rate of Technology Maturity:** This is a significant challenge for aircraft designers as they must factor in technology readiness levels into design methodology to ensure rapid turnaround time between initial concepts and scaled prototypes for flight tests. Examples of such enabling technology include batteries and other stored energy cells, collision detection and avoidance systems, airframe composites and human-assisted control architectures for complex flight maneuvers. Market modelers must also factor in the rate of technology improvement when forecasting earning potential. In this paper, special interest is placed on the energy and power densities of lithium-ion battery cells used in many of the EVs on the market today. The cycle and calendar life of these electrochemical cells also has an impact the long-term operations of electric aircraft. This however is not covered in this study.
3. **Environmental Impact:** Though RUAM aircraft are envisioned to be more eco-friendly than existing aircraft for short-range travel, life-cycle greenhouse gas emissions that encompass generated charging power at the grid will significantly increase. Realizing net reductions in emissions will not only require operations at scale to reach carbon neutrality, but collaboration between service providers and state governments to promote renewable energy. Furthermore, both the perceptive (audible) and psychological (psycho-acoustic) impact of these air vehicles

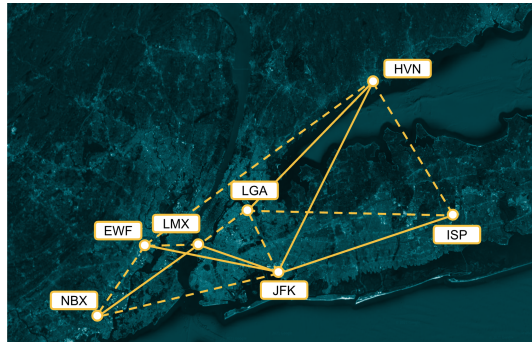
will have to be addressed to reach acceptable levels within residential spaces.

4. **Certification and Regulation:** This process is typically overseen at the national level by aviation authorities such as the U.S. Federal Aviation Administration (FAA) and the European Aviation Safety Agency (EASA) and involves international partnerships to establish policies. However, with prototype vehicles just now starting to emerge, data from UAM operations is sparse. Consequentially, the progress in drafting regulatory policies has been gradual. While regulations related to piloted passenger aircraft could be straightforward to devise, the allocation of Class B, C and G airspace for VTOL operations will be more challenging.
5. **Air Traffic Management:** As urban skies begin to open, RUAM services will start to launch hundreds of vehicles with inexperienced pilots into an already congested airspace with commercial passenger aircraft, rotorcraft for medical emergencies and media and military aircraft operations. Such a scenario will require a complete overhaul of today's air traffic control system to be more coherent and intuitive.
6. **Vertiport and Grid Infrastructure:** Apart from the vehicle itself, the establishment of vertiports to accommodate the high volume of aircraft stand as the single largest undertaking by stakeholders. Urban planning and land-use approval can take upwards of three years and the ensuing development encompassing the transformation of buildings, helipads, airports and unused land to serve as takeoff and landing zones for another five years. Additionally, there will need to be upgrades to grid infrastructure to handle power surges during peak times of the day like rush hour.

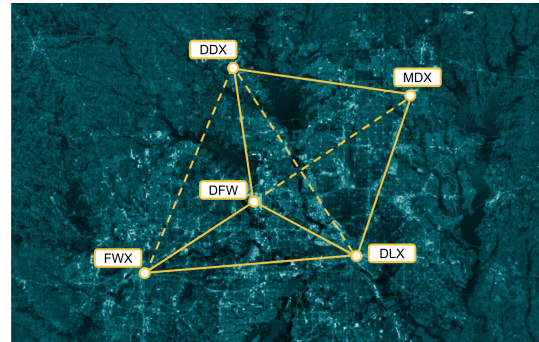
1.2.3 RUAM Potential Business Cases

The report by [7] also identified the potential cities where the first rollout of RUAM operations could occur, four of which are discussed in greater detail in subsequent sections of this paper. In fact, one of these candidates, San Francisco, was also suggested by Antcliff et al. [17] to be an early adopter due to the high percentage of long-distance commuting from peripheral cities such as Stockton, Tracy, and San Rafael to name a few. From a review of some of the aforementioned

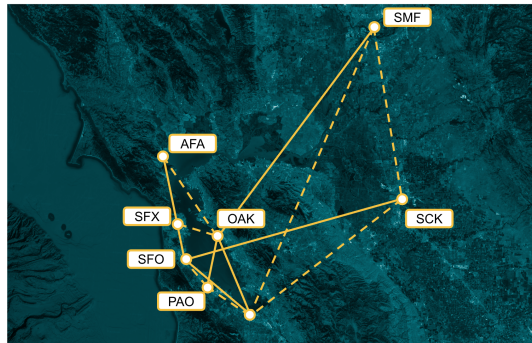
studies, a list of potential routes in four domestic cities is provided in Table 1.1 and four international cities in Table 1.2. With respect to the U.S. cities, though the majority of nodes are of existing airports listed by their three-letter geocode, there are a few, denoted (*) that are new vertiports. These are provided in Table 1.3. Routes within the table are marked as solid lines on Figure 1.2, while other potential routes between nodes are marked as dashed lines. These ranges reflect the gamut of business cases, from regional flights (120–70 nmi) between closely spaced cities such as San Francisco and Sacramento, mid-range (70–40 nmi) flights between polycentric cities like Dallas-Fort Worth, and short-range flights (40–10 nmi) within cities themselves.



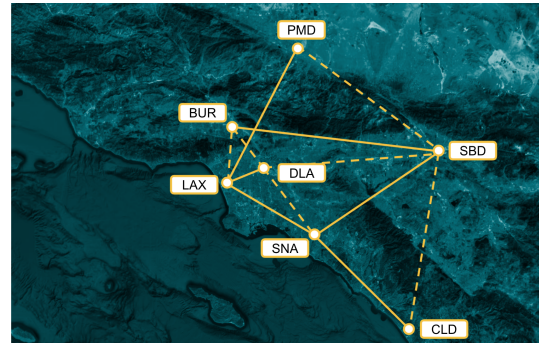
(a) New York Metropolitan Area, NY.



(b) Dallas-Fort Worth Metropolitan Area, TX.



(c) San Francisco Bay Metropolitan Area, CA.

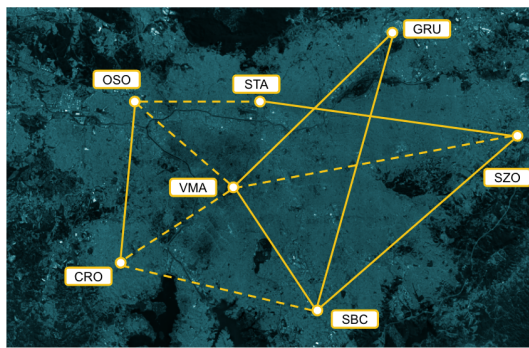


(d) Los Angeles Metropolitan Area, CA.

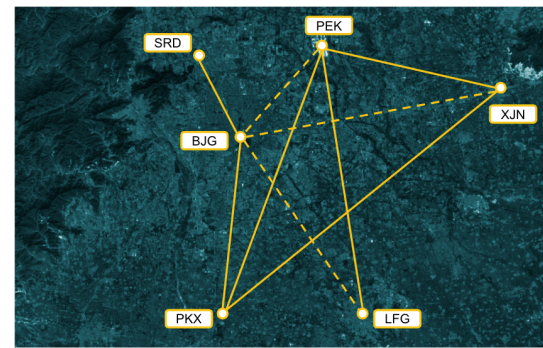
Figure 1.2: Potential UAM routes in four major metropolitan areas within the U.S.

Table 1.1: UAM destinations in four major metropolitan areas within the U.S.

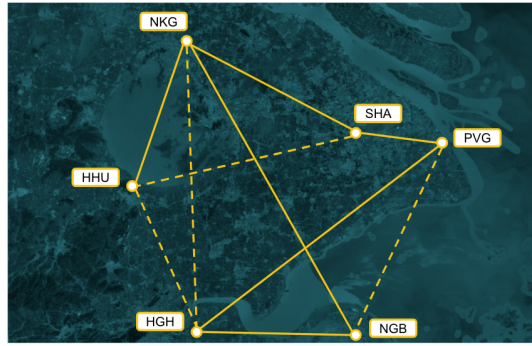
Metropolitan Area	Route	Range (nmi)
San Francisco Bay	SFO - SJC	26
	OAK - SMF	78
	OAK - SJC	26
	PAO - OAK	17
	AFA - SFO	21
	SFO - SCK	56
New York	LMX* - JFK	10
	HVN - LGA	55
	EWF - JFK	21
	NBX* - LMX*	26
	HVN - JFK	50
	JFK - ISP	50
Los Angeles	LAX - SNA	31
	SBD - SNA	41
	BUR - SBD	53
	DLA* - LAX	10
	SNA - CLD	35
	PMD - LAX	44
Dallas - Fort Worth	DLX - DFW	27
	DFW - DLX*	13
	DFW - FWX*	16
	MLX* - DLX*	28
	FWX* - DDX*	37
	MLX* - DDX*	25



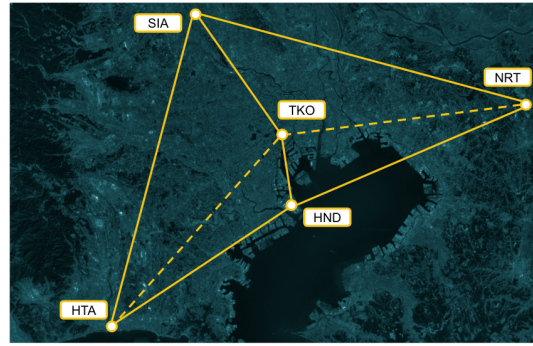
(a) São Paulo Metropolitan Area, Brazil.



(b) Beijing Metropolitan Area, China.



(c) Shanghai Metropolitan Area, China.



(d) Tokyo Metropolitan Area, Japan.

Figure 1.3: Potential UAM routes in four major metropolitan areas within the U.S.

Table 1.2: UAM destinations in four major international cities around the world.

Metropolitan Area	Route	Range (nmi)
São Paulo, Brazil Metropolitan Area	GRU - SBC*	11
	VMA* - SBC*	10
	OSO* - CRO*	15
	STA* - SZO*	22
	GRU - VMA*	15
	SBC* - SZO*	20
Shanghai, China Metropolitan Area	NKG - HHU*	70
	SHA - NKG	77
	NKG - NGB	131
	HGH - PVG	102
	PVG - SHA	27
	NGB - HGH	66
Beijing, China Metropolitan Area	SRD* - BJJ	23
	PEK - PKX	41
	PEK - LFG*	39
	BJG* - PKX	26
	PKX - XJN*	60
	PEK - XJN*	42
Tokyo, Japan Metropolitan Area	SIA - HTA	40
	HND - HTA*	28
	TKO* - HND	10
	TKO* - SIA*	15
	NRT - SIA*	42
	HND - NRT	29

Table 1.3: New Vertiport Codes.

Metropolitan Area	Vertiport	Vertiport Code
Domestic		
Los Angeles	Downtown Los Angeles	DLA
New York	Lower Manhattan	LMX
	New Brunswick	NBX
	Downtown Dallas	DLX
Dallas-Fort Worth	Denton	DDX
	McKinny	MDX
	Downtown Fort Worth	FWS
International		
Sao Paulo, Brazil	C��pao Redondo	CRO
	Vila Marina	VMA
	S��o Bernardo do Campo	SBC
	Osasco	OSO
	Suzano	SZO
	Stantana	STA
Shanghai, China	Hangzhou	HHU
	Langfang	LFG
Beijing, China	Downtown Beijiing	BJG
	Xijiecun	XJN
	Shangdi Residential District	SRD
Tokyo, Japan	Downtown Tokyo	TKO
	Saitama	SIA
	Hiratsuka	HTA

1.3 Categorizing Electric Aircraft Intended For RUAM Applications

The three main categories for vehicles put forth for RUAM are electric conventional takeoff and landing (ECTOL), electric short takeoff and landing (ESTOL) and electric vertical takeoff and landing (EVTOL) aircraft. ECTOL aircraft require standard length runways (for that weight class), implying that their applicability where the destination is space-constrained is limited. These aircraft are therefore expected to operate between pre-existing airport infrastructure [18]. With significantly shorter takeoff distances ranging between NUMBER and NUMBER, ESTOL aircraft should grant the flexibility of operation at newly constructed vertiports. However, in referring to the many

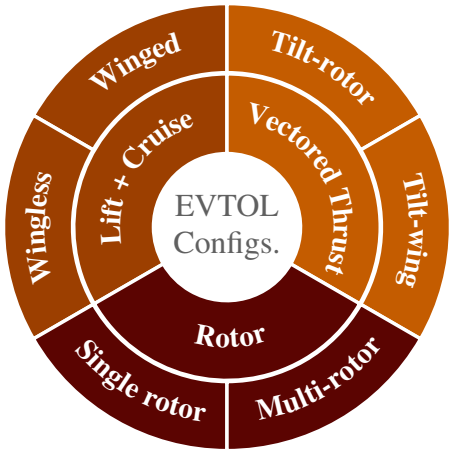


Figure 1.4: Classification of EVTOL configurations.

studies that point to rooftops [CITE](#) and mass transit stations [CITE](#) being the most practical locations, it can be said that ESTOL aircraft would be incapable to achieve safe egress. This has lead designers primarily focusing on EVTOLs for RUAM applications for which the takeoff footprint is comparable with a helicopter.

Though there is an infinite number of possibilities for the configuration of an EVTOL, these aircraft can be grouped into three categories based on their distinctive propulsive networks and flight dynamics as shown on the inner ring of Figure 1.4. The thrust-generating system on these aircraft can be ducted fans, open rotors, prop-fans, or a combination thereof. As noted by Moore [19], many concepts attempt to leverage the scale-invariant nature of electric propulsion to distribute propulsors around the airframe, offering substantial benefits to control authority and weight-distribution compared to traditional internal combustion engine (ICE) or turbine-driven propulsion. Secondly, compared to ICEs, electric motors have a wider RPM envelope in which near-optimal torques and efficiencies can be maintained, reducing the cost that comes with the complexity of variable pitch rotors [20].

Lift+cruise EVTOLs have separate systems for the vertical climb and forward thrust. The transition between hover and cruise is managed through the coaction of these two propulsive networks. In this study where the lift+cruise vehicle solely possess rotors, it is customary to demarcate rotors intended for forward flight as propellers while those intended for vertical flight, lift-rotors.

Vectored-thrust EVTOLs, which include tilt-wing, tilt-prop and tilt-fan aircraft use the same propulsion system for hover, transition and cruise. Should this class of EVTOLs have rotors, they are typically referred to as prop-rotors to signify the dual-purposing of the rotating blade. This multi-purposing of a single propulsive network oftentimes leads to compromises in performance even in the presence of gearboxes or variable pitch mechanisms. It must also be mentioned here that both lift+cruise and vectored thrust EVTOLs can be wingless or have wings for more efficient cruises. The third major classification is rotary-wing EVTOLs, which can be further subdivided based on the number of main lift-rotors, that is, single or multi-rotor. Despite possessing attractive VTOL characteristics, these aircraft are limited in airspeed by the speed of the advancing blade speed in edgewise flight. To reduce vehicle footprint for all three of the aforementioned configurations, VTOL designers may opt for coaxial rotors to achieve thrust requirements. This nonetheless comes at the expense of aerodynamic efficiency.

propellers (rotors intended for forward flight) and lift rotors (rotors intended for vertical flight) and prop-rotors

1.4 RUAM Mission Specifications and Vehicle Requirements

Analogous to the preliminary design stage of conventional tubular and wing aircraft, the development of RUAM aircraft must be preceded by the establishment of operation specifications and performance requirements needed to generate revenue once introduced into the market. Adapted from Straubinger [21], Figure 1.5 identifies these factors, shaded to signify the degree of importance. That is, the major requirements are shaded dark gray, design drivers in gray and external boundary conditions in light gray. Unlike the original diagram in the reference, noise is promoted from an external boundary condition to a major requirement to emphasize this metric as a pivotal factor in VTOL certification.

In accordance with Uber's landmark study in 2016 [13], an upper threshold of 67 dBA at ground level from an EVTOL at **250** ft altitude is used as an evaluation criterion despite being omitted in the sizing in this present study. With respect to range, the battery was sized to facilitate a two-leg mission without intermediate recharging as suggested by Patterson [22]. The target range of each

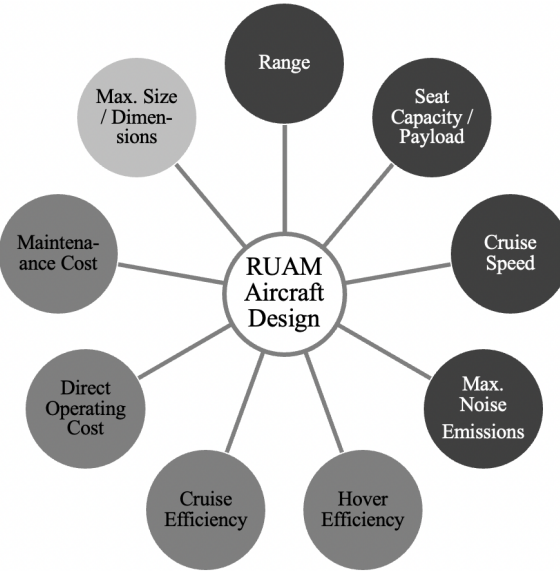


Figure 1.5: Design considerations for RUAM aircraft.

leg of the mission was 70 nmi, however as we will discover in subsequent sections, achieving such a range is vehicle configuration specific. An additional battery reserve constraint was included to demonstrate the ability of the aircraft to reroute in the event of an emergency. The four aircraft are designed to accommodate a maximum capacity of 6 passengers or an equivalent payload of 925 lbs, with cruise speeds between 75 mph and 175 mph depending on the configuration. Preliminary sizing was carried out before flight profile simulations to ensure that the winged aircraft were capable of achieving an L/D around 15 at cruise. To ensure that the aircraft can fit within the confines of proposed designs of both elevated rooftop and ground vertiports in suburban areas, a maximum allowable wingspan permitted was 50 feet. Despite being larger than the standard helipads defined in AC 150/5390-2C [23] with a touchdown and liftoff area (TLOF) of 30 ft, a larger area can be justified given the fact that: 1) Most of the proposed concepts UAM have wings which exceed this maximum radius and; 2) the documented sizing requirements is based on the rotor diameter of the reference design vehicle and is therefore impractical for EVTOL aircraft which typically possess rotors whose diameters are roughly an order of magnitude smaller. Lastly, the impact of chemical state changes that occur within the battery cell from repeated operations, the broader implications of fleet charging and the cost of maintenance to aircraft are not factored into vehicle design in this

study. They however will be an integral part of future life-cycle studies.

1.5 Chapter Summary

Chapter 2

SUAVE: A Conceptual Tool Enabling Computational Design, Analysis and Optimization

2.1 Introduction

The birth of the modern computer enabling mathematical computational has brought about several engineering feats within aerospace engineering from numerical simulation to design optimization. Since the early 60's where engineers employed the first forms of computed aided design and finite element analysis to design internal load-bearing structures around the airframe to the use of potential flow methods to compute aerodynamic properties, the use of computational tools has always been a cornerstone of aircraft design. Over the years, as computer memory increased and processing speeds improved, these early methods became easier and easier to implement and researchers began to tackle more difficult problems[24]. For example, researchers began to develop numerical method to calculate the flow fields of transonic airfoils and wings using inviscid computation fluid mechanics (CFD) methods [25–27]. The tools of today are now able to authoritatively examine several domains of interests such as aerodynamics, structures, acoustics. Moreover, not only is the assessment of individual disciplines possible, but their interactions with one another,

for example, fluid-structure interaction, have become commonplace. Ultimately, the ability of the modern computation tools to examine full aircraft configurations has led to them being adopted in early-stage conceptual design. With resurgence in interest in supersonic passenger air travel, new ideas around unmanned aerial systems, and the recent focus on on-demand short-range commuting, the need for tools parametrizing, analyzing, and optimizing novel vehicle configurations has been evident more than ever. However, on surveying the landscape of existing design tools, it is evident that there is a need for analysis capabilities for non-conventional configurations. Many of the current software tools for aircraft conceptual design, such as NDARC, PASS, TASOPT and FLOPS, rely upon empirical correlations and other low-fidelity approximations for the propulsion and power systems as well as the architecture of the airframe [28]. These limitations make them incapable of handling vehicles with non-tube-and-wing planforms and novel powertrain systems. This is even more true in the 21st century where resurgent interest in supersonic air travel and short-range, on-demand commuted has called for the development of tools capable of parameterizing, analyzing, and optimizing new vehicle configurations.

Initially developed in 2014 under the NASA LEARN Phase I program, SUAVE is a python-based aircraft conceptual design tool intended to address many of the shortcomings of its predecessors. SUAVE possess a modular code architecture in that simulations are constructed by first specifying then appending data structures to construct vehicles and analysis methods. This modularity also allows the designer to surgically access specific computational models as well as granting the designer freedom of choice in modeling fidelity. The latter implies that the designer has a direct say in the computational suite of tools used to assess a component or the entire aircraft, in so doing leaving them with the decision of computational speed vs. accuracy. Taking aerodynamics as an example, the lift generating from a surface could be computed using high fidelity, physics-based methods such as CFD using SU2, medium-fidelity potential-flow based methods such as a vortex lattice method (VLM), or lower fidelity correlative models based on historical data.

Since its early days, SUAVE has gone under a significant transformation. More physics-based models have been implemented to modern systems on board novel aircraft as well as to provide better estimates of aerodynamic loads, vehicle stability and noise. For instance, propeller-wing interaction models have been integrated to the performance of DEP aircraft concepts. Similarly, wing

vortex lift, wave drag and n-wave sonic boom And evanescent wave prediction methods have been implemented to study supersonic delta-wing aircraft. Indeed, advances to the code have enabled the implementation of multi-fidelity methods used in design optimization optimization [29, 30] .

Following the success of SU2 [31], an open-source CFD code also developed by the Aerospace Design Laboratory, SUAVE was released to the research community as an open-source code. This decision has proven to be advantageous for several reasons. Increased adoption by government entities, industry and academic institutions has fostered a community that is constantly pushing code developers to make improvements, address bugs and add new analysis capabilities. Secondly, it has lead to faster adoption by new users as commonly encountered problems are discussed in a forum settings therefore reinforcing the concept of group learning. Last but most importantly, the accessibility to frequently commonly used physical components models and computational methods that have been previously validated [32] circumvents mistakes that could arise from having to rewrite functions, in the process reducing design time. Users can therefore concentrate on developing new methods or assessing the performance of particular quantities or components of interest.

The majority of the improvements to the code over the past three years are geared towards studying EVTOL aircraft. These new methods and models are accordingly discussed in the following sections of this dissertation. Section 2.2 first documents the architecture of code and how functions, data structures and modules are laid out. This includes a discussion on the types of propulsion networks that can be modeled and how missions are constructed and solved. A closer look at the computational methods that were improved to assess EVTOL aircraft is the taken in 2.3. This includes an overview of the improvements to the analysis methods as well as models used to simulate physical components such as electrical motors and batteries. Chapters 3 and 4 are dedicated to in depth discussions of aircraft noise and lithium-ion batteries respectively so only a brief overview is provide in this chapter.

2.2 Code Architecture

SUAVE serves as the simulation platform to assess both the component-level and system-level attributes of the aircraft modeled in Chapter 5 and the subsequent trade studies of optimized rotors

in Chapter 6. From its conception, SUAVE was designed not just as another aircraft design tool with improved capabilities, but a tool meant to stand the test of time, a feature not shared by its predecessors. This was made possible through a few distinguishable characteristics that has enabled its longevity. First was the choice of python as the coding language. Constantly under development this high-level general-purpose programming language is both attractive to inexperienced coders due to its readability as well as experienced coders that take advantage of the plethora of advanced numerical libraries that can execute seemingly large mathematical operations relatively cheaply. The second distinguishable feature is the modular nature of the code and how analysis functions, the properties of components and the atmosphere, subroutines for discipline analyses, supporting number-crunching operations among others are arranged into repositories that can be easily assessed without getting entangled in "code spaghetti". Figure 2.1 below depicts this organization and conveys how easy it is for new users navigate to desired modules through parsing pythonic objects.

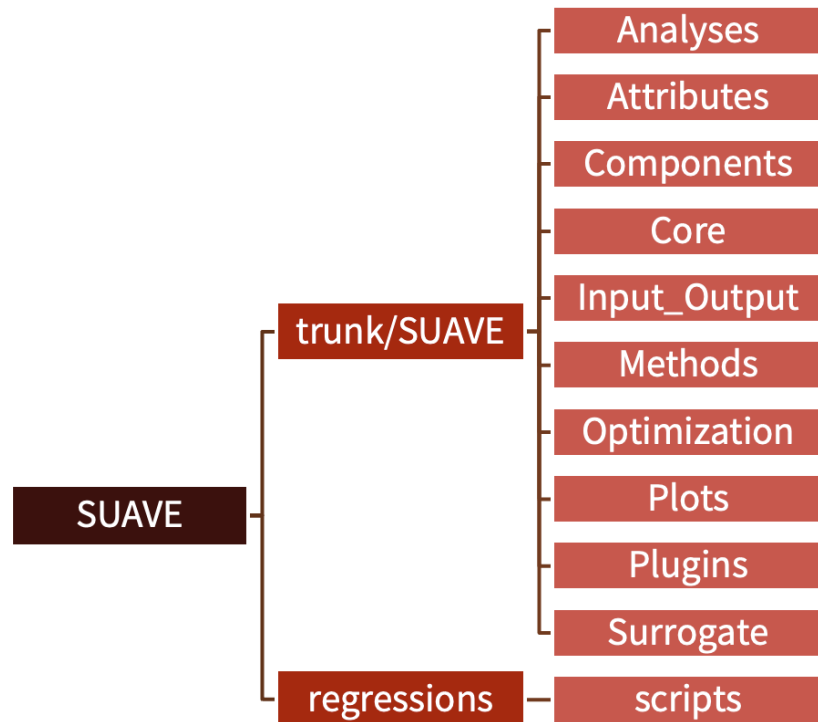


Figure 2.1: High-level SUAVE repository.

SUAVE possesses custom data structures that enable the designer to append, access and manipulate aspects of the vehicle, flight conditions and computational methods used to evaluate performance. One of these unique data structures worth mentioning here is the *Data* class, a pythonic structure that allows the designer to compute a vehicle, component or sub-component from all of its parametric and performance characteristics into one callable object. Moreover, *Data* can be used to create a hierarchy. For example, each segment of the flight profile contains information organized into data structures including *Analyses*, *Conditions*, *Settings* and *Numerics* making it easy to parse. Another example is depicted in Figure 2.2 where the *Data* class is also used almost exclusively to construct a full vehicle made up of physical attributes that are defined as classes and conveniently named for generalization. These classes include wings, propulsion networks, nacelles, fuselages and other lofted bodies. Furthermore, these classes themselves may contain sub-classes defining other components.

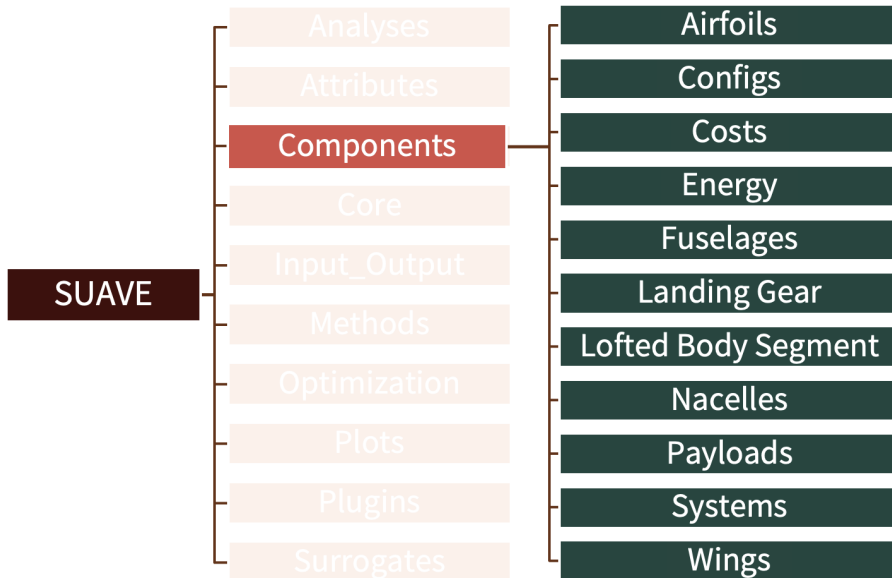


Figure 2.2: Component sub-repository in SUAVE.

2.2.1 Energy Networks

The flight simulations discussed in subsequent chapters adopt some of the new propulsion architectures that enable VTOL capability. SUAVE can accommodate a plethora of energy and power

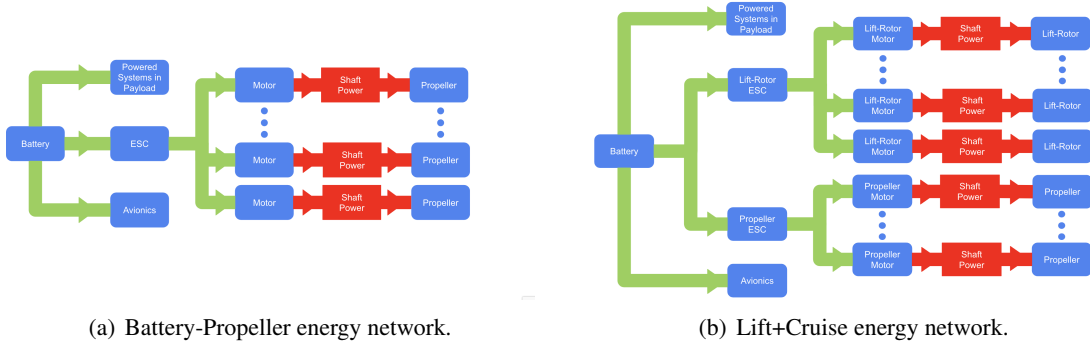


Figure 2.3: Electric aircraft energy networks in SUAVE.

sources, including combustible aviation fuel, batteries, solar panels, and fuel cells. It can also accommodate several energy converting machines such as motor and turbines. The grouping of components that propel the aircraft forms what is referred to as “energy network”. The code however does have a collection of predefined energy networks which come standard to the code , alleviating the task of the designer to conceptualize a new network from scratch. Examples of these energy networks include the *Turbofan* network, *Internal_Combustion_Engine* network, the *Battery_Propeller* network and the *Lift_Cruise* energy network. In this work, the latter two are used in the creation of creation of the electric aircraft modeled. The *Battery_Propeller* network class contains the rotor, battery, motor and electronic speed controller components and is used in this work to generate the ECTOL and tandem tilt-wing and multi-rotor EVTOL aircraft. The stopped-rotor EVTOL aircraft on the other hand uses the *Lift_Cruise* network. This energy network has separate propulsion sub-systems for vertical flight and forward cruise, but rely on the synergy of these networks to perform transition maneuvers. The differences between these two energy networks are illustrated in Figure 2.3. On the left, the current/voltage interactions between the motor and battery system in the *Battery_Propeller* linear for network, whereas the *Lift_Cruise* network on the right experiences a tandem draw of power from the battery to power the two sets of motors.

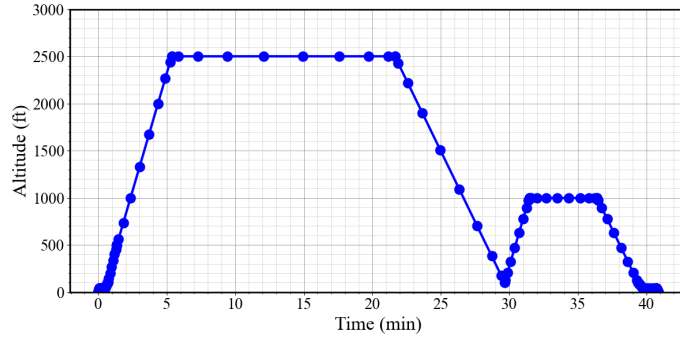
The level of component model fidelity can also vary from simple application of system efficiencies to account for losses to physics-based models that capture such loses in constituting components themselves through conservation equations. For instance, the battery pack can be modeled as

a lumped mass with a specified energy density or built up from individual battery cells in production today. Of course, the prior is suited for early stage conceptual design when the designer is not interested in the fine details of the system but rather the overall feasibility of a particular design. The latter however offers valuable insight into cell temperature which is crucial for ensuring safe operation. During flight simulations, the energy network takes as inputs values from the mission solver as well as outputs from different discipline analyses, and returns the thrust, vehicle mass change rate, and other properties to the mission as necessary. The conservation of mass, energy, and current are maintained by the energy network object.

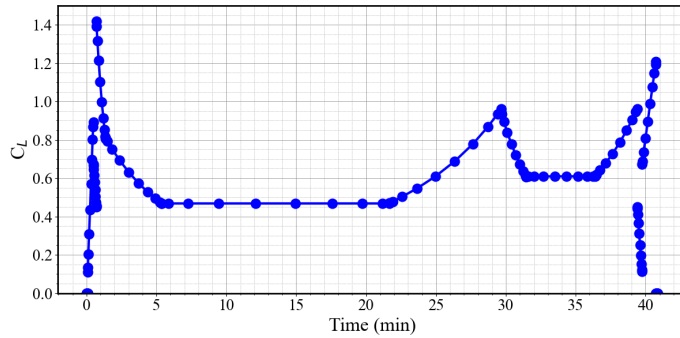
2.2.2 Mission Structure and Solving

A mission in SUAVE is composed of flight segments that define the position and motion of the aircraft. An entire flight profile is constructed by stitching together various segments that can define a climb, cruise, loiter or final descent of the vehicle. With many types of segments defined in the *missions* module, very intricate flight profiles can be defined. An example of a mission is shown in Figure 2.4, where a stopped-rotor EVTOL aircraft performs an descending approach maneuver, vertical land, vertical takeoff and lastly a departure maneuver where the vehicle climbs to cruising altitude. More importantly, this figure conveys that the mission does necessarily have to start from ground, but anywhere, enabling the designer to examine isolated events. Each segment is composed of pseudo-spectral control points in time and space where the forces, moments and other conservation equations unique to the energy network are resolved simultaneously. The mission solver, which takes as inputs this system of equations, is designed to allow the aircraft to operate in such a manner that is most efficient at each control point. This implies that numerical convergence can be challenging depending on the initial conditions or whether the rigid-body problem is well-posed and bounded. Oftentimes, choosing reasonable values for initial conditions is sufficient for the root-finding algorithm in the mission solver to arrive at an optimal set of state variables, for example, angle of attack, propeller RPM, battery current and cell temperature. A poorly designed component however, such as an aircraft with insufficient wing area to produce the required lift, or a low motor speed constant that results in the inability to generate the required RPM will manifest in

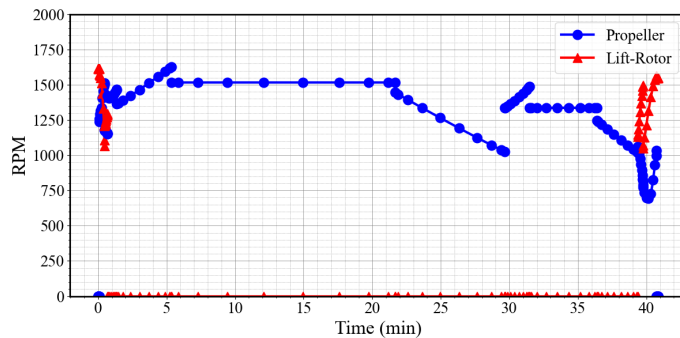
the failure of the mission solver to converge due to the absence of a feasible solution. This garbage-in-garbage-out philosophy that SUAVE adopts forces the designer to pay considerable attention to component parameterization in the simulation setup.



(a) Text.



(b) Text.



(c) Text.

Figure 2.4: Stopped-rotor EVTOL aircraft mission with reserve leg.

2.2.3 Optimization

The rotor blade design discussed in Chapter 6 were carried out using SUAVE’s native optimization framework called the Nexus. Originating from the Latin verb “nectere”, meaning “to bind”, the Nexus can be thought of as the glue that connects core elements of the SUAVE code, that is, vehicle parameterization, analysis methods, flight conditions, among other relevant data structures to external optimization packages that are integrated into the software. SUAVE functions as a black box through which the Nexus updates parameters and queries sensitivities to arrive at a solution. The Nexus is also capable of handling both single and nested optimization tasks as well as concurrently employing numerous fidelities of analysis. This makes it ideal for aircraft conceptual design where a designer may choose to use simple correlative models for certain aspects but resort to high-accuracy, memory-intensive simulations for studying quantities of interest. During each function evaluation in the optimizer, there is a flow of information through the Nexus framework. Upon initialization, outputs from the optimizer are fed into the SUAVE “black box”. Objective function evaluations and if applicable, constraint violations, are then passed back to the optimizer via the Nexus.

Several wrappers have been developed to facilitate both gradient-based and gradient-free optimization in the Nexus framework. For instance, gradient-based optimizers like SciPy’s SLSQP, pyOpt, pyOptSParce and IPOPT are would be better suited for convex problems. One the other hand, for multi-modal problems where the presence of several local minima, Particle Swarm Optimization which uses momentum accelerate convergence or the Differential Evolution optimizer, a genetic algorithm-based algorithm.

Similar to other modules in SUAVE, the Nexus inherits from the Data class with executable methods. It contains the problem set-up for optimization, the vehicle configurations, the analyses, the mission and the results. Configuring the Nexus therefore requires a series of files that require setup prior to initiation the optimization routine. The first of which is the *Optimization.py* file that defines the objective function, constraints, design variables, including their initial values and bounds. The second file is the *Analyses.py* file that contains computational methods used to evaluate the performance. The next file is the *Vehicle.py* file which contains parameterizes either the full vehicle or isolated component to be modified. Forth is the *Missions.py* file where the atmospheric

properties, flight conditions and operating settings are defined. Last is the *Procedure.py* file which comprises user-defined functions unique to the optimization problem. These functions include those that modify the object each iteration before analysis, evaluate constraint violations and compute objective functions that are passed back to the optimizer via the Nexus network.

2.3 Computational Analysis Methods and System Component Models

The following sections document the computational approaches employed in this thesis to assess both the overall aircraft performance as well as the performance of isolated components on-board the aircraft. This is not an extensive overview of SUAVE's capabilities, rather a discussion on those that are directly used to analyze electrical aircraft. The following are discussed below: methods for computing aerodynamic loads, methods for predicting electric powertrain performance including empirical models to simulate energy storage and discharge, methods for acoustics noise prediction and weight estimation models. Also covered in this section are analysis capabilities for evaluating mass properties of the aircraft including their component weight breakdowns. Collectively, these methods for the core of the mission solver which couples flight physics with conservation questions to predict aircraft performance at each control within each segment of the mission.

2.3.1 Aerodynamics

Since the early days of SUAVE, there have been continual improvements and broadening of its aerodynamics capabilities. At the highest level of fidelity, the development of a python-wrapper for the SU2 code written in C++ has made the investigation of sophisticated flow regimes on lifting surface as well as certification by analysis possible. In terms of medium-fidelity, the interface with AVL [33] and the new improvements to the vortex lattice method native to SUAVE have allowed for design optimization due to its robustness but speed. At the lowest level of modeling fidelity, the lifting-line and AERODAS [34] models have provided a means for estimating aerodynamic loads of simple planforms and estimating post-stall performance respectively. These various levels have led to the code reaching its full potential when it comes to multi-fidelity design and optimization. Discussed in the succeeding sub-sections below are three of these methods: SUAVE's VLM,

the Blade Element-Vortex Theory Method for prediction rotor blade loads and the vectorized 2D-panel method code. These three methods are extensively utilized throughout this body of work for prediction both aerodynamic and aeroacoustic quantities. for aircraft and rotor blade.

2.3.1.1 Vortex Lattice Method

SUAVE's new VLM formulation based on the VORLAX code is used to compute the aerodynamic forces on all surfaces on the vehicle. This includes primary lifting surfaces, control surfaces and lofted bodies such as fuselages, nacelles and boom. Despite again earning the classification of a medium-fidelity analysis method, it is capable of producing reasonably accurate predictions when compared to higher fidelity methods when benchmarked against experimental data. VLMs are based on lift-line theory whereby the velocity induced at a point C by a vortex filament of length dl is determined using the Biot-Savart law provided in Equation 2.1a and illustrated in Figure 2.5(a). In the VLM formulation, wings are modeled as flat surfaces along the mean camber line and are discretized into panels. Each panel possess a horseshoe vortex made up of a bound vortex at the $\frac{1}{4}$ chord location on the panel and trailing legs that extend to infinity behind the panel. The control point where aerodynamic loads are computed is located at the $\frac{3}{4}$ chord location of each panel as shown in Figure 2.5(b). The total induced velocity on a control point m on the wing is determined by numerically integrating the influence of the entire system of horseshoe vortices on the wing as given by Equation 2.1b.

$$d\vec{V} = \frac{\Gamma_n (\vec{dl} \times \vec{r})}{4\pi r^3} \quad (2.1a)$$

$$\vec{v}_m = \sum_{n=1}^N \vec{C}_{m,n} \Gamma_n \quad (2.1b)$$

where N is the total number of control panels on the lifting surface. An aerodynamic influence coefficient matrix is constructed from the regular lattice and solved by applying boundary conditions representing flow tangency on each panel to find the strength of the circulation and subsequently the lift and induced drag. This matrix, $C_{m,n}$, depends on the geometry of the n^{th} horseshoe vortex

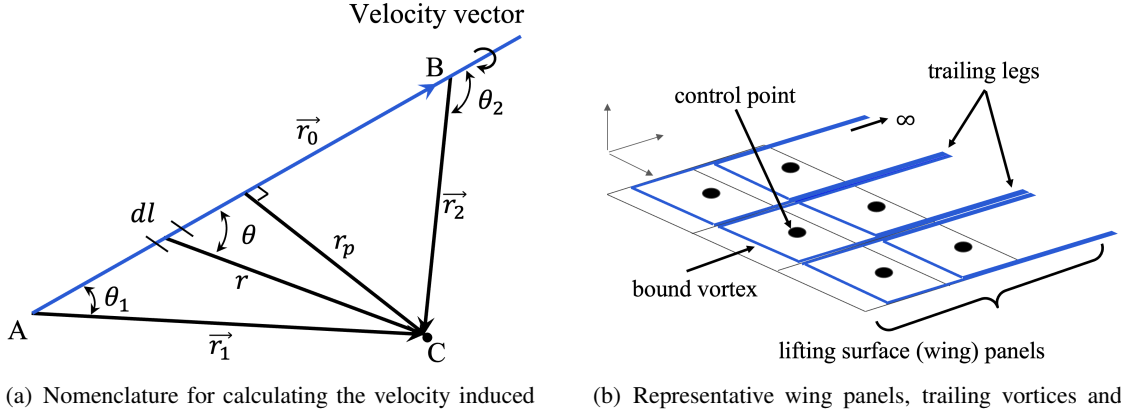


Figure 2.5: Vortex Lattice Method theory.

and its distance from the control point of the m^{th} panel. Katz [36] and Bertin [35] provide well-documented implementations of this method and will therefore not be discussed in further detail here. Integrating the forces over the entire vehicle and then normalizing by some reference area gives the inviscid aerodynamic coefficients characterizing the aircraft. Semi-empirical correlations are then applied to these non-dimensional coefficients to estimate viscous and compressibility effects on the vehicle. Corrections to the lift coefficient at high angles of attack as well as details concerning the calculation of parasitic and compressible drag components are outlined in [28].

Recent publication documenting SUAVE's VLM [32] not only reveal the exceptional range its capabilities, in terms of the design problems and flight conditions the VLM is equipped to handle, but sheds light on the areas where this method underperforms. The studies conducted in this paper range from the NASA Common Research Model (CRM), the second and third modification configurations of NASA X-57 Maxwell, a supersonic biconvex wing, a medium range airliner, the PROWIM [37] propeller-wing configuration, and the Onera M6. For both pure subsonic and supersonic flight, SUAVE's Aerodynamic Fidelity Zero Module which uses the VLM shows excellent agreement with experimental data and high fidelity analyses. Areas of caution are transonic cases with high lift, as SUAVE over-predicts drag and under-predicts lift. This is due to shockwave formations not fully captured. Another area of concern is where separation is present, such as in high angle of attack flight regimes and around the nacelles in the NASA X-57. In this thesis, all models

Table 2.1: X-57 Mod.-II Simulation Parameters.

Parameter	Value	
Vehicle Geometry		
Reference Area	m^2	14.76
Center of gravity [x,y,z]	m	[3.23, 0.0, 0.77]
Mean Aerodynamic Chord	m	1.19
Span	m	11.4
Test Conditions		
Case 1		
Angle of attack sweep	deg.	-2 – 12
Mach Number	-	0.3
Reynolds Number	-	0.6×10^6

examined have open-rotor powertrains, suggesting that strong helical wakes and tip vortices are generated. To reduce computation time of aerodynamic loads, this blown-wing effect is omitted from the analysis at the expense of accuracy. For this reason, only the relevant X-57 Maxwell validation studies are presented here here.

The first validation case was on the Modification-II variant (see Figures 2.6) that has one propulsor mounted on each wing around the mid-span while the second was on the Modification-III variant (see Figures 2.8) of NASA's X-57 Maxwell that possesses a higher aspect ratio wing with wing-tip mounted propulsors and high-lift nacelles for the integration of a distributed electric propulsion powertrain system. In the VLM analysis, the vertical section of the fuselage is omitted in the VLM panelization while control surface discretization for the second set of comparisons is included as their effectiveness is studied.

In this first case, the clean vehicle geometry was benchmarked against experimental data obtained from wind tunnel experiments by Nicolosi et al. [38] on a 1:6.5 scale wooden model. Properties of the computational domain were also modified to emulate comparable experimental test conditions with Reynolds numbers around 0.6×10^6 . Moreover, as the VLM is inherently an inviscid prediction tool, it is incapable of modeling flow separation at high angles of attack. As a result, high angles of attack were not examined. Table 2.1 summarizes the high-level parametrization of the Modification-II (Mod.-II) as well as the test conditions used for the purposes of reproducing the findings presented.

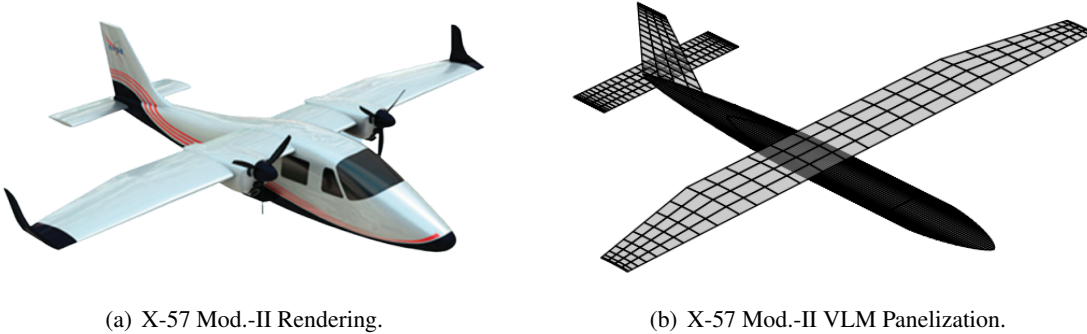


Figure 2.6: X-57 Modification II Aircraft.

Generally speaking, great agreement was found between SUAVE’s aerodynamic analysis routine and the experimental data. In the case of the lift curve slope in Figure 2.7(a), the computational predictions fall within 5% of wind tunnel measurements up to an angle of attack of 7° . After which, an expected overprediction of the lift coefficient is observed. The VLM however slightly underpredicts the zero-lift angle of attack as shown in the plot. The linearized drag polar in Figure 2.7(b) on the other hand highlights a more significant discrepancy between the measured and predicted drag, particularly at low angles of attack. Between a lift coefficient of 0 ($\text{AoA} = -2.5^\circ$) and a lift coefficient of 0.7 ($\text{AoA} = 7.1^\circ$), there is an underprediction of drag by as much as 100 drag counts when the aircraft is pitched nose-down. Predictions within the region of the curve where this aircraft is expected to operate are closer to the experimental data and do point to the VLM being suitable for providing more than sufficient estimates for aerodynamic loads in a full mission.

In the second validation study the VLM was compared to CFD simulations taken from Yoo and Duensing [39]. Their study utilized two Reynolds-averaged Navier-Stokes (RANS) flow solvers: STAR-CCM+, a commercial code, and Launch Ascent Vehicle Aerodynamic (LAVA), which is a code developed and maintained by NASA Ames Research Center. In this paper, however, only the results of STAR-CCM+ which solves the RANS equation in finite-volume, cell-centered formulation are provided. Using this commercial code, the inviscid fluxes were discretized using the second-order Roe flux-difference splitting scheme. Additional information about the solver, turbulence model and preconditioning can be found in the reference. Here we assess the performance

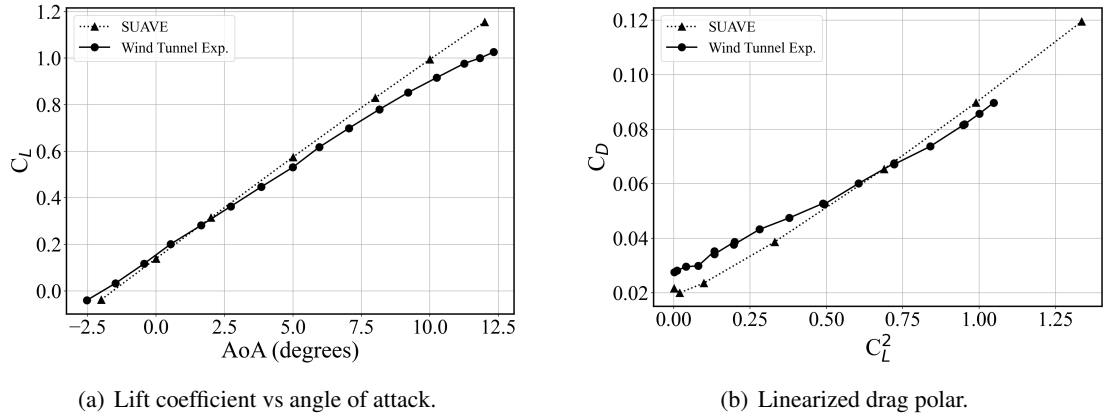


Figure 2.7: X-57 Modification-II Validation.

of the SUAVE's VLM for two flap-deflection angles, cruise (0°) and takeoff (10°). The aircraft itself is designed to be a configuration with a blown wing, and has a higher aspect ratio with nacelles distributed along the wingspan. Those at the wingtips are for mounting larger propellers for efficient cruises while the smaller ones inboard are for high-lift flight regimes such as takeoff and cruise. Again, the high-level geometric parameters and flight conditions used in the simulations are documented in Table 2.2.

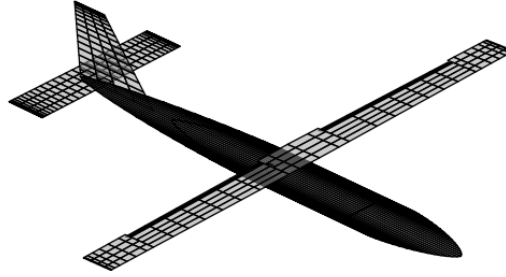
Similar to the twin-engine case, there is a close agreement of the predicted lift coefficient of both the undeflected and deflected flap cases up to about 8° angle of attack where flow separation dominates, particularly on the upper surface of the wing. This separation is computed by the CFD solver and is seen in Figure 2.9(a) by the gradual attenuation of lift as the angle of attack increases. There is also an underprediction of total drag at low angles of attack, more than likely attributed to nacelles on the wing that have a non-negligible contribution to the profile drag of the aircraft. On the other hand, the higher predicted drag coefficient in Figure 2.9(b) past an angle of attack of 10° is believed to be a result of the overprediction of lift-induced drag. These findings highlight areas in which the code can be improved, notably with the inclusion of a stall model that corrects inviscid aerodynamic predictions and an improvement of profile drag estimates of non-lifting bodies such as boom, nacelles and fixed landing gear systems.

Table 2.2: X-57 Mod. Mod.-III Simulation Parameters.

Parameter	Value	
Vehicle Geometry		
Reference Area	m^2	6.13
Center of gravity [x,y,z]	m	[3.35, 0.0, 0.34]
Mean Aerodynamic Chord	m	0.65
Span	m	9.64
Test Conditions		
Case 1		
Angle of attack sweep	deg.	-2 – 18
Mach Number	-	0.233
Reynolds Number	-	1.32×10^6
Flap Deflection	deg.	0
Case 2		
Angle of attack range	deg.	-2 – 18
Mach Number	-	0.233
Reynolds Number	-	1.32×10^6
Flap Deflection	deg.	10



(a) X-57 Mod.-III rendering.



(b) Drag coefficient vs angle of attack.

Figure 2.8: X-57 Modification III Aircraft.

2.3.1.2 Blade Element Vortex-Wake Method

The aerodynamic loads and non-dimensional coefficients characterizing the performance of rotors are computed using a Blade Element model coupled with a Vortex Wake formulation by Drela [40]. Such an approach is appealing for conceptual design because of its speed and accuracy when compared to experimental data and high-fidelity simulations. Determination of loads first begins with a discretization of the rotor blade quasi two-dimensional airfoils as shown in Figure 2.10 and

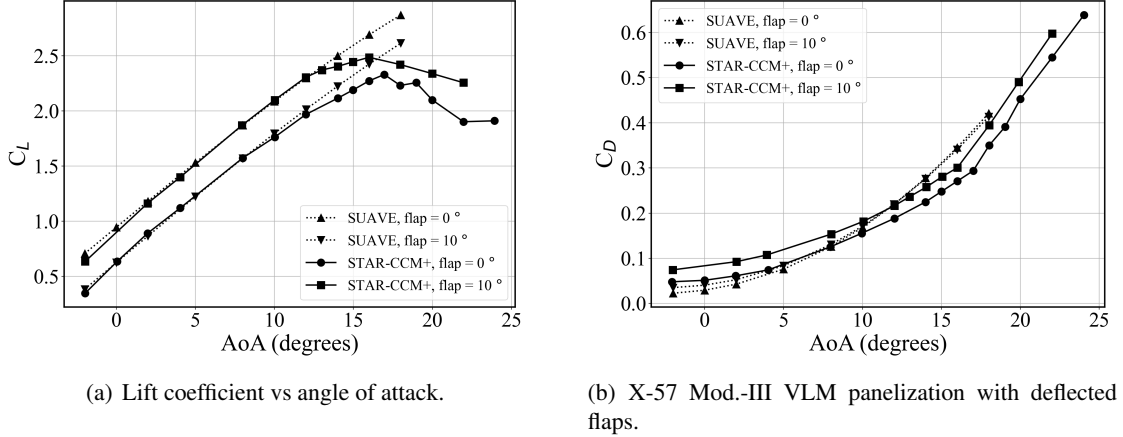


Figure 2.9: X-57 Modification-III Validation.

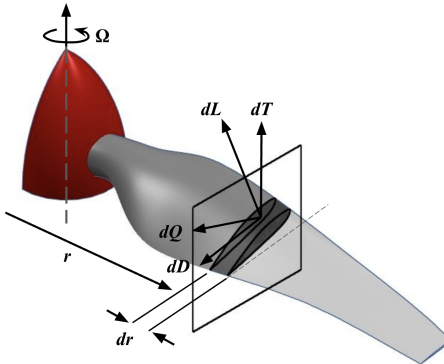


Figure 2.10: Sectional forces on propeller blade.

characterized by a radial location, r , twist angle, chord and sweep (mid-chord alignment). The circulation at each blade element located at a radius r along the blade is determined from the Kutta Joukowski theorem which is then equated to the circulation computed from Helmholtz's theorem, using the tangential swirl velocity associated with the torque imparted on the fluid by the rotor. These two representations for circulations are provided in Equations 2.2a and 2.2b below. A Newton iteration is used to converge on the inflow angle, driving the residual between these equations to zero.

$$\Gamma = \frac{1}{2} W c C_l \quad (2.2a)$$

$$\Gamma = \frac{4\pi r}{N_B} \bar{v}_l = \frac{4\pi r}{N_B} \left(v_t F \sqrt{1 + \left(\frac{4\lambda_w R}{\pi N_B r} \right)^2} \right) \quad (2.2b)$$

In the BEVT formulation, the inflow velocities imparted by the wake model are included in the total local velocities seen by each blade section. Blade element forces can now be evaluated at the local Reynolds number and angle of attack by querying pre-built surrogate models of these force coefficient. These surrogate models are generated using XFOIL [41] at a range of Reynolds numbers relevant to the rotor and operating conditions. An intermediate post-processing step to extend the range of the surrogate is carried out prior to sampling. This step applies post-stall corrections based on the empirical correlations by Spera [34] to raw coefficient data obtained from XFOIL. The force coefficients at each radial and azimuthal station are therefore functions of the local properties,

$$C_l, C_d = f(\alpha, Re, Ma, a_{geo}). \quad (2.3)$$

The sectional lift and drag components are subsequently decomposed into components parallel and perpendicular to the freestream to acquire differential thrust and torque on the blade

$$dT = dL \cos \Psi - dD \sin \Psi \quad (2.4a)$$

$$dQ = (dL \sin \Psi + dD \cos \Psi)r, \quad (2.4b)$$

where Ψ is the local inflow angle. Prandtl tip loss and hub loss factors are also applied the final radial distributions to account for 3D effects. Finally, these loads are integrated along the blade from hub to tip to obtain the total thrust and torque of a rotor.

The implemented BEVT model, referred to as (VW) in Figure 2.11 was validated against experimental data and other propellers models that included a prescribed vortex wake(PVW) model and a vortex particle method (VPM) model [42]. Here, a comparison of the isolated propeller in

an axially uniform freestream flow is evaluated at a range of advance ratios. For the BET model, the number of radial blade elements, N_r , and azimuthal stations, N_a , was selected to be 30 and 72, respectively, with a spline interpolation fit between the known airfoil sections. The PVW shape was generated over six propeller rotations while the approximately 6 propeller rotations using the VPM were required to form a reaching a fully developed near-wake state, with 72 time-steps per rotation. Comparing the three wake methods, it is observed that that for an isolated propeller, the use of a simplified vortex wake model is sufficient for predicting performance, corroborating prior findings by Gur and Rosen [43] As we do not consider interactions between lifting surfaces in this work, this model was deemed acceptable and is used throughout this work

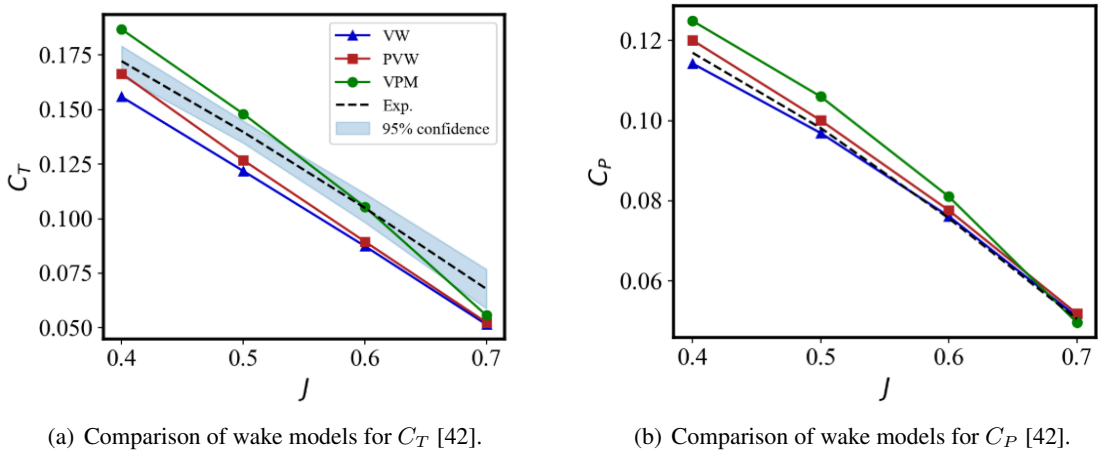


Figure 2.11: Validation of isolated TUD F29 propeller performance for $\alpha = 0^\circ$.

2.3.1.3 Airfoil Panel Method

In the BEVT model, the creation and storing of lift and drag coefficient surrogate models significantly reduces the computational of determining the aerodynamic loads on the blade. These models are simply queried each the Newton iteration at the control points of a given flight segment in a mission. In theory, the raw data that goes towards building these surrogate models can be sourced from a variety of places: CFD, thin airfoil theory, potential flow method such as a panel method code as discussed in the previous section. Of course, depending on the method being used, boundary layer properties on the surface of the blade can also be computed. These properties are used to compute the

pressure spectrum model used to determine trailing edge broadband noise outlined in Chapter 3.

The use of CFD is one option to acquire such properties, but this would take enormous amounts of time to automatically generate a mesh, perform mesh refinement, initialize flow conditions, then solver for the properties of the blade. Even if this process were accelerated by the reducing mesh resolution, the computed properties would be nowhere near accurate. A more viable alternative is a panel code coupled with empirical models for predicting boundary layer properties on pseudo-2D airfoil sections on the blade. This brings us back to the through of using XFOIL which would be ideal had it not been for the code's inability to be efficiently automated - each airfoil section on of each rotor blade of each rotor must be evaluated separately because it experiences a unique operating condition. Moreover, even if a wrapper were efficiently build around this FORTRAN-based code, the the input/output (I/O) bound interface that reads written output files of the code is slower than CPU-bound tasks. This ultimately led to the creation of a python-based panel method code that addressed these shortcomings among others.

First and foremost, the developed framework can compute the aerodynamic forces and boundary layer properties of unique airfoils simultaneously at separate flight conditions, that is, angle of attack and Reynolds number, implying that the entire lifting surface, be it a wing or rotor blade can be characterized at once. Secondly, there is guaranteed convergence. A significant drawback of using XFOIL is that if the user-specifies a high angle of attack as the first evaluation point, the code fails successfully converge and return boundary layer properties. This can be attributed to the fact that the code uses previously computed angles as initial conditions to arrive at aerodynamic and boundary layer properties at ore extreme angles. If a poor initial condition is provided, the code fails to converge. For example, to compute the properties of an airfoil at an angle of attack of 10° requires the computation of the properties of the same airfoil at an angle of attack of 9° , which requires properties of an angle of attack of 8° , and so forth. The result is the cumbersome task of unnecessarily computing several results which takes up computing time and RAM. The vectorized panel method code developed in this work guarantees convergence without initialization and is capable of computing aerodynamic and boundary properties. Additionally, because it is written in python, tasks are solely CPU-bound, alleviating the need to perform inefficient and memory intensive operations such as importing, exporting, reading, and writing files.

The panel method implemented here is based on Hess and Smith [44] begins like any other panel method where the surface of the airfoil is first discretized into panels where elementary panel is designated one or more types of singularity distributions such as sources, vortices and doublets. Here, sources and vortices are used, where potential at a given point is expressed as:

$$\phi = \phi_\infty + \phi_S + \phi_V, \quad (2.5)$$

where ϕ is the total potential function and its three components are the potentials corresponding to the freestream ϕ_∞ , the source distribution ϕ_S , and the vortex distribution, ϕ_V . These last two distributions have locally varying strengths $q(s)$ and $\gamma(s)$, where s is an arc-length coordinate that spans the complete surface of the airfoil. The potentials created by the distribution of sources and vortices are given below where the various quantities are defined in the Figure below.

$$\begin{aligned} \phi_S &= \int \frac{q(s)}{2\pi} \ln r ds \\ \phi_V &= - \int \frac{\gamma(s)}{2\pi} \theta ds, \end{aligned} \quad (2.6)$$

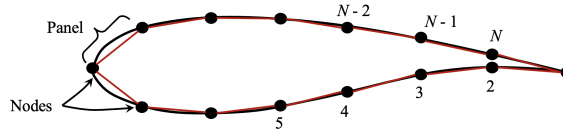


Figure 2.12: Nomenclature for the analysis by surface singularity distribution [2].

This integration is carried out along the surface of the airfoil. Per Hess and Smith's approach, the vortex strength is assumed to be constant over the whole surface of the airfoil while the source strength is allowed to vary from panel to panel so that, together with the constant vortex distribution, the flow tangency boundary condition is satisfied everywhere. Using the panel decomposition depicted in Figure 2.13. We can discretize Equation 2.5 in the following way:

$$\phi = V_\infty(x \cos \alpha + y \sin \alpha) + \sum_{j=1}^N \int_{\text{panel}_j} \left[\frac{q(s)}{2\pi} \ln r - \frac{\gamma}{2\pi} \theta \right] ds \quad (2.7)$$

Since the vortex strength was considered to be a constant, we only need to solve for $N + 1$

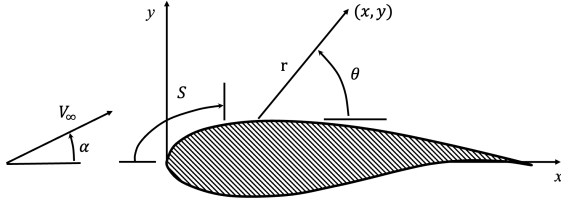
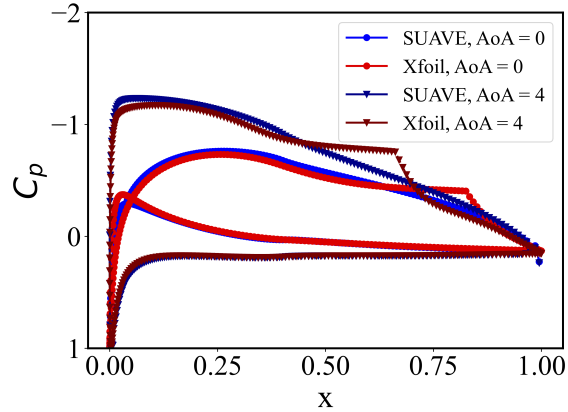
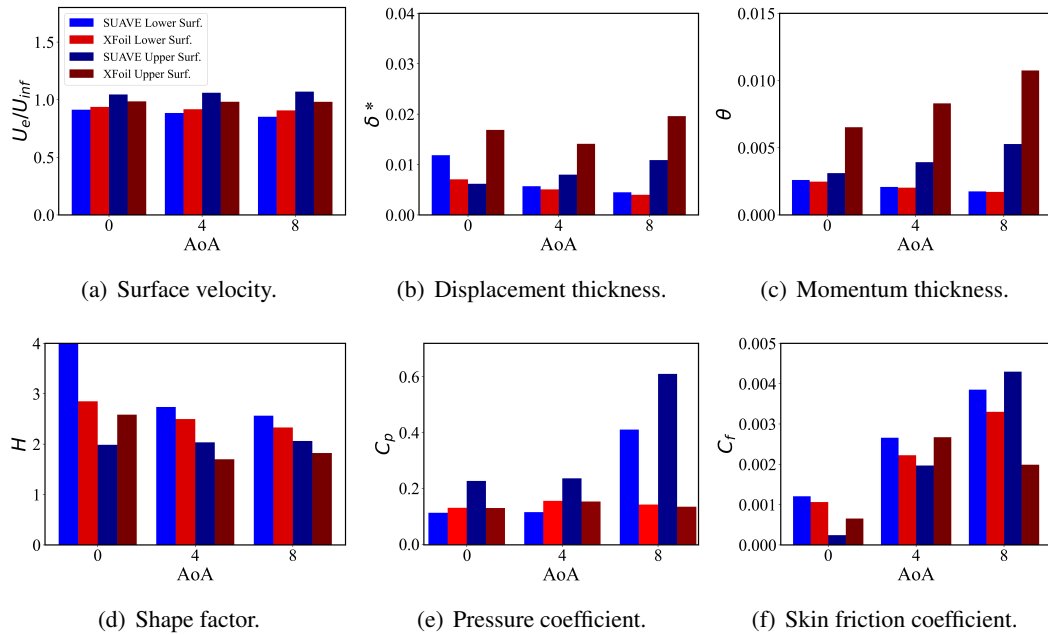


Figure 2.13: Definition of nodes and panels.

unknowns - the N panel source strengths q_i and the constant vortex strength γ . Consequently, we will need $N + 1$ independent equations which can be obtained by formulating the flow tangency boundary condition at each of the N panels, and by enforcing the Kutta condition that the flow leaves the trailing edge of a sharp-tailed airfoil smoothly; that is, the velocity is finite there. The midpoint of each of the panels are used to impose the Kutta condition as well as flow tangency boundary condition. Though it suffers from a slight alteration of the surface geometry, the panel method easy to implement and yields fairly accurate results for a reasonable number of panels.

Once the pressure distribution and local velocity distribution on the surface of the airfoil are determined. Integral momentum equations that characterize the boundary layer are applied to determine quantities of interest. Here, Thwaites' Method [45] is used to characterize regions of laminar flow while Head's method [46] is in turbulent flow regimes. Michel's criterion [47] was chosen as the transition criterion between the two flow regimes. Illustrated below is a comparison of boundary layer properties computed using this new approach with XFOIL. First, in Figure 2.14 we observe relative close agreement of local pressure about the airfoil. As XFOIL employs a different transition criterion – the e^n method – we do not expect a perfect match of results. This can be seen on the upper surface of the airfoil where there is a departure near the transition of the airfoil between $0.5 < x < 0.75$. Everywhere else, partially at the trailing edge where our attention is focused on, producing similar results. A comparison of the remaining boundary lower properties is provided in Figure 2.15. This includes surface velocity U_e/U_{infty} , displacement thickness, δ^* , momentum thickness, θ , shape factor, H , local skin friction coefficient, c_f and local pressure coefficient c_p at the trailing edge of the airfoil.

Figure 2.14: NACA 4412 C_p distribution at $Re = 1 \times 10^5$ for $\alpha = 0^\circ$ and 4° Figure 2.15: NACA 4412 trailing edge boundary layer properties at $Re = 1 \times 10^5$ for $\alpha = 0^\circ$ and 4° .

2.3.2 Propulsion

The following sub-section described the main components of the *Battery_Propeller* and the *Lift_Cruise* networks chosen for electric aircraft design in this body of work, Auxiliary components such as the electronic speed control, gearboxes and avionics instrumentation are simple integrated

into the networks either system efficiencies or static loads and are therefore not discussed extensively here.

2.3.2.1 Energy Storage Models

Central to any electric propulsion architecture is the energy source. For practical applications, this can either be in the form of batteries or fuel cells. In SUAVE there are several types of batteries that the user can choose from. These include the constant mass cell types such as lithium-ion and lithium-sulfur as well as variable-mass cells like lithium-air batteries that gain weight during operation as chemical reactions result in the formation of byproducts [48]. For the lithium-ion class of battery cells, there also exists a choice in modeling fidelity. The designer can either assume the battery pack is one large lumped mass comprised of small individual cells. This ability to choose fidelity level is extremely helpful when moving from preliminary sizing to detailed design. Within this thesis, the latter is selected to model lithium-ion batteries. This will however not be discussed in great detail here as it is extensively covered in Chapter 4. That being said it is working discussing for completeness within the confines of the propulsion model section of this chapter.

2.3.2.2 Rotor Model

The mission solver seeks to drive the set of equations that define the motion of the aircraft and interactions of the components of the powertrain of the vehicle. For the two energy networks used in this thesis, the rotor-motor matching equation is the conservation equation of interest. Here, we seek to match the propeller the motor output and rotor input. To do this we require that the shaft torque and rotation rates of the motor and rotor are equal. This BEVT methodology implicitly assumes axis-symmetric inflow into the rotor disc making it suitable for the ECTOL and lift+cruise EVTOL. For the vectored-thrust EVTOL, the use of this model can be justified if we assume that the transition phase of the flight is slow enough such that the tangential component of the freestream velocity incident on the disc plane is small in comparison to the axial component. For the multi-rotor configuration, however, this is not necessarily the case as edgewise flight dominates. Here, the half of the lift-rotor where the blade is advancing will have greater lift than the retreating side where the blade is moving in the direction of the freestream. Despite the presence of a semi-prescribed vortex

wake model in SUAVE capable of more accurately predicting aerodynamic loads in edgewise flight, the BEVT model was preferred in this study due to better numerical convergence and computing speed. Small inaccuracies in the estimation of aerodynamic loads on the rotor for the multi-rotor aircraft are therefore expected. Once the thrust, torque and power are determined at a given RPM and flight condition, the non-dimensional coefficients can be computed as follows

$$C_T = \frac{T}{\rho n^2 D^4} \quad (2.8a)$$

$$C_Q = \frac{Q}{\rho n^2 D^5} \quad (2.8b)$$

$$C_P = \frac{P}{\rho n^3 D^5}, \quad (2.8c)$$

where

$$n = \frac{\omega}{2\pi}.$$

The propulsive efficiency of converting shaft power to thrust is given below is used in the rotor-motor matching within the mission solver.

$$\eta_p = \frac{P_{thrust}}{P_{shaft}} = \frac{Tv}{Q\omega}. \quad (2.9)$$

2.3.2.3 Motor Model

The motor model used in this study is a simple brushed direct current motor model, void of the losses in latency that alternating current motors suffer from when switching signs as the internal commutator brushes keep the magnetic fields aligned in the desired phase with the magnets. Shown in Figure 2.16 is a combined illustrative and electrical circuit model. Given the motor speed constant K_v , no-load current I_0 , internal resistance R_0 , and the applied voltage V , the torque and power supplied to the propeller at a particular rotation rate can be computed as follows:

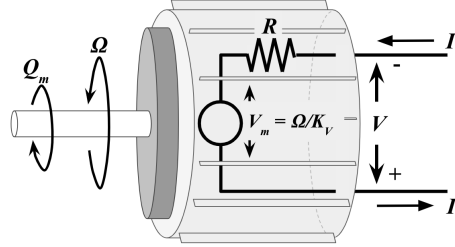


Figure 2.16: Electric motor model.

$$Q_{mot} = \frac{(I - I_0)}{K_v} \quad (2.10a)$$

$$\Omega = (V - I_m R_0) K_v \quad (2.10b)$$

$$P_{\text{shaft}} = Q_{mot} \Omega \quad (2.10c)$$

$$= (I - I_0)(V - I_m R_0). \quad (2.10d)$$

The efficiency of converting electric energy to mechanical energy is given by:

$$\eta_{mot} = \frac{P_{\text{shaft}}}{P_{\text{elec}}} = \frac{Q_{mot} \Omega}{IV} = \left(1 - \frac{I_0}{I}\right) \left(1 - \frac{IR_0}{V}\right). \quad (2.11)$$

In the presence of gearbox efficiency losses represented by η_G and a gear ratio, G , matching the load required by the propeller to the load supplied by the motor resulting in the derivation of motor parameters as functions of the current and terminal voltage. Starting with the manipulation of Equation 2.10a to derive an expression for motor current, I , then substituting into Equation 2.10d for an expression of shaft power yields:

$$P_{\text{shaft}} = \left[\left(V - \frac{\Omega}{K_{v_e}} \right) \frac{1}{R_0} - I_{0e} \right] \frac{\Omega}{K_{v_e}} \quad (2.12)$$

where

$$I_{0e} = I_0 + I(1 - \eta_G) \quad (2.13)$$

$$K_{ve} = \frac{K_v}{G}. \quad (2.14)$$

This is solved for the rotation rate and motor torque by setting the power of the motor equal to the power required by the propeller or rotor to arrive at

$$\Omega = \frac{(\pi^{3/2}) \left((-16C_p I_{0e} \rho K_{ve}^3 R^5 R_0^2 + 16C_p \rho V K_{ve}^3 R^5 R_0 + \pi^3)^{0.5} - \pi^{3/2} \right)}{8C_p K_{ve}^2 R^5 R_0 \rho} \quad (2.15a)$$

$$Q = \left(\frac{V - \frac{\Omega}{K_{ve}}}{R_0} \right) - I_{0e}/K_{ve}. \quad (2.15b)$$

In the above expression, C_p is a vector of power coefficients obtained from the propeller model ran prior in the mission solver at each flight segment. Additionally, it is assumed that the motors are connected in parallel, implying that $V_{UL_{bat}} = V$.

2.3.3 Aeroacoustics

In SUAVE, the computation of noise is executed as a post-processing step at the end of each segment. Once the aerodynamic loads on rotor blades, pressure distributions on the surfaces of the aircraft and propeller wake are obtained at each control point, the acoustic signature of the aircraft is constructed. Having this done outside the mission-solving routine significantly reduces the computation time of analyses. The implemented model expanded upon in greater detail in Chapter 3 forms the basis of SUAVE’s new Fidelity-One Noise Analysis approach – Fidelity-Zero Noise Analysis uses empirical correlates from Shevell [49] while Fidelity-Two under development couples SU2 with an Ffowcs-Williams and Hawkins (FWH) acoustic pressure solver. Outlined in Figure 2.17 below, the methodology for determining the overall sound pressure level using this approach is iterative, meaning that the potential to parallelize processes exists.

In this framework, only the noise from rotors is considered – noise generated from unsteady wake interactions, wing loading and fuselage interference is not modeled. As shown in Figure

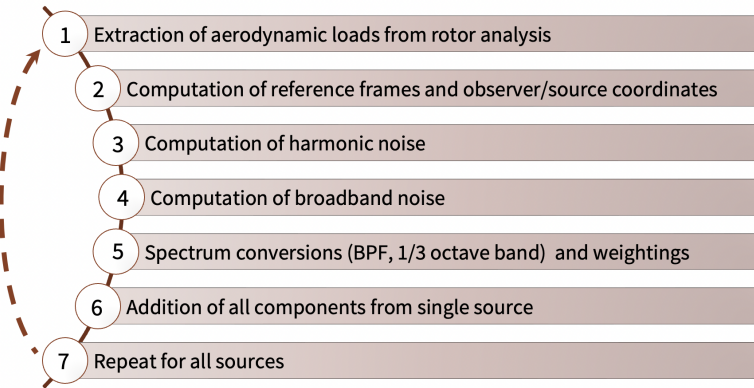


Figure 2.17: Methodology of Fidelity-One aircraft noise computation in SUAVE.

2.18(a) the noise at each observer is computed through decibel addition of all sources around the vehicle. The observer locations where the sound is computed are fixed in the inertial frame on the x-y plane beneath the aircraft as depicted in Figure 2.18(b).

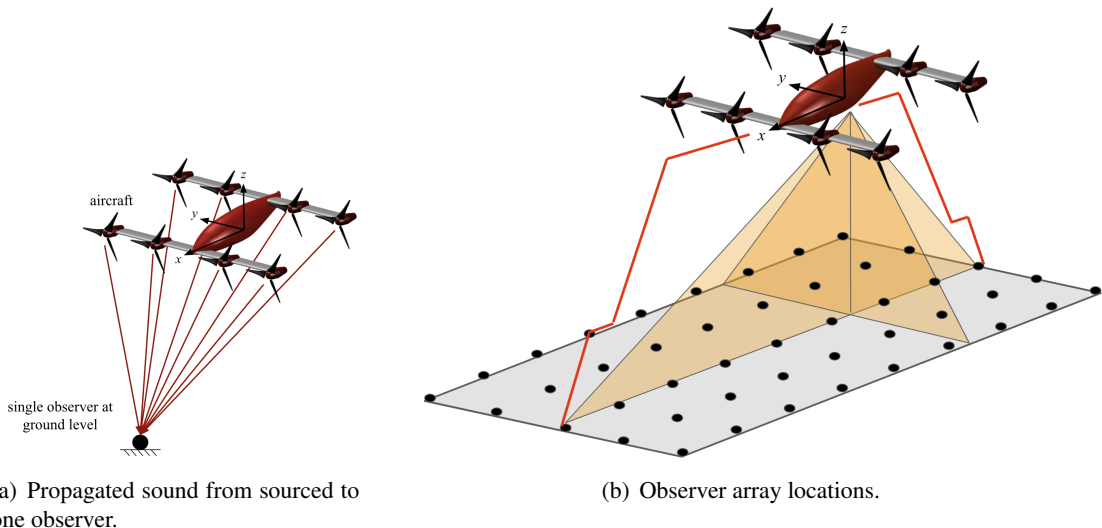


Figure 2.18: Noise source-observer diagram.

2.3.4 Physics-Based Weight Estimation

Takeoff gross weight (TOGW) is a critical design parameter to consider in the evaluation of mission feasibility. This is especially true for aircraft with VTOL capability where distributed weight

not only dictates initial vertical climb but transition maneuverability of the aircraft. For conventional aircraft, historical data and high-level geometry parameterizations may be sufficient to directly ascertain component weights from the regression. For emerging eVTOLs, these historical correlations fail for several reasons listed by Smart [50]. It was therefore necessary to use a more physics-based approach. With the exception of motors and smaller avionic systems, this current study utilizes a component-by-component, loading-driven weight build-up of the vehicle weight implemented in SUAVE. The authors will refer the reader to the code repository on GitHub [51] for the full description of this methodology. This flexible build-up method considering novel classes of vehicles rely on projected aerodynamic loads, material properties and safety criteria to drive the sizing of components. This approach also grants the ability to incorporate new information as it emerges.

2.4 Chapter Summary

Chapter 3

Medium-Fidelity Aircraft Noise Prediction

3.1 Introduction

The idea of having large numbers of vehicles operate air shuttling and cargo delivery services at low altitudes has not come across without justifiable push back, particularly when it comes to the foreseeable impact on noise pollution. From the psychoacoustic effect associated with cognitive dissonance of seeing many aircraft, to the increase in perceived noise levels, the livelihoods of entire communities are at risk of serious disruption. One can therefore argue that in future RUAM ecosystems around the world, noise exposure levels will dictate the approach and departure of air corridors within densely populated areas. Noise will also be an integral factor in vertiport placement, effectively changing traffic patterns of ground transportation networks.

After dropping the ball on vehicle certification that lead to a large exodus of small UAS and drone companies from US markers in the early 2000s, the National Aeronautics and Space Administration (NASA) and the Federal Aviation Administration (FAA) are attempting to move away from the lengthy, bureaucratic practices that have come to define these agencies and adopt faster, more streamlined approaches that would more collaboration with both the private sector and academia. These partnerships will focus on all aspects of aviation, including infrastructure, air traffic systems,

aircraft flight handling and autonomy, vehicle design and performance, market analyses, policy creation, flight and ground testing, flight control system development, and of course, safety. Specifically looking at aircraft noise, some of these efforts have begun to examine how the application of computational noise prediction tools can complement, and even potentially inform certification processes. Unlike the early tools that could only predict the noise from isolated rotors, new tools will need to be developed that are capable of assessing non-conventional distributed propulsion architectures that radiated sound from multiple sources. Moreover, these novel tools must be able to analyse aircraft perform the new maneuvers proposed within urban canyons.

Presented below is the implementation of an inexpensive approach capable of accomplishing such a feat, enabling fast prediction, iterative design and ultimately design optimization. This chapter is broken into four main sections. Section 3.2 reviews the major sources of aerodynamically generated sound, as well as the two computational approaches to predict noise spectra. Section 3.3 then provides formulations for the components of noise for the approach chosen. This is followed by an extensive set of validations tests for the model developed using both against experimental campaigns and higher-fidelity summations in Section 3.4. Finally in the last section, a brief review of the A-weighting noise metric that is used throughout this work is provided.

3.2 Fundamentals of Sound and Governing Acoustics Equation

Prior to discussing the governing acoustics equation that serves as the foundation for the methodologies presented in subsequent sub-sections, it is important to recognize a few important characteristics that will be beneficial to the reader later down in this chapter. Sound energy is transmitted in a fluid, in this case area, as a wave. Secondly, sound takes a finite about of time to travel from the source to the observer, implying that for moving sources such as aircraft, the located at time t where the sound was created is not the same location where the source would be when it reaches the observer. To correct predict the sound at an observe, one compute the acoustic pressure computed in the retarded time-frame, where retarded time corresponds to the sound emitted at an earlier time $\tau = t - \frac{R}{c_0}$ at a distance S away from an observer. Third, sound energy can also change due to atmospheric attenuation. Forth, variations in source speed can result in changes in wave

frequency. This is known as the Doppler effect. It is important that all of these effects are accounted for when formulating mathematical expressions for predicting the acoustic power spectral density at the observer at a given time.

Excluding the motor, the primary sources of noise from electric aircraft arise from the rotors. The rotating blade produce harmonic noise, broadband noise and unsteady-force noise. Harmonic noise, otherwise referred to as rotational noise occurs at integer multiples of the blade passing frequency and consists of thickness noise that arises from the displacement of the air by the volume of a passing blade element and loading noise due to a combination of lift and drag components on the rotating blade. Broadband noise arises from turbulent flow impinging on the rotating blades and blade self-generated turbulence interacting with the blade trailing edge. Lastly, unsteady-force noise is produced by blade vortex interaction and blade wake interaction meaning that it can be time-dependent in the rotating-blade frame of reference, for example, when rotors blades pass through the wake emanating from another blade.

3.2.1 Governing Acoustics Equation

The mathematical expression of the various sources of noise presented in subsequent sections all start with the governing equation by Ffowcs-Williams and Hawking [52] for the noise radiated from a body in an arbitrary motion

$$\begin{aligned} 4\pi c_0^2 \rho'(x, t) = & -\frac{\partial}{\partial x_i} \iint \left[\frac{P_{2j} n_j}{\Re [1 - M_{\Re i}]} \right]_\tau dS(\eta) \\ & + \frac{\partial}{\partial t} \iint \left[\frac{\rho_0 v_n}{\Re [1 - M_{\Re}]} \right]_\tau dS(\eta) \\ & + \frac{\partial^2}{\partial x_i \partial x_j} \iiint \left[\frac{T_{ij}}{\Re [1 - M_{\Re i}]} \right]_\tau dV(\eta) \end{aligned} \quad (3.1)$$

It is convenient to consider the blade as the moving body so that the reference frame is rotating with the blade. The term on the left-hand side of the equation represents the acoustic pressure where $p = \rho c_0$ while the three terms on the right-hand side, correspond to the thickness (monopole), loading (dipole) and unsteady random noise terms respectively. Examining this equation a little closer, we can see that the first term is simply a time derivative of the summation of thickness

source terms while the second is a spatial derivative of the summation of force source terms [53].

As previously stated, there are two main approaches to solving for the acoustic pressure in Equation 3.1 radiated from a source: the Time-domain approach and frequency-domain approach. Time-domain methods solve the governing equation directly in terms of the space-time variables resulting in predictions of the form $p(t)$. Frequency-domain methods on the other hand eliminate time from the wave equation by means of Fourier transformation but have been known to suffer from loss of information as a result of the oversimplification of the blade geometry [54]. This loss however is not as significant in the lower harmonic of interest near the BPF, as pointed out by Hubbard [55]. Despite suffering from lower accuracy, they are typically a few orders of magnitude less computationally expensive than time domain methods. For these results, a frequency-domain approach was deemed satisfactory and preferred for out applications.

3.3 Frequency Domain Acoustic Formulation

In this section, we cover the formulations used to predict the individual constituents of the overall sound spectrum generated from a rotor blade. Harmonic noise is discussed first, followed by broadband noise. The acoustic prediction of the aircraft is confined to rotating blades and excludes fluctuating loads on wings and noise generated in the quasi-steady wake. This suggest that unsteady random noise is omitted from subsequent formulations.

3.3.1 Harmonic Noise: Thickness and Loading Noise

In this work, Hanson's formation [56] of harmonic propeller noise in the frequency domain was implemented. Extending from early work by [57–62], this approach encompasses the effects of airfoil thickness, non-axial propeller inflow and blade sweep. To garner appreciation for the method used in this work, we start the derivation from a slightly modified version of the governing equation describing the generation of sound in the presence of sound boundaries in Equation 3.1 by Goldstein [63].

$$\begin{aligned}\rho'(x, t) = & -\frac{1}{c_0^2} \int_{-T}^T \int_{S(\tau)} \rho_0 V_n \frac{\partial G}{\partial \tau} dS(y) d\tau \\ & -\frac{1}{c_0^2} \int_{-T}^T \int_{S(\tau)} f_i \frac{\partial G}{\partial y_i} dS(y) d\tau \\ & +\frac{1}{c_0^2} \int_{-T}^T \int_{\nu(\tau)} T_{ij} \frac{\partial^2 G}{\partial y_i \partial y_j} dy d\tau\end{aligned}\quad (3.2)$$

where, V_n is the normal surface velocity while f_i represents the i^{th} component of the force per unit area exerted by the fluid on the boundary. T_{ij} is Lighthill's stress tensor which is used to describe quadrupole sources. This term however is not considered in this work and therefore will be ignored from henceforth. The integrals over the source time, τ are over the range $\pm T$ large enough to include all source times of interest. To solve this expression, we will utilize a collection of mathematical operations and approximations, the first of them being the free space form of Green's function which is essentially an integral kernel used to solve ODE's and PDE's. This function is given below as

$$G = \frac{\delta(t - \tau - R/c_0)}{4\pi R}, \quad (3.3)$$

where $R = |x - y|$, and x and y are the observer and source locations measures from a reference point fixed in the fluid.

We now examine the motion of the propeller blade in forward flight. Adopting the approach outlined in [62], we can replace the Cartesian coordinates for a single blade segment with the locally orthogonal helicoidal coordinates $\gamma_i = (\gamma_0, \zeta_0, r_0)$ depicted in Figure [Figure \[ref\]](#) and defined below:

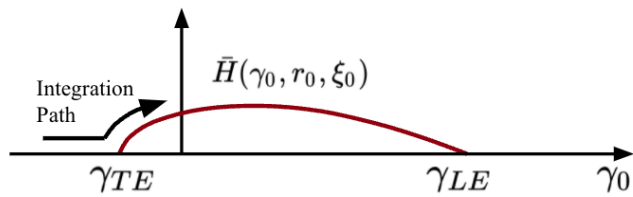
$$y_1 = \frac{\Omega r_0 \xi_0}{U} - \frac{V \gamma_0}{U} \quad (3.4a)$$

$$y_2 = r_0 \cos \left(\frac{V \xi_0}{r_0 U} + \frac{\Omega \gamma_0}{U} \right) \quad (3.4b)$$

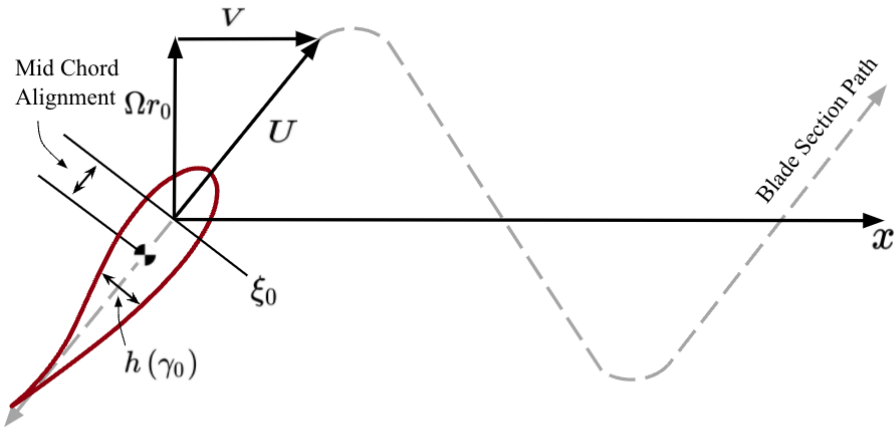
$$y_3 = -r_0 \sin \left(\frac{V \xi_0}{r_0 U} + \frac{\Omega \gamma_0}{U} \right) \quad (3.4c)$$

where

$$U = \sqrt{V^2 + (\Omega R)} \quad (3.5)$$



(a) Text.



(b) Text.

Figure 3.1: TEXT.

The first term on the right hand side of Equation 3.4c captures the distance the blade, travelling at a particular speed, U given in Equation 3.5 has gone in time t while the second term captures the angular offset of the blade from $t = 0$. Using this coordinate system, the observer at a distance R

from the source can not be expressed as

$$R = \sqrt{\left(x - \frac{\Omega r_0 \xi_0}{U} + \frac{V \gamma_0}{U}\right)^2 + y^2 - 2y r_0 \cos\left(\frac{V \xi_0}{r_0 U} + \frac{\Omega \gamma_0}{U}\right) + \dots} \\ \dots + z^2 + 2z r_0 \cos\left(\frac{V \xi_0}{r_0 U} + \frac{\Omega \gamma_0}{U}\right) + r_0^2 \quad (3.6)$$

With the thin airfoil approximation to permit solving the surface boundary conditions on the mean camber line surface rather than the upper and lower surfaces of the blade. For the surface sources, the surface area element dS can be re-expressed as a function of the differential span of the blade element, r and the differential element of the mean camber line surface, γ as follows:

$$dS = dr d\gamma \quad (3.7)$$

to give:

$$p(x, t) = - \int_{-\infty}^{\infty} \int_0^r \int_{-\infty}^{\infty} \left(\rho_0 V_n \frac{\partial G}{\partial \tau} + f_i \frac{\partial G}{\partial \gamma_i} \right) d\gamma_0 dr_0 d\tau \quad (3.8)$$

The second significant mathematical operation is the expression of surface sources as volume sources. First, the monopole source is given as :

$$V_n = U \int (\gamma_0, r_0) \quad (3.9a)$$

$$V_n = U J \bar{H}' (\gamma_0, r_0, \xi_0) d\xi_0 \quad (3.9b)$$

Secondly, the dipole source f_i at τ_0 can be written as

$$f_i (\gamma_0, r_0) = \int F_i (\gamma_0, r_0, \xi_0) d\xi_0 \quad (3.10a)$$

$$F_i (\gamma_0, r_0, \xi_0) = f_i (\gamma_0, r_0) \delta (\xi_0) \quad (3.10b)$$

Again the action at the mean surface is expressed by:

$$\bar{H}(\gamma_0, r_0, \xi_0) = h(\gamma_0, r_0) \delta(\xi_0) \quad (3.11)$$

The acoustic pressure given by the volume-time integral is now

$$p = \iiint \left[-\rho_0 U \bar{H}'(\gamma_0 + U\tau, r_0, \xi_0) \frac{\partial G}{\partial \tau} - F_i(\gamma_0 + U\tau, r_0, \xi_0) \frac{\partial G}{\partial \gamma_i} \right] d\xi_0 d\gamma_0 dr_0 d\tau \quad (3.12)$$

The third significant mathematical operation is the representation of the integrand on the right hand side as one function, $g(\gamma_0, r_0, \xi_0)$, where

$$g(\gamma_0, r_0, \xi_0) = \rho_0 U^2 \bar{H}''(\gamma_0, r_0, \xi_0) + \frac{\partial}{\partial \gamma_i} F_i(\gamma_0, r_0, \xi_0) \quad (3.13)$$

We can now rewrite the Equation 3.12as

$$p(x, t) = \iiint \int g(\gamma_0 + U\tau, r_0, \xi_0) \frac{\delta(t - \tau - R/c_0)}{4\pi R} d\xi_0 d\gamma_0 dr_0 d\tau \quad (3.14)$$

In this equation above, the τ integration may be performed first because the spatial integration limits no longer depend on τ (i.e. no $\frac{\partial}{\partial \tau}$), yielding

$$p(x, t) = \iiint \frac{I}{4\pi R} g\left(\gamma_0 + Ut - \frac{UR}{c_0}, r_0, \xi_0\right) d\xi_0 d\gamma_0 dr_0 \quad (3.15)$$

Finally, to determine far field noise, we first perform a binomial expansion of Equation 3.6 for radiation points near the origin (blade sections) to the field point r, θ . Retaining terms to first order in $\gamma_0/r, \zeta_0/r$ and r_0/r yields

$$R \rightarrow r - \frac{\Omega r_0}{U} \xi_0 \cos \theta + \frac{V}{U} \gamma_0 \cos \theta - r_0 \sin \theta \cos \left(\frac{V \xi_0}{U r_0} + \frac{\Omega \gamma_0}{U} \right) \quad (3.16)$$

Using a Fourier transformation pair to describe oscillatory nature of the source:

$$\psi\left(\frac{\omega}{U}, r_0, \xi_0\right) = \int_{-\infty}^{\infty} g(\gamma_0, r_0, \xi_0) \exp\left[i \frac{\omega}{U} \gamma_0\right] d\gamma_0 \quad (3.17)$$

where

$$g(\gamma_0, r_0, \xi_0) = \frac{1}{2\pi U} \int_{-\infty}^{\infty} \psi\left(\frac{\omega}{U}, r_0, \xi_0\right) \exp\left[-i\frac{\omega}{U}\gamma_0\right] d\omega \quad (3.18)$$

Substitution 3.18 into 3.15 yields

$$p(x, t) = \frac{1}{8\pi^2 r} \iiint \frac{1}{U} \int \psi\left(\frac{\omega}{U}, r_0, \xi_0\right) \times \exp\left[-i\frac{\omega}{U}\left(\gamma_0 + Ut - \frac{UR}{c_0}\right)\right] d\omega d\xi_0 d\gamma_0 dr_0 \quad (3.19)$$

Recognizing that this is in the form of a Fourier integral shown below

$$p(x, t) = \int P(x, \omega) e^{-i\omega t} d\omega \quad (3.20)$$

, we can apply a Fourier transform on the acoustic pressure to obtain the pressure as a function of frequency

$$P(x, \omega) = \frac{I}{8\pi^2 r} \iiint \frac{1}{U} \psi\left(\frac{\omega}{U}, r_0, \xi_0\right) \times \exp\left[-i\frac{\omega}{U}\left(\gamma_0 - \frac{UR}{c_0}\right)\right] d\xi_0 d\gamma_0 dr_0 \quad (3.21)$$

Note here that for the amplitude factor $\frac{1}{R}$, we simply use $R \rightarrow r$. Substituting Equation 3.16 into Equation 3.21 yields

$$P(x, \omega) = \frac{\exp\left[i\frac{\omega r_0}{c_0}\right]}{4\pi r} \iint \psi\left(\frac{\omega}{U}, r_0, \xi_0\right) \times \exp\left[-i\frac{\omega}{c_0} \frac{\Omega r_0}{U} \xi_0 \cos \theta\right] I d\xi_0 dr_0, \quad (3.22)$$

where

$$I = \frac{1}{I - M_x \cos \theta} \sum_{n=-\infty}^{\infty} J_n\left(\frac{\omega r_0}{c_0} \sin \theta\right) \times \exp\left[in\left(\frac{V\xi_0}{Ur_0} - \frac{\pi}{2}\right)\right] \delta\left(\omega - \frac{n\Omega}{I - M_x \cos \theta}\right) \quad (3.23)$$

from which it follows that the noise at radiation angle B is periodic at the Doppler frequency $(\Omega/\pi)/(l - M_x \cos \theta)$. If we write the discrete spectrum as the sum of the harmonics

$$P(x, \omega) = \sum_{n=-\infty}^{\infty} P_n(x) \delta \left(\omega - \frac{n\Omega}{1 - M_x \cos \theta} \right) \quad (3.24)$$

where P_n is the n th complex Fourier coefficient of the acoustic pressure, then

$$\begin{aligned} P_n(x) = & \frac{\exp \left[in \left(\frac{\Omega_D r}{c_0} - \frac{\pi}{2} \right) \right]}{4\pi r (I - M_x \cos \theta)} \int_0^\infty J_n \left(\frac{n\Omega_D r_0}{c_0} \sin \theta \right) \times \int_{-\infty}^\infty \psi \left(\frac{n\Omega_D}{U}, \xi_0, r_0 \right) \dots \\ & \times \exp \left[-i \frac{n}{U} \left(\frac{\Omega \Omega_D r_0}{c_0} \cos \theta - \frac{V}{r_0} \right) \xi_0 \right] d\xi_0 dr_0 \end{aligned} \quad (3.25)$$

where $\Omega_D = \Omega / (1 - M_x \cos \theta)$.

This is the general far-field result for any helically convected source as given by g in Equation 3.13 and its transform in Equation 3.17. For B blades, the m^{th} harmonic of blade passing frequency is found by setting $n = mB$ and multiplying by B . Waveforms can be computed from the Fourier series. Using the a definition of coordinate systems in Figure 3.2 below, θ and ϕ denote radiation angles of an arbitrary propeller in a freestream at an angle of attack, α relative to the observer. These two angles are defined in Equation 3.26 along with other geometrical expressions required to fully interpret the diagram.

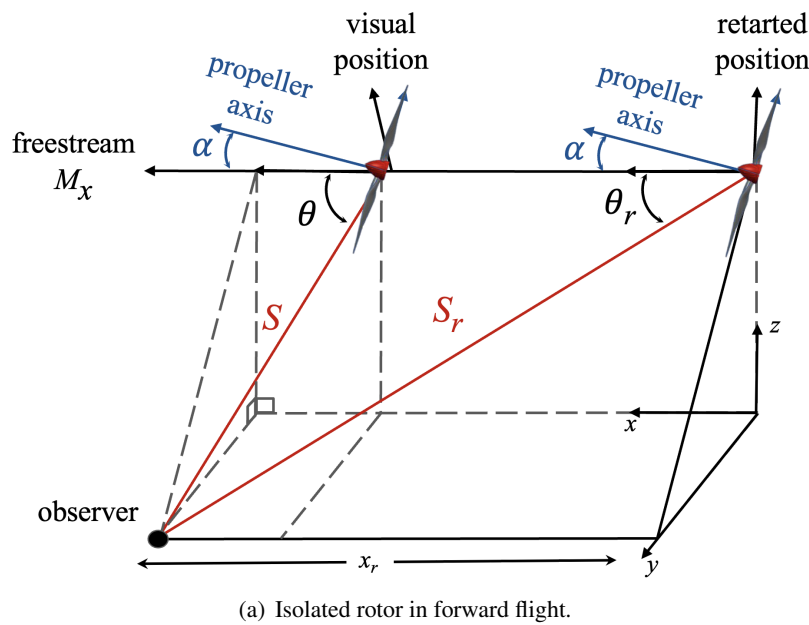
$$\text{where } \theta = \cos^{-1} \left(\frac{x}{S} \right) \quad , \quad \phi = \tan^{-1} \left(\frac{z}{y} \right) \quad , \quad S = \sqrt{x^2 + y^2 + z^2} \quad , \quad Y = \sqrt{y^2 + z^2} \quad (3.26)$$

Applying the required transformation from the visual frame to the retarded frame using Equations 3.27a and 3.27b result in the corrected distance and radiation angles from the point of emission.

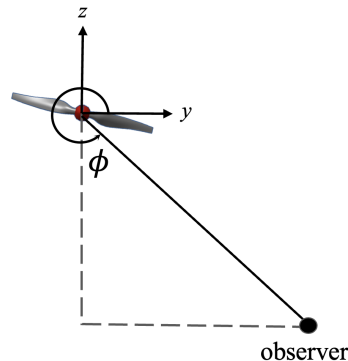
$$\theta_r = \cos^{-1} \left(\cos(\theta) \sqrt{1 - M_x^2 \sin^2 \theta} + M_x \sin^2 \theta \right) \quad (3.27a)$$

$$S_r = \frac{Y}{\sin \theta_r} \quad (3.27b)$$

Finally, modification of the propeller from the inertial frame to the body-fixed frame oriented α



(a) Isolated rotor in forward flight.



(b) Azimuth radiation angle.

Figure 3.2: Sound emission reference frames.

relative to the freestream as shown in Figure 3.2 yields the following:

$$\cos \theta'_r = \cos \theta_r \cos \alpha + \sin \theta_r \sin \phi \sin \alpha \quad (3.28a)$$

$$\cos \phi' = \frac{\sin \theta_r}{\sin \theta'_r} \cos \phi \quad (3.28b)$$

With these definitions, the thickness and loading noise components of the root mean squared pressure of the n^{th} rotor is be expressed as:

$$P_{Tm_n} = \frac{-\rho a^2 B \sin \theta_r \exp [imB (\frac{\Omega S_r}{a} + (\phi' - \frac{\pi}{2}))]}{4\sqrt{2}\pi(Y/D) (1 - M_x \cos \theta_r)} \dots \int_{hub}^{tip} M_s^2(h/b) \exp(i\phi_s) J_{mB} k_x^2 \Psi_V dr \quad (3.29)$$

$$P_{Lm_n} = \frac{imB M_t \sin \theta_r \exp [imB (\frac{\Omega S_r}{a} + (\phi' - \frac{\pi}{2}))]}{2\sqrt{2}\pi Y r_t (1 - M_x \cos \theta_r)} \dots \int_{hub}^{tip} \left[\frac{\cos \theta'_r}{1 - M_x \cos \theta_r} \frac{dT}{dr} - \frac{1}{r^2 M_t r_t} \frac{dQ}{dr} \right] \exp(i\phi_s) J_{mB} \Psi_L dr \quad (3.30)$$

where

$$J_{mB} = J_{mB} \left(\frac{mBrM_t \sin \theta'_r}{1 - M_x \cos \theta_r} \right) \quad (3.31)$$

k_x , the ratio of the blade passing frequency to the speed of the aircraft or wave number for short is given as:

$$k_x = \frac{2mBbM_t}{M_s (1 - M_x \cos \theta_r)} \quad (3.32)$$

and ϕ_s is the phase lag due to the sweep of the rotor defined below:

$$\phi_s = \frac{2mBM_t}{M_s (1 - M_x \cos \theta_r)} \frac{MCA}{D} \quad (3.33)$$

Given below in Equation 3.34, Ψ_V is the source term that approximates the chordwise thickness as

a parabolic distribution with maximum thickness at unity while Ψ_L in Equation 3.35 represents a uniform lift distribution.

$$\Psi_V(k_x) = \begin{cases} 2/3 & \text{if } k_x = 0 \\ \frac{8}{k_x^2} \left[\frac{2}{k_x} \sin\left(\frac{k_x}{2}\right) - \cos\left(\frac{k_x}{2}\right) \right] & \text{if } k_x \neq 0 \end{cases} \quad (3.34)$$

$$\Psi_L(k_x) = \begin{cases} 1 & \text{if } k_x = 0 \\ \frac{2}{k_x} \sin\left(\frac{k_x}{2}\right) & \text{if } k_x \neq 0 \end{cases} \quad (3.35)$$

Finally, the total unweighted harmonic sound pressure level from a single rotor is determined through decibel arithmetic of the thickness and loading terms as follows:

$$SPL_{har_m_n} = 20 \log \left(\frac{P_{Tm_n} + P_{Lm_n}}{P_0} \right). \quad (3.36)$$

3.3.2 Broadband Noise: Trailing-Edge Noise

The term broadband noise is in fact used to collectively refer of noise generating phenomena, including Blade-Wake Interaction (BWI) noise due to a rotor blade's interaction with the turbulent wakes emanating from preceding blades, blade vortex interaction (BVI) noise produced by the rotor blade's interaction with the strong tip vortex and self-noise generated as a result of the development and shedding of turbulence within the rotor blades' boundary layers [64]. Self-noise itself too is a combination of noise-generation mechanisms that include the following: 1) trailing edge noise is caused by the scattering of the turbulence pressure field on both the upper and lower surfaces of the rotor blade; 2) laminar boundary layer - vortex shedding (LBL-VS) noise generated at conditions conducive to laminar boundary layer flow on the surfaces of the blade; 3) blunt trailing edge (BTE) noise is due to vortex shedding from a less-than-sharp trailing edge and ; 4) tip noise due to the finite nature of the lifting surface resulting in the formation and shedding of a tip. Figure ?? highlights some of these major contributors to overall broadband noise for a BO-105 model rotors. The rotor in this experimental set-up was approximately 4 meters in diameter and operated around a tip Mach number of 0.6. These details are significant because although it was a scaled model of a helicopter blade, it is equivalent in size and operating tip Mach range of most eVTOL lift-rotor blades. This

allows us to make some preliminary hypotheses on EVTOL aircraft noise.

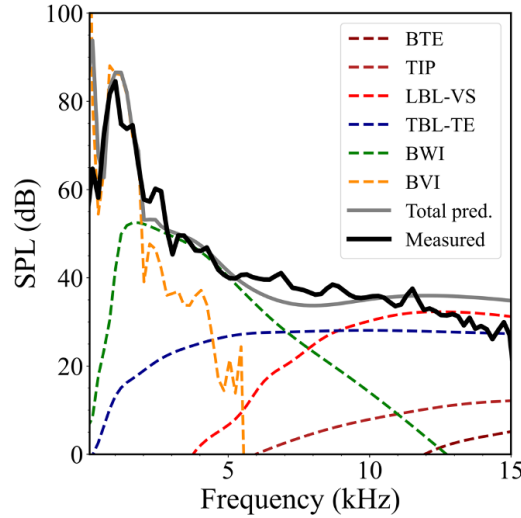


Figure 3.3: TEXT [3] .

Thus far, only the trailing-edge noise component of broadband noise has been implemented and validated; formulations for the remaining components are still under development. An under-prediction in total aircraft noise is there expected, particularly in the vertical transition and descent flight stages of flight where BWI and BVI dominate. In these maneuvers, the wakes from the preceding rotors impinge on encroaching blade generating large amounts of acoustic energy. The acoustic power spectral density of this source is determined the model proposed by Amiet [65] and follows the methodology outlined in [66]. The process begins with the discretized loads and local flow incidence angles of all sections of the rotating blades obtained from BEVF routine described in Chapter 2. A viscous panel method code is then used to compute the boundary layer properties. This evaluation of the surface pressure distribution and the magnitude of the displacement and momentum thicknesses at the trailing edge using a combination of potential theory and laminar and turbulent boundary layer models from Thwaites [45] and Head [46] respectively is a departure from the empirical models proposed by Brooks, Pope and Marcolini [67] whose model assume symmetric airfoil sections and utilize empirical estimations for boundary layer properties. The computed variables along the surface are rotor blades are then used in Lee's wall pressure spectrum model. A more detailed methodology is now presented below. We start the mathematical formation

by examining a section of the blade shown in Figure 3.4. The local coordinate system located at the midspan of each blade segment is shown in the figure, with both the x and y axes lying on the rotor disk plane if the blade segment is not pitched with respect to the rotor disk. Additionally, the blade pitch angle, α_p , is the angle between the rotor plane and the local blade chord.

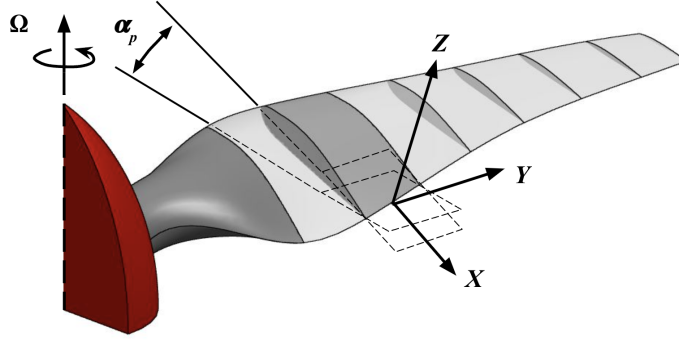


Figure 3.4: Local blade section coordinate system.

Starting with Amiet's model for power spectral density at an observer location with respect to the upper and lower surfaces of the airfoil can be written as:

$$S_{pp(U/L)} = \left(\frac{\omega}{a}\right)^2 c^2 dr \left(\frac{1}{32\pi^2}\right) \frac{N_B}{2\pi} \int_0^{2\pi} D_\phi |L|^2 l_r \Phi_{pp} d\phi \quad (3.37)$$

where U and L represent the upper and lower surfaces of an airfoil, respectively and

$$\epsilon^2 = X^2 + \beta^2 (Y^2 + Z^2) \quad (3.38a)$$

$$\beta^2 = 1 - M^2 \quad (3.38b)$$

$$\frac{\omega_d}{\omega} = \frac{1}{1 + M_r \left(\frac{X}{R_s}\right)} \quad (3.38c)$$

$$M_r = \frac{\Omega r}{a}. \quad (3.38d)$$

D is the spectrum directivity as defined in the appendix of [66], ϵ is the doppler shifted frequency and c is the chord length of the blade section. This paper also provides a comprehensive review of the coordination transformation from the observer to the blade section surface, including any out of plane flapping motion of the blade thus the authors refer the reader to this reference. Schlinker and

Amiet's model [3] for the loading term, L is used in the above formulation. It is given as follows:

$$|L| = \frac{1}{\Lambda} \left| e^{i2\Lambda} \left[1 - (1+i)E^* \left(2(\bar{K} + \bar{\mu}M + \bar{\gamma}) \right) + e^{-i2\Lambda} \sqrt{\frac{K + \mu M + \gamma}{\mu x \epsilon + \gamma}} (1+i) + \dots E^* \left(2 \left(\frac{\bar{\mu}x}{\epsilon} + \bar{\gamma} \right) \right) \right] \right| \quad (3.39)$$

where

$$\Lambda = \bar{k}_x - \frac{\bar{\mu}x}{\epsilon} + \bar{\mu}M \quad (3.40a)$$

$$K = \frac{\omega_d}{U_c} \quad (3.40b)$$

$$\mu = \frac{\omega_d M}{U \beta^2} \quad (3.40c)$$

$$\gamma^2 = \left(\frac{\mu}{\epsilon} \right)^2 (x^2 + \beta^2 z^2). \quad (3.40d)$$

Here, k_x is the chordwise wave number denoted by ω/U and $mu = Mk_x/beta^2$ and E^* represents the complex conjugate of a Fresnel integral defined by

$$E(x) \equiv \frac{1}{\sqrt{2\pi}} \int_0^x e^{it} \frac{dt}{\sqrt{t}}. \quad (3.41)$$

The bar over the variables indicated normalization by the semichord of the blade section. Lastly, the wall pressure proposed by Lee [68] is used. This model uses a wall-pressure spectrum model that capable of handling zero pressure gradient flows and non-symmetric and high-loading airfoil flows and has as been shown by the author to produce results closer to benchmark experimental tests than other wall-pressure models in [69–72]. is given by

$$\frac{\Phi_{pp}(\omega)U_e}{\tau_w^2 \delta^*} = \frac{\max(a, (0.25\beta_c - 0.52)a) \left(\frac{\omega \delta^*}{U_e} \right)^2}{\left[4.76 \left(\frac{\omega \delta^*}{U_e} \right)^{0.75} + d^* \right]^e + (8.8R_T^{-0.57}) \left(\frac{\omega \delta^*}{U_e} \right)} \quad (3.42)$$

Table 3.1 below documents the parameters used within the Equation 3.42.

Table 3.1: Parameters for wall pressure spectrum model.

Parameter	Value
β_c	$(\Theta/\tau_w) dp/dx $
a	$2.28\Delta^2 (6.13\Delta^{-0.75} + d)^e [4.2(\Pi/\Delta) + 1]$
Δ	δ/δ^*
Π	$0.8 (\beta_c + 0.5)^{3/4}$
e	$3.7 + 1.5\beta_c$
d	$4.76(1.4/\Delta)^{0.75}[0.375e - 1]$
R_T	$(\delta/U_e) (v/u_\tau^2)$
h^*	$\min(3, (0.139 + 3.1043\beta_c)) + 7$
d^*	if $(\beta_c < 0.5)$, = $\max(1.0, 1.5d)$, otherwise = d

Finally, the far-field SPL for one side of the i^{th} section on the n th rotor blade is calculated from the acoustic power spectral density S_{pp} as

$$\text{SPL}_{\text{bb}_i(U,L)} = 10 \log_{10} \left(\frac{2\pi S_{pp}(U,L)}{P_0^2} \right). \quad (3.43)$$

The rotor's total SPL can now be computed through decibel arithmetic

$$\text{SPL}_{\text{bb}_n} = 10 \log_{10} \sum_{i=1}^{n_S} \left(10^{0.1 \text{SPL}_{\text{bb}_i,U}} + 10^{0.1 \text{SPL}_{\text{bb}_i,L}} \right) \quad (3.44)$$

where n_S is the total number of sections. Likewise, the total SPL of a vehicle with multiple rotors is given in Equation 3.45 below:

$$\text{SPL}_{\text{bb}_{\text{tot}}} = 10 \log_{10} \sum_{j=1}^n \left(10^{0.1 \text{SPL}_{\text{bb},j}} \right). \quad (3.45)$$

3.3.3 Total Vehicle Noise

The final step of the noise prediction methodology is the summation of the harmonic and broad-band component for each source (rotor) on the aircraft is accomplished through decibel arithmetic. The general two step formula can be applied to sum any number of sources:

$$\left(\frac{p}{p_{ref}}\right)_i^2 = 10^{SPL_i/10} \quad (3.46a)$$

$$SPL = 10 \log_{10} \left[\sum_{i=1}^n \left(\frac{p}{p_{ref}} \right)_i^2 \right] \quad (3.46b)$$

3.4 Computational Model Validation

3.4.1 Harmonic Noise

The propeller harmonic noise is validated against experimental data obtained from Weir [4]. This experimental test campaign was geared towards evaluating the performance of NASA Aircraft Noise Prediction Program (ANOPP) Propeller Analysis System (PAS) tool and examined propeller noise for a Piper Lance aircraft for comparison with FAA wind tunnel and flyover data. The comparisons presented in this paper are a subsect of the results reported in the reference. The tests conducted on a single 2-bladed, 2.03-meter diameter Hartzell F8475 D-4 propeller which has a rounded-tip and Clark-Y airfoil sections are selected for validation here. The in-flow microphones were placed at 60° and 90° from the propeller axis at a nominal distance of 4 meters. Additional information on the environmental and operating conditions can be found in the reference. Figure 3.5 documents the three cases at power coefficients of 0.027, 0.047 and 0.042. The right column of plots corresponds to the SPLs of the first 18 harmonics at the microphone positioned at 60° from the propeller axis while the left column corresponds to the microphone positioned at 90° . With the exception of the in-plane case at $C_P = 0.042$, reasonably good agreement of the medium-fidelity model implemented in SUAVE to PAS and the experimental data reported in the literature is achieved.

The second validation study of harmonic noise was on the directivity of first two harmonics of around the propeller. Static-rotor tests by Hubbard [73] were used to benchmark the performance of the implemented computational routine. In this experiment, the helical tip Mach number was 0.62 with microphone placed at 30 feet from the propeller hub. Additionally, the geometry of the

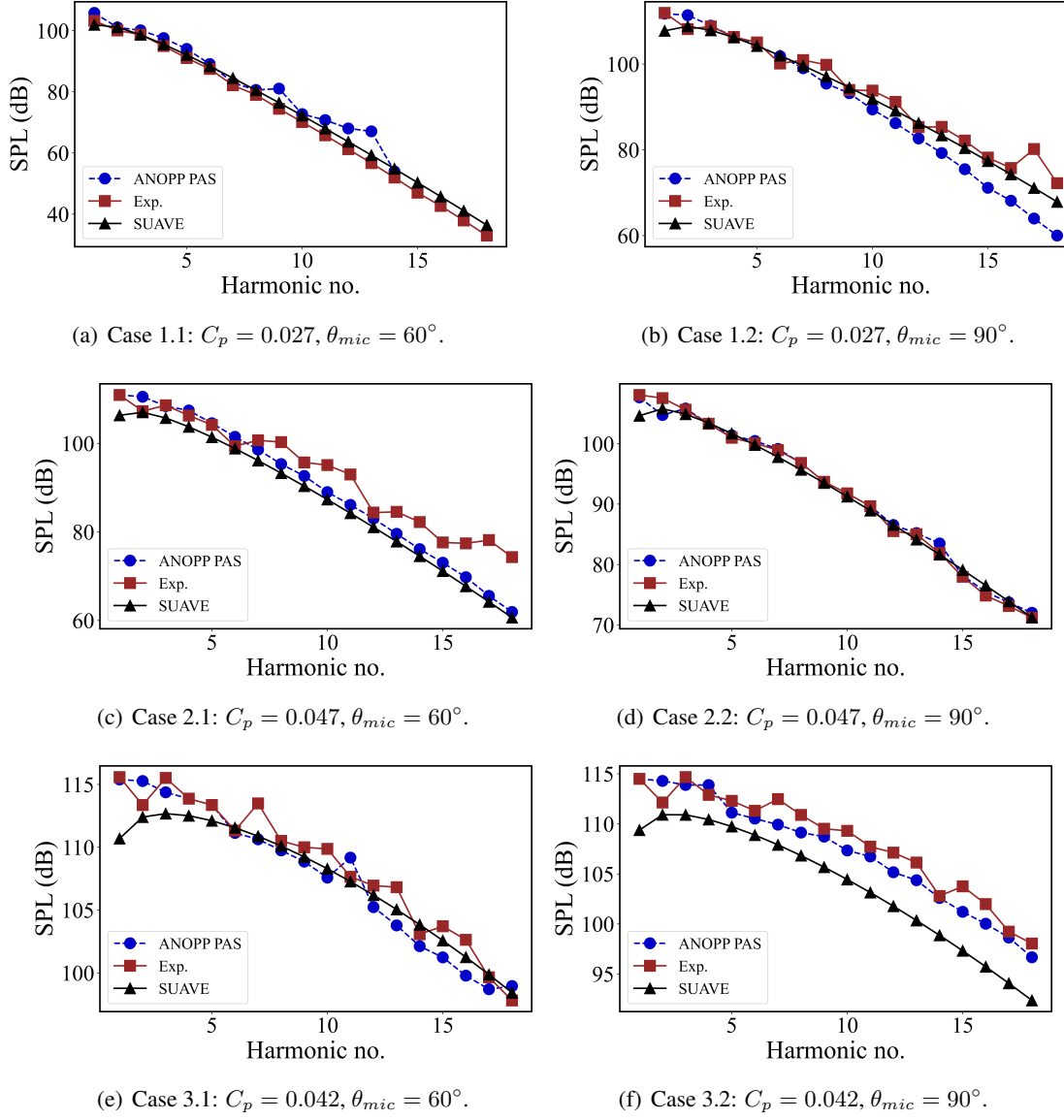


Figure 3.5: Comparison of SUAVE prediction with PAS and data for windtunnel test cases [4].

propeller blades and other test conditions can be found in the reference. The polar plots in Figure 3.6 show that the performance of this semi-empirical prediction routine start to break down as the observer moves away from the plane the rotor or conversely approaching the propeller axis. This is expected given the mathematical formations for the thickness and loading noise which, with simplifications, can be reduced to show that the strongest signatures are around at 25° and 60°

respectively. Nevertheless, the results for over 77% of the sound directivity were within reasonable bounds and was this deemed satisfactory for the purposes of this study.

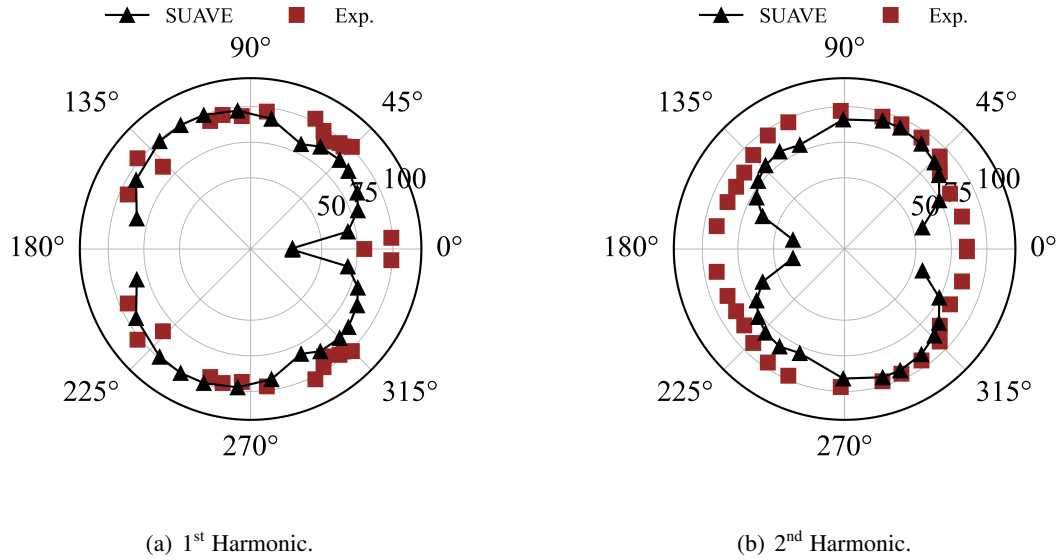


Figure 3.6: Tonal noise directivity validation study.

3.4.2 Broadband Noise

The experimental campaign to identify characters of the power spectral density of small unmanned aircraft systems by Zawodny et al. [74] is used to assess the accuracy of the implemented noise model. These tests were conducted on an APC 11x4.7 SF rotor blade and DJI 9443 rotor blade at Structural Acoustics Loads and Transmission Anechoic chamber facility at NASA Langley Research center. Isolated broadband noise measurements of the APC blade are discussed here for validation. In contrast to the validation study of the harmonic noise model, that of broadband proved moderately successful. Individuals who were directly responsible for data collection at the SALT facility indicated that the isolated broadband noise could potential have captured tonal behavior from the interference of the rotor wake causing sound energy radiation off the testing rig and mounting rod. This would explain why poor performance is seen near the blade passing frequency of the test conditions despite good agreement in the mid to high regions of the spectrum.

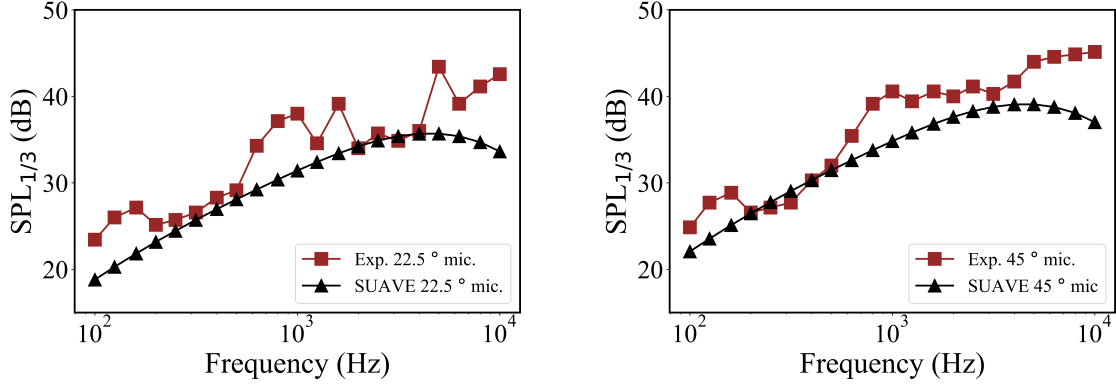


Figure 3.7: Trailing-edge broadband noise validation study.

3.4.3 Total Isolated Rotor Noise

In Figure 3.8, we compare the full $\frac{1}{3}$ octave band spectrum of the the APC rotor used [74] to experimental data. Measurements were taken at a distance of 1.905 and angle of 45° from the propeller plane. Additional information about experimental setup for these static tests can be found in [74]. Through the computational model over-predicts broadband noise near the blade passing frequency, we observe that together with the harmonic noise components that dominate in this range, the overall noise spectrum falls within reasonable bounds of the experimental data. Future work will however seek to improve these medium-fidelity methods for prediction power spectrum densities.

3.4.4 Comparison of Noise Prediction Approach: Time-Domain vs. Frequency Domain

To gain a full appreciation of the decision to opt for a frequency-domain approach over a time-domain approach, a comparison of prediction accuracy at the expense of computation time is given below. On the left, Figure 3.9(a) shows differences in the full acoustic spectrum of a DJI Phantom III Drone Rotor predicted using the BEVT discussed in Chapter 2 the an application of the newly

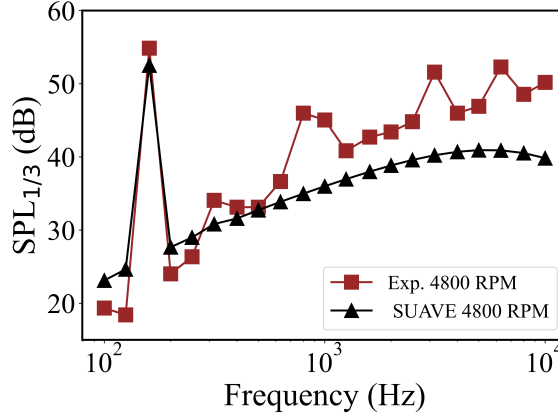
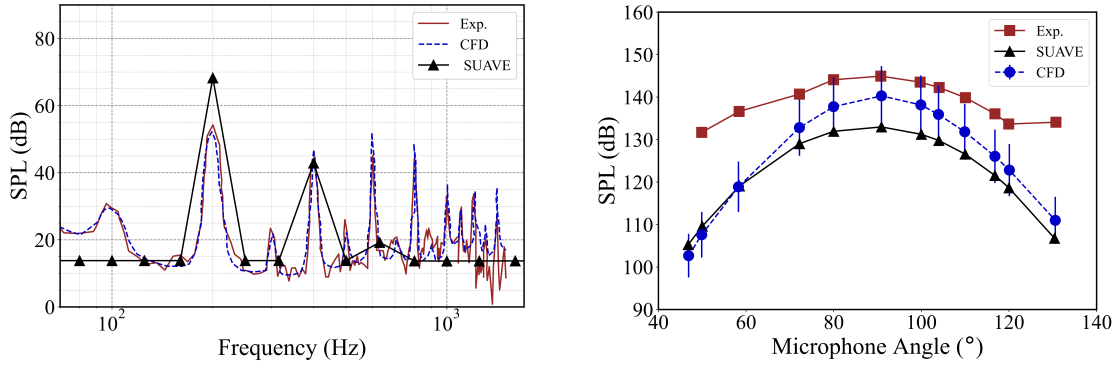


Figure 3.8: One-third octave band acoustic spectrum at RPM = 4800.

implemented method discussed above and high-fidelity simulations from [75] that coupled OpenFoam to Farassat's 1A formulation of the FWH equation developed by Brentner and Farassat [76]. In the figure, the former method is labeled "SUAVE" while the latter is labeled "CFD". The rotor is a 2-bladed rotor with a 0.24 m diameter, operating conditions at an RPM of 6000 RPM. Experimental measurements (shown as the red dashed line on the plot) were taken at $\theta_{mic} = -30.5$, at a distance of 1.51 meters away from the blade. From the figure, it can be gathered that the implemented model sufficiently captures lower harmonics but not quite the higher harmonics as shown by the rapid decay of tonal peaks. The general broadband shape is however captured reasonably well by the frequency-domain model. In terms of computation time however, more accurate high-fidelity results do come with a considerable penalty, for the DES with RANS turbulence model used in [75] took about 2250 CPU-Hours to solve a 78 million cell model. The simulation in SUAVE took only 3.83 seconds, underscoring its applicability for iterative design.

In the second image on the left, CFD simulations by Tan et al.[77] of an 8-blade, 0.622 m diameter SR2 propeller were compared to SUAVE. Again, this higher-fidelity method used a time-domain approach to determine the sound pressure level of the rotor. The advance ratio of the simulated rotor was 3.06 with a freestream Mach number of 0.6. In this study, noise measurements were taken around the propeller axis. The exact distances between the propeller and microphone array are provided in [78]. As shown in Figure 3.9(b), the medium-fidelity directivity predictions using SUAVE fell within 10 % of high-fidelity simulations. This is achieved considerable low computing

– the CFD-based method tool 560 CPU hours while the model in SUAVE took 6.22 seconds to compute all radiated sound pressure level values. Another very significant observation is that both methods lose predictive accuracy near the axis of the rotor blade (directly in front on being of the disc plane). Though surprising for the high-fidelity method, its behavior is expected from the implemented frequency-domain method as previously highlighted in Figures 3.6(a) and 3.6(b). This implies that for vehicles in hover, the total noise radiated directly beneath the aircraft will not be reflected in the amassed results.



(a) One-third octave band comparison of implemented frequency-domain modeling approach to CFD reference data against experimental data for DJI rotor.

(b) SPL directivity comparison of implemented frequency-domain modeling approach to CFD reference data against experimental data for APC rotor.

Figure 3.9: Noise computation modeling fidelity comparisons.

3.5 A-Weighting Noise Metric

Currently, there are numerous assessment methods to quantify aircraft noise and annoyance in communities around airports. A few noteworthy ones are weighted sound pressure level-based ratings, computed loudness and annoyance based ratings, noise level and event-based ratings and statistical centennial based rating. The rationale behind the development of several noise ratings stemmed from the purpose of using a different noise rating that adequately predicts human response to noise [79]. Different occasions led to a slightly different rating in each case. More [80] outlines some of their respective advantages and disadvantages. For the purposes of this study, the A-weighted Maximum Noise Level, SPL_{Amax} , measured in dBA is used. This is an instantaneous

peak noise level measured at an observer location during the time period in consideration.

The A-weighting scheme is based on equal loudness contours [81] at different pressure levels. A universally accepted for community noise, this scheme takes into consideration the fact that human ears have different responses at different frequencies. Given as a function of frequency, $A(f)$, this scheme is added to the raw sound pressure level. The exact function is provide in Equation 3.47 and illustrated in Figure 3.10. This expression was developed by first fitting the A-weighting standard to a continuous polynomial. It is then summed to the sound pressure level of the corresponding frequencies to produce a re-scaled noise spectrum. It can be seen from the figure that $A(f)$ is maximum near a frequency of approximately 2.5 kHz, indicating that the human ear is particularly sensitive to sounds at this frequency. To reduce subjective annoyance, the designer should strive to avoid sound frequencies near 3 kHz as much as possible.

$$R_A(f) = \frac{12194^2 f^4}{(f^2 + 20.6^2) \sqrt{(f^2 + 107.7^2)(f^2 + 737.9^2)} (f^2 + 12194^2)} \quad (3.47a)$$

$$A(f) = 20 \log_{10} (R_A(f)) - 20 \log_{10} (R_A(1000)) \quad (3.47b)$$

$$SPL(dBA) = SPL(dB) + A_f(f) \quad (3.47c)$$

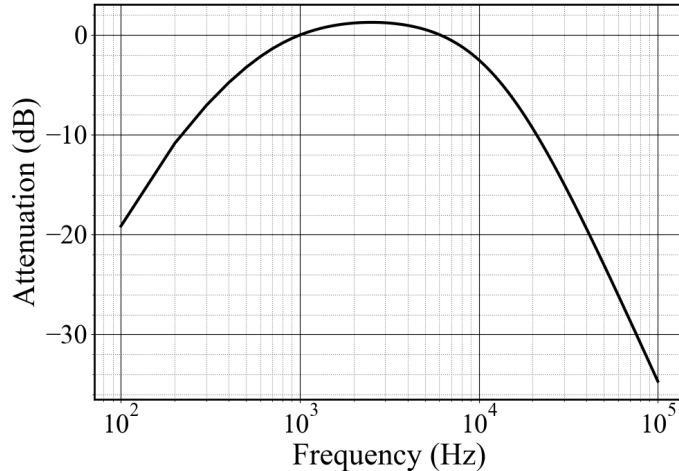


Figure 3.10: Text.

3.6 Chapter Summary

Chapter 4

Lithium-Ion Battery Modeling for Aerospace Applications

4.1 Introduction

Growing public concern over the extent over the impact of fossil fuel consumption on the natural environment has driven industries and stakeholders to seriously consider viable alternatives for powering land, air and maritime vehicles. Now that recent advances in clean technology have made renewable energy conversion as cheap, if not cheaper than nuclear and coal alternatives [82], a vision of a carbon-neutral future is becoming more apparent. In the automotive industry alone, there has already been significant progress with the likes of electric cars constituting 7.2 million of the total vehicles on the planet [83]. According to IEA this number is expected to rise to 150 million by the year 2030. By contrast, the adoption of clean technology in aerospace applications such as aerial cargo delivery passenger travel has proved to be somewhat are a challenge for a variety of reasons. These include the safely of operating at electrical loads characteristic of flight vehicles, system redundancy in the event of a power failure, the gross weight of the energy storage unit and auxiliary components, and last but not least public perception. Truly, realizing an emission-free future entails addressing all of these areas of concern. One step in this direction is the improvement of modeling fidelity adopted to design, assess and ultimately inform the certification of the devices

constituting these novel propulsion systems. In this chapter, we narrow our focus on the use of lithium-ion batteries as an alternative to aviation fuel as the source of energy for mid to short-range travel.

The development of high power and energy density batteries have provided the impetus to seriously consider the viability of battery-electric aircraft for RUAM. In a direct response the need to accurately assess the performance of these cells for ensuring safe operation and identifying potential points of failure in the flight operation has grown. The following sections of this chapter document the development of a semi-empirical model for predicting degradation in lithium-ion batteries and using it to assess the performance of an all-electric aircraft over its operational lifetime. This chapter is arranged in 5 main sections. A review of the general classification of batteries is provided in 4.2 followed by an in depth discussion on battery modeling in Section 4.3. The third sections provides an overview of electrification in the aerospace industry and provides the framework for the three-part model presented in Section 4.5. A thermal and capacity fade validation of this model is then provided in Section 4.6

4.2 Categorizing Lithium-ion Batteries

Reliability in performance coupled with high energy and power densities have led to rechargeable lithium-ion batteries being the preferred energy source for EVs [84, 85] over other battery technologies such as molten salts and lithium-air. Due to high demand, mostly driven by consumer electronics and the automotive industry, the low manufacturing cost has also made it easier to develop and test battery packs based on such technology. The primary components of this electrochemical cell are; (1) a cathode, (2) an anode, separated by (3) an electrolyte that is connected to (4) current collectors as shown in Figure 4.1(b). The electrolyte itself is a liquid organic solvent containing free lithium ions and other compounds for fire retardation and decelerating the formation of unwanted by-product formation retardation other fire retardant components. When a charged cell is connected to an external circuit and experiences a potential difference, the flow of electrons from the cathode to anode occurring outside of the cell across the load is accompanied by the simultaneous diffusion of lithium ions from the anode to the cathode through the electrolyte occurring within

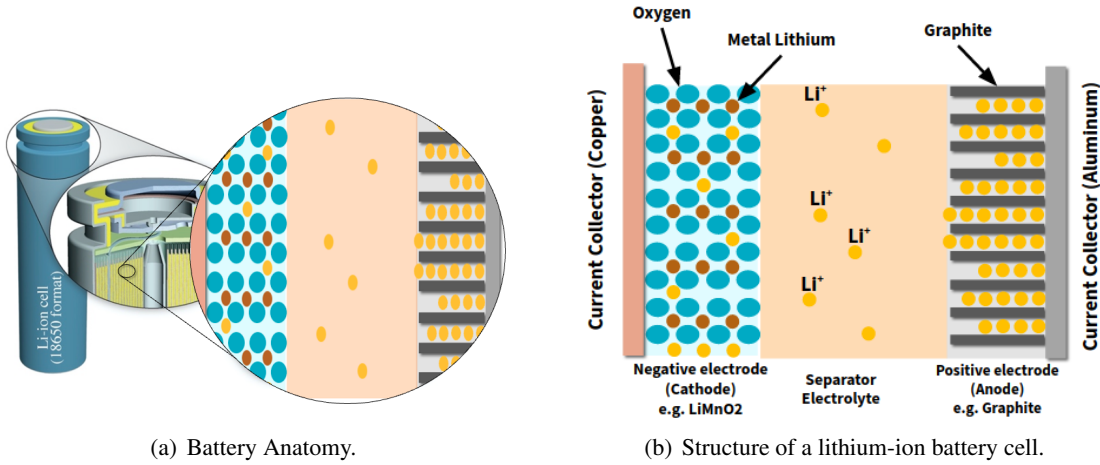


Figure 4.1: Components of a cylindrical jelly-rolled lithium-ion battery cell.

the cell.

For EV applications, lithium-ion cells are commercially produced as either jelly-rolled cylindrical cells or prismatic pouch cells, constructed as successive layers of electrode, electrolyte and current collector. Both have their advantages and disadvantages. For example, the cylindrical cell offers durability, but at the expense of low packaging density. On the other hand, the pouch cell has a large surface area suitable for cooling but requires a heavy protective case which adds a significant amount of weight to the overall battery pack. Further classification of lithium-ion batteries is done by the chemical compound used at the positive electrode – with a long cycle-life, the crystalline allotropic form of carbon (graphite) remains as the best negative electrode today. These cathodes typically are in the form of a layered spinel-rock salt which undergoes a transition phase as lithium is being intercalated and deinterlaced during discharging and charging respectively. A comparison of common cathode compounds by [86] is provided in Figure 4.2. With high scores in safety and lifespan, we can see why lithium-iron-phosphate (stoichiometry: $LiFePO_4$, abbreviated LFP) is used in many ground transportation EV applications such as buses where weight is not a major design concern. However, in aerospace applications where weight is a limiting factor, cathodic chemistries such as lithium-nickel-manganese-cobalt-oxide (stoichiometry: $LiNiMnCoO_2$, abbreviated NMC) and lithium-nickel-cobalt-aluminum oxide (stoichiometry: $LiNiCoAlO_2$, abbreviated NCA) are preferred. The NMC cell has a similar energy and power density to the NCA

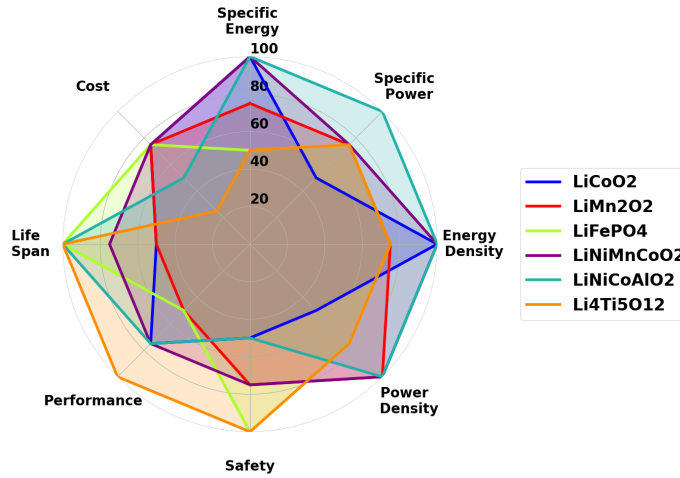


Figure 4.2: Comparison of lithium–ion battery chemistries [5].

cell but outperforms the NCA cell in the metrics of safety and cost of sourcing raw materials for cell manufacture. In this study, the cylindrical NMC cell developed by Panasonic is used in the computational model of the lithium-ion cell.

4.3 Current State of Lithium-Ion Battery Modeling

The ability to accurately predict the amount of energy remaining in a cell, the intensity of the current load being drawn from it and the temperature at the core and surface of the cell any given instant of time is critical for ensuring safe operating and the longevity of the cell. Before we discuss approaches to measure these properties, it is important that we establish common terminology to avoid confusion later down in this chapter and subsequent chapters. From henceforth, any inference of a "cell" pertains to one cylindrical NMC cell, the smallest independent source of stored energy while a "module" implies a collection of these cells electrically connected in some regular arrangement. One level higher is a pack, constructed by connecting multiple modules together to form the unified energy source of an EV.

With that, we now turn our attention to the two most common metrics used to describe the battery: State of Charge (SOC) and State of Health (SOH). SOC is defined as the energy remaining

within a cell or entire battery pack¹ as a percentage of its fully-charged state. SOH is a figure of merit describing the condition of the battery relative to its initial², ideal condition. The battery management system (BMS) in EVs is responsible for estimating SOC and SOH within the pack as well as balancing the load experienced by cells to ensure that no one cell is overcharged during charging or loaded past its lower threshold upon discharging.

SOC and SOH can either be determined experimentally or by numerical simulation. In terms of experimental means, coulomb counting using the Adaptive Kalman Filtering method [87–89] has been one of the most widely implemented techniques for estimating SOC of a cell. These approaches do however require high precision instruments, making them impractical for on board BMS applications. With respect to numerical simulation, the computational approaches for SOC and SOH estimation fall under one of two categories. First are empirical or phenomenological-based models that represent the battery as an equivalent circuit or supposition of algebraic and logarithmic functions whose response and behavior mimic that of the cell. The parameters of these models are tuned using experimental data and some form of regression, for example in [90–92] for SOC estimation and [93, 94] for SOH estimation. Equivalent Circuit Models (ECMs) predict the behavior of a battery cell via a system of ordinary differential equations (ODEs) and are easy to implement. They are also computational inexpensive and therefore best suited for data-driven modeling and online prediction applications such as on a BMS. They however suffer from the reliance on large amounts of experimental data and can at times display low accuracy at high and low SOC. They by themselves are also unable of providing insight into the internal properties of the battery cell as well as exhibiting poor extrapolation behavior. Algebraic models such as the one developed by [95] on the other hand do not require an ODE solver to obtain state variables. Nonetheless, they do suffer the same fate as ECMs when it comes to the requirement of test data for fitting and regression as well as for extrapolation performance. Additionally, both types of low fidelity models are chemistry and cell-type (cylindrical or pouch) specific limiting their application to a particularly class of battery pack.

¹One assumption here is that all of the cells are drained proportionally.

²Though battery cells can be through as identical, manufacturing defects and variability from internal chemical reactions when the organic electrolyte comes into contact with the electrode often leads to cases where some cells in the battery module have a maximum capacity lower than the rated value. At the beginning of operation, SOH among cells typically range between 97-99%

The physics-based electrochemical approach that tracks the behavior of the phase changes of the internal structure of the cell is the other alternative to computationally estimate SOC and SOH. Examples of such models include the porous electrode Doyle–Fuller–Newman (DFN) model and the single particle model (SPM) [96]. In these models, mass and energy conservation laws and kinetics are described by a system of partial differential equations allowing physical insight into the behavior and phase changes of the internal structure of the cell. Unlike empirically driven models, these models tend to have high accuracy over wide operating regions and more recently have encompassed degradation mechanism through a loss factor that accounts for LAM. One major drawback to physics-based models however is the expensive nature of simulations.

Last but not least, all batteries have an ideal temperature range for optimal operation. Below this range, the battery's energy-capacity decreases and above this range the potential of a safety hazard significantly heightens. The speed at which fires can erupt and the catastrophic nature of these explosions make thermal runaway an important issue in lithium-ion battery use. Accordingly, it is crucial to monitor and control the temperature of a battery through a thermal management system that ensures operation within safe margins to prolong cycle life. To design a robust BMS, the cell behavior must therefore not only be characterized at optimal conditions but in off-design conditions that reflect the temperature fluctuations in different geographic locations around the world. This includes cities that have cold climates due to latitude or altitude such as Moscow and Denver respectively, as well as cities where temperatures can soar over 40 °C (104 °F) such as Sydney. The use of computational modeling to predict heat generation and assess cooling strategies to remove battery-generated heat has proven to be an efficient and cost-effective method of extending shelf life [97]. For example, Zhao et al. [98] sought to prolong battery life by minimizing thermal runaway through natural and forced cooling strategies. This work was extended by Wang et. al [99] in their assessment of the impact of cubic, hexagonal and circular cell arrangements on the maximum pack temperature. However, in the two previously-mentioned studies, the discharged current was held constant. Alston et al [100] was one of the first studies to use a power profile of an electric vehicle, thus generating a more realistic thermal profile of the battery pack. In this work, SUAVE is used in a similar manner to generate the realistic power profiles that the battery of an electric GA aircraft would experience during flight.

4.4 Electrification Within the Aerospace Industry

Lithium-ion batteries has proven to be one the key enabling technologies for electric vehicle certification. This has to the fore attention on how these stored energy systems are modeled. This concern unfortunately has not quite yet been reciprocated at the early stages of conceptual design where choices can have detrimental ramifications into the realization of a concept. At present, computational designers have resorted to blanket assumptions and simplified representations for battery pack parameterization as well as performance. Many of these assumptions have manifested in less than credible results in terms of estimating system performance. The first crippling assumption is that the performance and energy storing capacity remains constant through the cell's operational lifetime. Oftentimes, the models employed are incapable of capturing such performance degradation, weakening the optimistic claims, particularly with respect to range, airspeed, charging time. Additionally, there has been little attention to the discussion of the creation of a safe, non-flammable electrolyte with a large operating window for aerospace applications. When the cell is fully charged, the electrolyte and electrode become more reactive and can react with one another, forming this passivating solid electrolyte interface (SEI) layer containing lithium. Although this byproduct coats and protects the electrodes preventing further corrosion, it is irreversible. This consumption of lithium ions to form the SEI layer reduces the concentration of ions to facilitate energy storage, resulting in a reduction in the overall capacity [101, 102]. Such a process is referred to as the loss of active material (LAM). Failure to capture this diminishing behavior leads to the over-prediction of system-level performance which can lead to the inability of an electric vehicle (EV) to meet its intended range. As a result, battery-life studies should be considered an important practice for evaluating long-term flight operations and estimating market potential.

A second example of blanket assumptions made during the conceptual design stage which have a detrimental impact on the overall progress of realizing electrical aircraft is that of lumped thermal models where designs assume that the thermal behavior of individual cells of the battery pack can be ignored. This assumption has to led to disagreement between aircraft designers and battery experts pertaining to the operational limitations of these electrochemical cells. This disconnect will become even more apparent in UAM operations which intend to deploy EVTOL aircraft that

consume large amounts of energy during transitioning approach and departure procedures as noted by[103]. Furthermore, with go-around maneuvers, weather-related alternative landings and congestion at vertiports, realistic UAM operations can lead to significant departures from the standard eVTOL power profiles.

To address the aforementioned shortcomings, a comprehensive three-stage semi-empirical model developed my [5] is used . This first stage is an electrical discharge model capable of capturing the steady-state and transient responses of the battery during charging and discharging. The second stage is a thermal model that applies principles of forced-convection to quantify the thermal load on individual cells. The last stage estimates the simultaneous decay of the cell's capacity and increases in internal impedance. This detailed approach to capturing transport phenomena within the cell during continuous operation falls between simple first-order approximations and more computationally-intensive methods such as finite element analysis, thus earning the classification of medium-fidelity. This model is able to provide reasonably accurate estimates of state variables over an extended period of simulated operation at a fraction of the computational cost of SPM, making them attractive for iterative design approaches. Together with the other components of the aircraft's powertrain, the designer is able to observe electrothermal behavior of the cell that may go unnoticed at the system level.

4.5 Lithium-Ion Battery Modeling for Electric Aircraft Architectures

The following section outlines each of the three elements of the holistic model to simulate the performance of the cells that constitute the battery module in the battery pack. First is the electrical discharge and charging model, followed by the thermal model used to capture heat flux through the module during flight, and lastly the cell aging or degradation model.

4.5.1 Electrical Discharge/Charge Model

The ECM implemented is based on the Thevenin circuit is used in this study to predict the voltage and current that the cell provides at a particular SOC. It is capable of characterizing critical electric properties such as the transient response of the discharging load during operation. This

characteristic of this first-order ODE model is critical for predicting battery performance under the high-frequency load modulations generated by the motors as the aircraft trims. Despite these fluctuations being a characteristic of all aircraft, this phenomenon is more pronounced for EVTOL-type aircraft that have perform trimmed maneuvers using vectored thrust propulsors that are offset from center of gravity of the aircraft. As depicted in Figure 4.3, the model comprises four components: the open-circuit voltage (V_{OC}), the ohmic resistance (R_0), the polarization resistance (R_{Th}) and the polarization capacitance (C_{Th}) which captures the transient response. Properties of the cell used in this work are given in Table 4.1. Experimental data from [1] was aquired to generate surrogate models for cell voltage as a function of temperature, current and SOC, while correlations the other state variables, R_0 , R_{Th} and C_{Th} , are provided in Equations 4.1 below and were taken from from [104].These expressions for these state variables, provided in Equations (4.1a) to (4.1d), were developed through regression of pulse polarization experimental test data.

Table 4.1: Properties of the Panasonic NCR18650G cell [1].

Parameter	Value
Nominal Voltage (V)	3.6
Nominal Capacity (mAh)	3550
Standard Charge (CC-CV)	1.305A - 4.2V
Diameter (mm)	18.5
Height (mm)	65.3
Weight (g)	48.0
Specific Heat Capacity (J/kgK)	1007

$$R_0 = 0.01483SOC^2 - 0.02518SOC + 0.1036 \quad (4.1a)$$

$$R_{th} = -1.212e^{-0.03383SOC} + 1.258 \quad (4.1b)$$

$$\tau_{th} = 2.151e^{2.132SOC} + 27.2 \quad (4.1c)$$

$$C_{th} = \frac{\tau_{th}}{R_{th}} \quad (4.1d)$$

Using the above expressions, the voltage across the parallel resistor-capacitor combination as well as the terminal voltage (V_{UL}) to the propulsion system and powered electronics can be determined

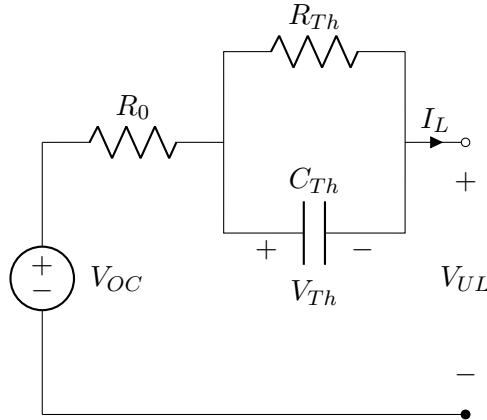


Figure 4.3: Thevenin Equivalent Circuit.

as follows:

$$\frac{dV_{Th}}{dt} = \frac{I_L}{C_{Th}} - \frac{V_{Th}}{R_{Th}C_{Th}} \quad (4.2)$$

$$V_{UL} = V_{OC} - V_{Th} - I_L R_0 \quad (4.3)$$

4.5.2 Thermal Model

As previously alluded to, battery packs of electric vehicles typically comprise a number of smaller units called modules that are electrically connected in series and parallel to meet the power and energy requirements. Two examples of such layouts are provided in Figure 4.4 for an automobile and aircraft. On the left is the X-57 battery pack with 16 modules each comprising of 320 cells and on the right is the Model S with 16 modules, each comprising of 432 cells. Similarly in this work, the battery packs of the four aircraft were modeled as separately connected units, implying that the thermal analysis of the pack is confined to the cells situated in a given module. Under the assumption that the electrical load is evenly distributed among the modules, we, therefore, focus our attention on one module within a given battery pack.

Akin to an electrochemical system, the operating conditions dictate the efficiency of energy conversion. The ability to accurately predict cell temperature is therefore not only critical for ensuring cells perform to their peak potential but cells are regulated to avoid thermal runaway, a phenomenon

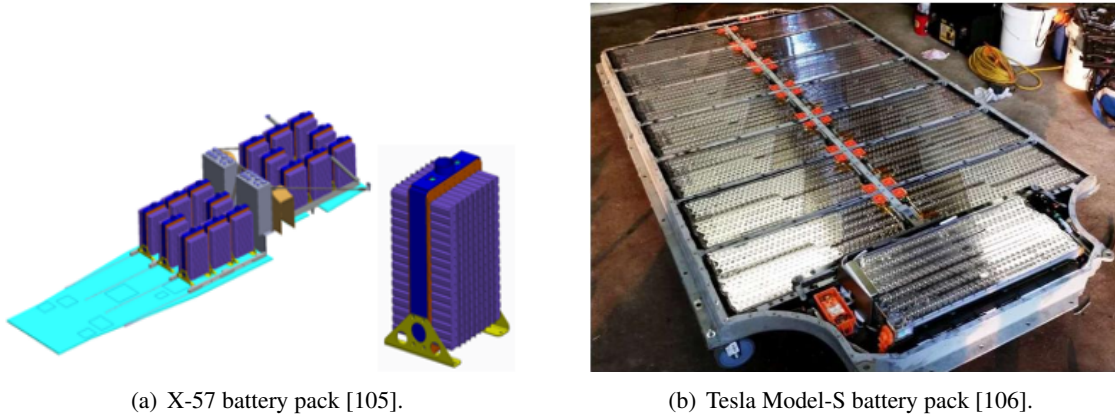


Figure 4.4: Comparison of land and air EV battery pack.

which can either be gradual or explosive depending on the type of failure. The thermal model presented below is the second component of the holistic battery simulation model. It balances the heat generated by the cell during operation with convective heat dissipation into the surroundings. Within each cell, the temperature and heat-generation rate is determined through the conservation of energy and Gibbs function using a relation by Bernardi [107] and detailed below in Equations (4.4a) to (4.4c). These expressions capture temperature changes as a result of electrochemical reactions within the electrodes and separating electrolyte, phase changes at the cathode and Joule heating [108]. Four assumptions governing this heat generation were made. These were (1) homogeneity of the cell's internal structure; (2) the temperature-independent thermophysical properties; (3) uniform distribution of the internal heat source in all directions; and (4) an absence of thermal radiation and convective heat transfer within the battery cell. The first assumption was deemed acceptable based on work by [109–111] which demonstrated that a detailed cell structure had little effect on the thermal behavior of the battery. As a result, a single value was used to represent the specific heat capacity of the cell. Regarding the second assumption, studies in [112] suggest that properties such as freezing point, boiling point, viscosity and conductivity of the electrolyte and electrodes do not change significantly between 0°C and 50°C, allowing us to assume temperature independence. The third assumption is acceptable based on work by [113] which demonstrated that for small cylindrical lithium-ion cells, electrochemical properties inside the battery tend to be homogeneous and

isotropic. The last assumption can be made given the limited mobility of the liquid electrolyte in a lithium-ion battery as pointed out by [114].

$$\dot{q}_{heat} = \dot{q}_{Joule} + \dot{q}_{entropy} \quad (4.4a)$$

$$\dot{q}_{Joule} = A_e i (V_{OC} - V_{UL}) = \frac{i^2}{\sigma} \quad (4.4b)$$

$$\dot{q}_{entropy} = -I \left(T \frac{\delta V_{OC}}{\delta T} \right) = -T \Delta S \frac{i}{nF} \quad (4.4c)$$

The first term on the right-hand side of Equation 4.4a accounts for the ohmic losses inside the battery cell which typically occurs at the SEI layer adjacent to the anode, charge transfer overpotential at the electrode-electrolyte interfaces and the mass transfer limitations. The second term is captures generated entropy often referred to as reversible heat. Entropic heat is generated when the lithium content of the electrode changes, causing the entropy of the electrode materials to change. The total electrode area is used to compute the current density, i . For the NMC cell used in this study, the entropy change, ΔS , is given as a function of SOC as obtained from [108]. This relationship is a sixth-order polynomial fit to experimental data obtained from [115].

$$\begin{aligned} \Delta S_{LiNi_xCo_yMn_zO_2} = & -496.66(SOC)^6 + 1729.4(SOC)^5 - 2278(SOC)^4 + 1382.2(SOC)^3 \\ & -380.47(SOC)^2 + 46.508(SOC) - 10.692 \end{aligned} \quad (4.5)$$

Air cooling has risen to be one of the most practical solutions for reducing takeoff gross weight. We therefore adopt atmospheric air as the coolant within each battery module which is modeled as a tube bank in a crossflow. Empirical formulations outlined in [116] were used to estimate the heat removed from this system where the flow conditions are dominated by boundary-layer separation effects and turbulent wake interactions. A prior studies by [105] implemented lumped models that oversimplified the interactions between the individual battery cells and the coolant by ignoring the geometry of the cell itself, the area expected to such cooling fluid and lastly specific layout within

the module. The result of these limited heat transfer models is the inability to accurately analyze thermal distribution within the module, making any attempt to optimize cell performance futile. Additional assumptions regarding the layout of the battery module shown in Figure 4.5(a) were based on packs produced by Toyota [117]. Here, the simplest reduced-order model is employed where the battery cells can be considered to have the same temperature. The layout is characterized by the cell diameter, D , transverse pitch, S_T and longitudinal pitch, S_L . Cell rows were staggered in the direction of the flow velocity, V_∞ as shown in Figure 4.5(b). The values for these parameters used in this study are summarized in Table 4.2. These assumptions are appropriate for aircraft conceptual design as it provides sufficient information for a detailed analysis without introducing additional uncertainty.

The average heat transfer coefficient for the entire module can be determined using the relationship between Nu , which provides a measure of the convective heat transfer occurring at the surface of the cell, and Re , which represents the ratio of the inertia to viscous forces. This relationship is given below:

$$Nu = \frac{\tilde{h}D}{k_f} \quad (4.6)$$

Here, k_f is the thermal conductivity of the cooling fluid. Nu can be estimated through correlations by [118] based on Re characterizing the maximum flow in the tube bank, $Re_{D,max}$. The constants used in Equation 4.7 below can be found in [116] and are provided for different flow velocities and tube arrangements.

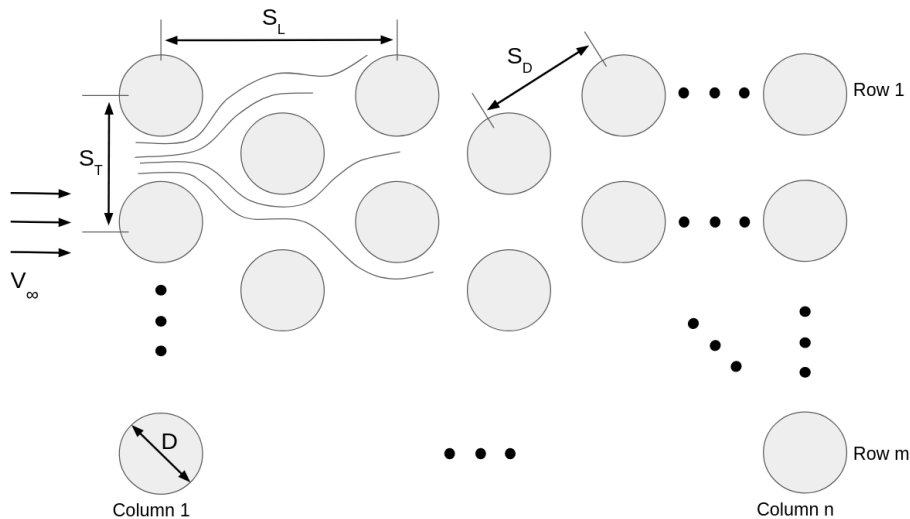
$$Nu = C Re_{D,max}^m Pr^{0.36} \left(\frac{Pr}{Pr_w} \right)^{0.25} \quad (4.7)$$

$$\text{where } \begin{cases} C = 0.35 \left(\frac{S_T}{S_L} \right)^{0.2} \text{ and } m = 0.6, & \text{if } Re_{D,max} > 1 \times 10^3 \\ C = 0.51 \text{ and } m = 0.5, & \text{otherwise} \end{cases}$$

Pr and Pr_w are the Prandtl numbers of the fluid at the inlet and near the surface of the battery cells



(a) An EV battery module.



(b) Staggered cell arrangement.

Figure 4.5: Battery module design.

respectively. $Re_{D,max}$ are determined using S_T and S_L as follows:

$$Re_{D,max} = \frac{V_{max}D}{\nu} \quad (4.8)$$

where $V_{max} = \begin{cases} V_\infty \frac{S_T}{2(S_D - D)}, & \text{if } 2(S_D - D) < (S_T - D) \\ V_\infty \frac{S_T}{(S_T - D)}, & \text{otherwise} \end{cases}$

Here, the diagonal distance S_D can be determined as follows:

$$S_D = \sqrt{S_T^2 + S_L^2} \quad (4.9)$$

Table 4.2: Geometry and coolant (air) flow conditions of the battery module.

Parameter	Value
V_∞ (m/s)	0.1
S_T (mm)	20
S_L (mm)	20

This model can be easily modified for in-lined tube bundles and different numbers of cells parallel or perpendicular to the direction of the cooling fluid. The temperature difference between the cell surface and the outlet temperature can then be determined using Equation 4.10, which, in turn, is used to determine the log mean temperature difference, ΔT_{LM} .

$$\frac{T_w - T_o}{T_w - T_i} = \frac{\exp(-\pi D N_{tot} h)}{(\rho_\infty V_\infty N_T S_T c_{p_\infty})} \quad (4.10)$$

$$\Delta T_{LM} = \frac{(T_w - T_i) - (T_w - T_o)}{\log \left(\frac{T_w - T_i}{T_w - T_o} \right)} \quad (4.11)$$

where N_{tot} is the total number of cells in the module. The convective heat transfer from the battery can then be computed:

$$\dot{q}_{convec} = N_{tot} \tilde{h} A_s \Delta T_{LM} \quad (4.12)$$

The net heat load \dot{q}_{net} and the cell temperature rise $\frac{dT}{dt}$ can be quantified using the following equations:

$$\dot{q}_{net} = \dot{q}_{heat} - \dot{q}_{convec} \quad (4.13a)$$

$$\frac{dT}{dt} = \frac{\dot{q}_{net}}{m C_p} \quad (4.13b)$$

4.5.3 Aging Model

To facilitate large scale simulation for the selected aircraft under a variety of flight conditions, a semi-empirical degradation model was the preferred approach. This model was inspired by [119] and [120] and possess several attractive characteristics including the ability to capture the influence of temperature and voltage on calendar aging, as well as the effect of depth of discharge (DOD) and SOC on cycle aging. As with the case of stored-energy cells, performance degrades with repeated cycling from a variety of factors including an increase in SEI, deterioration of the once pristine electrodes, and the loss of active material. The model used to characterize the reduction in cell capacity and growth of internal resistance within the cell was developed by [120]. Tailored for the cell chemistry and type, this model has the added benefit capturing both the DOD and \bar{V} , the quadratic-average voltage in its formulation. This feature allows us to directly assess separate segments of the flight profile individually and quantify the sensitivity of certain flight maneuvers on the overall aging of the battery. The model fits a physics-based model to experimental data and consists of an impedance-based electric-thermal model coupled with accepted metrics for predicting cell degradation. Given in Equations 4.14a to 4.14d, the electrical load, V , ambient air temperature, T and DOD are used to determine stress factors caused by volumetric changes during intercalation and deintercalation of lithium in the cathode and anode.

$$\alpha_{\text{cap}} = (7.543V - 23.75)10^6 e^{-\frac{6976}{T}} \quad (4.14\text{a})$$

$$\alpha_{\text{res}} = (5.270V - 16.32)10^5 e^{-\frac{5986}{T}} \quad (4.14\text{b})$$

$$\beta_{\text{cap}} = 7.34810^{-3}(\bar{V} - 3.667)^2 + 7.60010^{-4} + 4.08110^{-3}\Delta\text{DOD} \quad (4.14\text{c})$$

$$\beta_{\text{res}} = 2.15310^{-4}(\bar{V} - 3.725)^2 - 1.52110^{-5} + 2.79810^{-4}\Delta\text{DOD} \quad (4.14\text{d})$$

α_{cap} and α_{res} are coefficients that capture calendar aging for the cell capacity and resistance respectively while β_{cap} and β_{res} coefficients defining cycle aging. The superposition of calendar and cycle aging coefficients provides the total aging function for the battery energy-capacity fade, E_{Fade} , and the internal resistance growth, R_{Growth} respectively. As shown in Equation 4.15, these

two quantities are computed as normalizations to the initial state of the battery. Here, t is the aging time in days while, Q , the charge throughput in amp-hours, is interpreted as the amount of charge that has passed through a battery cell in its lifetime.

$$E_{Fade} = 1 - \alpha_{cap} t^{0.75} - \beta_{cap} \sqrt{Q} \quad (4.15a)$$

$$R_{Growth} = 1 + \alpha_{res} t^{0.75} + \beta_{res} Q \quad (4.15b)$$

4.6 Validation of Battery Model

Validation of the full battery pack unit is challenging for many reasons. First the cost associated with simulating realistic loads on packs is both expensive and dangerous, requiring significant quality control.

In a research setting, this would entail the integration of hardware such as transformers and super-capacitors that can produce the characteristic voltage and current loads that these aircraft will exhibit because such loads cannot be simply drawn from the standard power outlet. Outsourcing the testing campaign to a vendor, be it private or government also poses its own set of challenges as these entities may be reluctant to share sensitive and valuable data that grants them a competitive advantage. Even if these resources were made readily available, the data is expensive to obtain, both in terms of the need for high precision instrumentation and secondly in terms of the length of time for test protocols to run – running protocols and intermittent diagnostic tests to capture the effect of C-rates on cell performance can take about months. Validation of batteries is general has thus proven to be laborious task. As a result, industry, and to some extent academia, are reluctant to share testing data for competitive advantage.

The experimental data used to validate the models discussed in this work therefore comes from the small sample of published literature that has been made public. It was carried out in part through an examination of thermal loads arising from electrical discharge then a comparison of predicted cell degradation to experimental data. The inability to experimentally cycle an entire custom-made

battery module over an extended period limited the scope of validation to the individual cells rather than the entire pack. A possible source of error therefore originates from the high uncertainty of the heat removed from the module. This will be tackled in future work through large-scale experimentation. Observed in Figure 4.6(a) is a comparison of the predicted thermal response of the NMC cell with experimental tests conducted by [108] when subjected to two different discharge rates. Similarly, the aging model was validated using experiments by [119] on a cell cycled at 35° C at 1C. Figure 4.6(b) depicts the depletion of capacity as well as an increase in internal resistance at various cycle depths. For example, a cycle depth of 75-25% implies that the cell was cycled from SOC of 0.75 to 0.25.

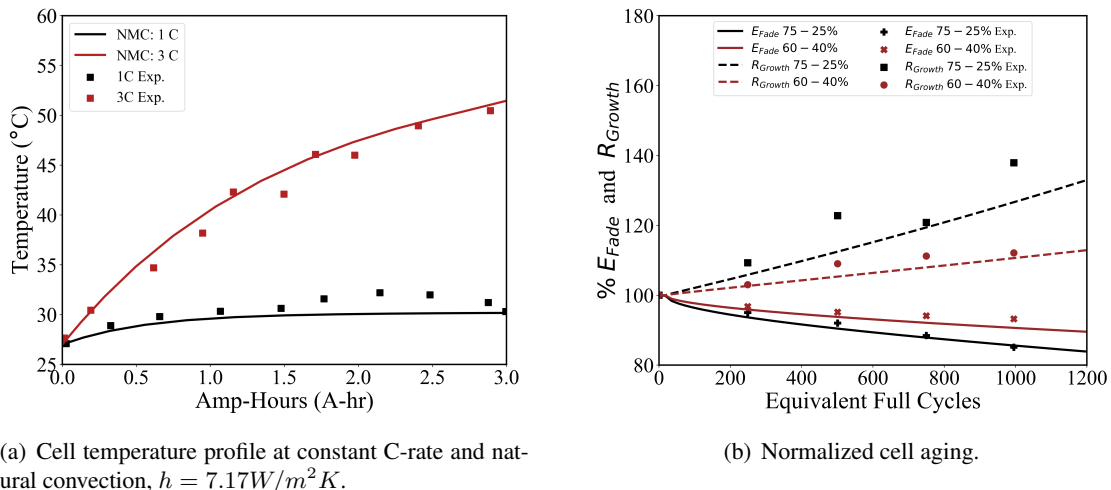


Figure 4.6: NMC cell validation.

4.7 Chapter Summary

In this chapter, we document the three-part model used for estimating the state of charge and other electrical circuit attributes of the cell over extended operation. These models were all empirically driven, implying that prediction of voltage, temperature, current, capacity fade, resistance growth among other variables can be computed cheaply, making it ideal for integrating into the SUAVE framework for predicting the performance of electric powertrains. This will be covered in

Chapter 5 where comparisons of the performance of the four aircraft are made and again in Chapter 6 where we discuss there a relationship between aircraft noise and battery performance. That being said, there are a few assumptions made in the formulation of the model worth mentioning. The first was the use of a constant specific heat capacity to characterize the thermal load of the NMC cell. In actuality, cylindrical batteries such as the ones used in this work are manufactured by placing multi-layer electrodes and a diaphragm into the electrolyte in the form of a spiral structure. This makes the conductivity inside the battery anisotropic [121]. Additionally, it must be noted that though the model presented in this paper is specific to cylindrical NMC cells, the methodology can be applied to other cell structures or chemistries once equipped with information to update the respective discharge, thermal and aging models. Future work includes relaxing this assumption and implementing a semi-empirical model that can predict the non-uniform thermal behavior within the cell. This will affect the cell's internal resistance behavior and holistically the macro-electrical properties of the entire pack. Another area of future work specific to battery modeling is the division of the cells within the module into thermal zones. This can be used in tandem with experimental data to predict heat sinks within the module based on the specific cooling strategy employed.

Chapter 5

RUAM Aircraft Baseline Studies: Performance and Acoustic Footprint

5.1 Introduction

It was only until recently [122] that the true potential of SUAVE analyzing of non-conventional aircraft was featured through the design and analysis of drastically different EVTOL configurations. Admittedly, the capability to critically assess the performance of specific components right up to system-level manifests itself as a double-edged sword. On one end, the user possesses the ability to ascertain deeper understandings of subsystem interactions. On one other, the application of physics-based approaches to study the dynamics of isolated components as well as their coupling interactions presents issues pertaining to numerical convergence within the mission solver. For example, the solver may return nonsensical results, for instance, negative thrust and torque if components of the energy network are not adequately sized or a particular flight segment exceeds physical limitation of the powertrain systems. Ultimately, SUAVE’s garbage-in-garbage-out code philosophy ensures that any errors made by designer during sizing or difficulties encountered by the solver while attempting to arrive at a set of state variables do not remain overlooked. For recollection, these variables include attributes such as vehicle angle of attack and the engine throttle to generate the forces required to perform the specified flight segment. This throttle is defined as the ratio of commanded thrust or

power.

This chapter serves as the focal point of the work presented in this dissertation. The aeroacoustic prediction method along with the battery-powered energy network model developed in Chapters 3 and 4 respectively are integrated into SUAVE framework to assess select aircraft and draw concrete conclusions meant to guide the aerospace community developing solutions for a RUAM ecosystem. We first begin in Section 5.2 with a summary of the four electric aircraft conceived to represent the major classes of RUAM passenger-carrying vehicle configurations. This also encompasses the methodology undertaken for sizing lifting surfaces and the propulsion architecture as well as a weight breakdown of the each aircraft. Following this review is the breakdown of the flight profiles which each vehicle is simulated then an in depth discussion on aircraft performance over a single flight. Finally in Section 5.5, we look at the degradation of vehicle performance over a prolonged period of operation.

5.2 Electric Aircraft Configurations

The four electric aircraft studied in this dissertation are an electric conventional takeoff and landing (ECTOL) aircraft, a stopped-rotor aircraft, a tilt-wing and multi-rotor aircraft. Their distinct configurations span the four major categories of aircraft envisioned to facilitate RUAM operations - conventional tube-and-wing, lift+cruise, vectored thrust and multi-rotor EVTOL aircraft. Inspiration for their designs were taken from tech-demonstrators in existence today, namely NASA's X-57 Maxwell Modification II, Wisk Aero's Cora, Airbus's Vahana and CityAirbus' demonstrators respectively. These aircraft were selected based on the abundance of publicly available geometric parameterizations and subsystem specifications of these aircraft. Renderings of the four aircraft are shown in Figure 5.1. The ECTOL aircraft is a high-wing model with engines mounted near the mid-span on each wing. This aircraft requires takeoff field lengths around 2200 feet, nearly two orders of magnitude greater than EVTOL aircraft, limiting its operation to standard airports with runways. The stopped-rotor EVTOL aircraft is of the lift+cruise category, characterized by separate powertrains for vertical climb and forward flight. The transition between hover and cruise here is made possible through the co-action of these separate propulsive systems. Estimating the electrical

load drawn by the motors during the transitioning phases of flight for this type of vehicle is somewhat non-trivial as medium to high fidelity computational methods are required if one wishes to accurately predict the forces and moments about the vehicle. Third is the tandem tilt-wing EVTOL aircraft which is of the vectored-thrust type. The particular model designed in this work possess eight engines, with four mounted on both the front canard wing and rear main wing. Both wings however do have equivalent spans, aspect ratios and tapers. This vehicle uses a combination of lifting surfaces and thrust-vectoring to perform its transitioning maneuvers. Last is the multi-rotor EVTOL aircraft, a hexacopter with engines mounted above the fuselage using struts (not displayed in Figure 5.1).

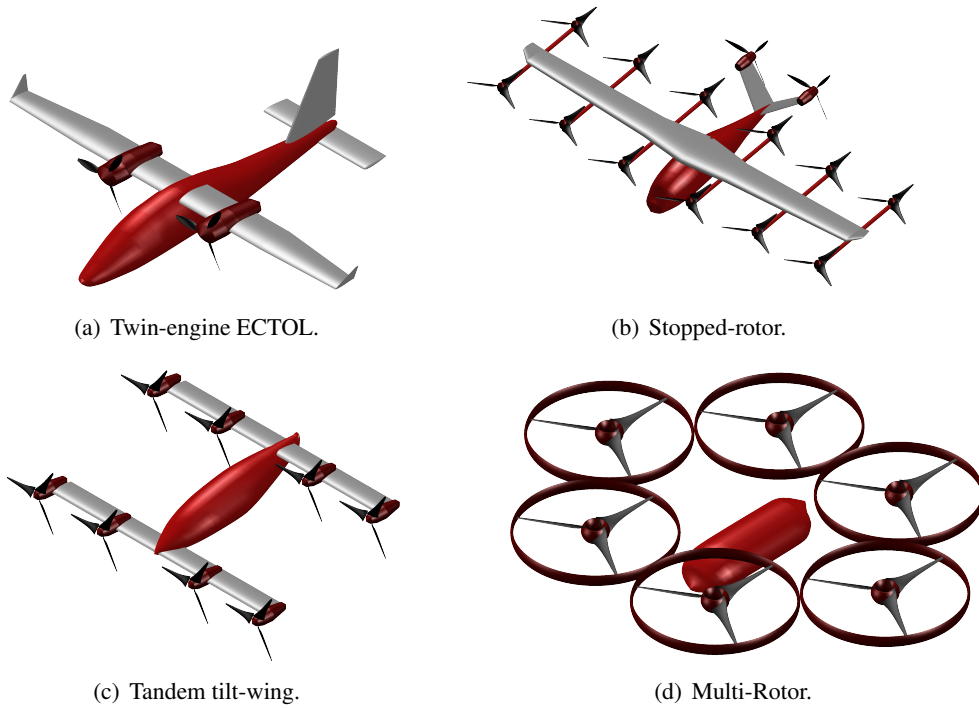


Figure 5.1: Electric aircraft models.

The aircraft are all designed to carry 6 passengers or an equivalent payload of 925 lbs. A full breakdown of vehicle dimensions and powertrain attributes is provided in Table 5.1 including the layout of battery the pack configurations. Here, (\parallel) represents the number of cells parallel to the cooling airflow while (\perp) represents the number of cells perpendicular to the cooling airflow with a

module. Additionally, "s" denotes the number of units (cells or modules) in series and "p" denotes the number of units in parallel. Lifting surfaces other integral components of the four aircraft were sized based on design loads estimated by the physics-based weight build-up method discussed in Section 2.3.4 of Chapter 2. The following section provides a more descriptive outline of component sizing, including the sub-optimization problems.

5.2.1 Vehicle Component Sizing

With the exception of the multi-rotor, the design cruise speed was chosen to be 175 mph - a lower airspeed of 75 mph was chosen due to constraints surrounding blade tip Mach and the extent of reverse flow on the retreating side of the blade in edgewise flight. The following subsections expand on some of the primary domains of the aircraft conceptual design process, particularly aerodynamics and construction of the energy network.

5.2.1.1 Aerodynamics and Stability: Wing Sizing

The main wings of the winged concepts were sized and positioned to achieve trimmed flight and a minimum lift-to-drag ratio around 15 the design cruise speed and altitude. This optimization was performed on the clean wing planform, neglecting interference of booms and nacelles. To minimize the number of design variables in this sub-optimization to parameterize the wing, planform area, S_{ref} , aspect ratio, AR , root twist, θ_r , and tip twist, θ_t , were chosen as the only design variables. All other geometric properties were determined through the following assumptions: (1) a linear twist from wing root to wingtip; (2) the ratios of wing chord segments along the wing are held fixed; (3) the percent location of wing segments are held fixed in the spanwise direction. The other design variables were the location of all lifting surfaces, x_{w_i} , relative to the nose of the aircraft. This includes main wings, tandem wings, v-tails and horizontal tails depending on the configuration. Collectively, these design variables are denoted by \vec{X}_{wing} below in Equation 5.1. The center of gravity (c.g.) location is updated each iteration by resolving the moments about a reference point. Along with meeting the target lift constraint, trimmed static stability is achieved by meeting the following three criteria. The first is zero pitching moment about the center of gravity for the clean wing configuration. This implies that control surfaces not deflected. The second is a static margin

Table 5.1: Vehicle parameters.

	ECTOL	Stopped-rotor	Tandem Tilt-wing	Multi-Rotor
<i>General Vehicle Characteristics</i>				
Capacity (pass.)	6	6	6	6
Payload (lbs)	925	925	925	925
Radial Footprint (ft)	36	48	32	39
Reference Area (ft ²)	159	180	234	96
TOGW (lbs)	3527	6113	6007	8381
Battery				
Total Pack Weight (lbs)				
Pack Capacity (kW-hr)	92	179	249	631
Number of Modules	10	10	10	10
Module Geometric Layout ($\parallel \times \perp$)	12×6	14×10	15×13	19×26
Module Electrical Layout ($s \times p$)	12×60	14×100	15×130	19×260
Pack Electrical Layout ($s \times p$)	$10s \times 1p$	$10s \times 1p$	$10s \times 1p$	$10s \times 1p$
Rotors				
Blade Type	2 propellers	2 propellers 12 lift-rotors	8 prop-rotors	6 lift-rotors
Rotor Diameter (ft)				
Propeller	6.3	7.5	-	-
Lift-Rotor	-	7.5	-	16.4
Prop-Rotor	-	-	7.9	-
Motors	$2 \times 83 \text{ kW}$	$2 \times 221 \text{ kW}$ $12 \times 47 \text{ kW}$	$8 \times 108 \text{ kW}$	$6 \times 155 \text{ kW}$
<i>Performance</i>				
Hover Disc Loading (lb/ft ₂)	-	11.5	15.3	6.6
Hover Power Loading (lb/hp)	-	8.1	5.1	6.7
Cruise Speed (mph)	175	175	175	75
Maximum Operational Altitude (ft)	14000	5000	5000	2500

of 15%. This metric can be thought of as a measure of pitch stiffness and is defined as the change in moment coefficient with respect to lift coefficient for the aircraft. Unlike larger passenger aircraft whose static margins can be between 20-40%, a lower value is chosen to ensure that the aircraft possess the favorable maneuverability to transition from hover to cruise with a high degree of control authority. The last criteria is a negative Cm_{alpha} , implying that changes in angle of attack are inversely proportional to the the pitching moment, thus promoting a vehicle response that returns the aircraft to an equilibrium state. An additional constraint of aircraft footprint was included in this optimization ensure that generated certifiable aircraft are able to operate with existing helipad infrastructures. The weight build-up method is called each design iteration to ensure that TOGW is updated and the correct moments are utilized in the center of gravity calculations

$$\begin{aligned}
 & \min_{\vec{X}_{wing}} C_D(\vec{X}_{wing}) \text{ where, } \vec{X}_{wing} = [S_{ref}, AR, \theta_r, \theta_t, x_{w_i}] \\
 \text{s.t.} \quad & L = TOGW \\
 & L/D \geq 15 \\
 & C_M = 0 \\
 & SM = 0.15 \\
 & Cm_{alpha} < 0 \\
 & x_{fp} \leq 50 \text{ ft}
 \end{aligned} \tag{5.1}$$

5.2.1.2 Energy Network: Rotor Sizing

Depending on vehicle configuration, propellers were sized to produce the thrust required at transition or cruise conditions, while lift and prop-rotors were sized to meet the thrust required for hover. The rotors were sized to lift a total weight of the aircraft, divided by the total number of rotors. The other two constraints in this optimization were that of disc loading and tip Mach number. Arriving at the optimal blade geometry was achieved using an adaptation of the methodology developed [123] for designing propellers with minimum power losses. Modifications worth mentioning are a relaxation of the small-angle approximation and the inclusion of sectional airfoil data that accounts for stall as well as compressibility and skin friction drag. In this optimization, the design variables,

collectively denoted \vec{X}_{prop} and \vec{X}_{rot} for the propeller and lift-rotor (and prop-rotor) respectively where tip radius, chord distribution and twist distribution in the blade design process. The hub fraction was held constant at 10 % of the tip radius of the blade. The design approaches for propellers and lift-rotors are given below in Equations 5.2 and 5.3 respectively. The disc loading constraint, DL serves to ensure that the structural integrity of the blade is not compromised due to heaving loading and the tip Mach constraint, M_t ensures that the blades do not approach an operating regime where transonic effects come into consideration

$$\begin{aligned} \min_{\vec{X}_{prop}} \quad & P(\vec{X}_{prop}) \text{ where, } \vec{X}_{prop} = [r, \Theta_r, \mathbf{c}_b] \\ \text{s.t.} \quad & T = D_{cruise} \\ & DL \leq 100 \text{ lb/ft}^2 \\ & M_t \leq 0.6 \end{aligned} \tag{5.2}$$

$$\begin{aligned} \min_{\vec{X}_{rot}} \quad & P(\vec{X}_{rot}) \text{ where, } \vec{X}_{rot} = [r, \Theta_r, \mathbf{c}_b] \\ \text{s.t.} \quad & T = \frac{TOGW}{n_{rot}} \\ & DL \leq 100 \text{ lb/ft}^2 \\ & M_t \leq 0.6 \end{aligned} \tag{5.3}$$

5.2.1.3 Energy Network: Motor Sizing

The approach to sizing the electric motor is outlined in Equation 5.4. Here the objective is to minimize the current drawn from the battery while producing the torque required to match torque produced by the rotor in the previously section at a target efficiency. The design variables are motor speed constant, K_V and internal resistance, R_0 . Battery voltage, V , the angular rate of the motor, Ω given in radians-per-second, and no-load current, I_0 are fixed parameters and should be chosen by the designer based on the power requirements. The philosophy behind such an approach comes from the conjecture that the electric motor market is at the stage where motors can be manufactured

to meet the unique specifications of a particular powertrain.

$$\begin{aligned} & \min_{K_V, R_0} \left(V - \frac{\Omega}{GK_v} \right) / R_0 \\ \text{s.t. } & \left[\left(V - \frac{\Omega}{GK_v} \right) / R_0 - I_o \right] / K_v = Q_m \\ & \left(1 - \frac{I_0 R_0}{V - \frac{\Omega}{GK_v}} \right) \left(\frac{\Omega}{GV K_v} \right) = \eta_m \end{aligned} \quad (5.4)$$

5.2.1.4 Energy Network: Battery Pack Sizing

With the steady development of high energy and power density cells, lithium-ion batteries are leading the race to be the energy storage of choice for electric aircraft. The battery packs were sized to close the missions outlined in Section 5.4. That is, except for the multi-rotor that designed to close a two-legged mission around 37 nmi, the packs were sized to facilitate a two-legged mission of 70 nmi. In this study, the NMC cell manufactured by Panasonic[1] was selected. Properties of this cell are provided in Table 5.2. By using a model of a real lithium battery available on the market today, the results from the flight simulations are guaranteed to be grounded in verisimilitude, departing from prior studies that over-estimate energy and power densities. The inclusion of a tech factor of was made to account for the mass of the BMS, wiring and protective module housing. Given as a percentage of the total battery mass this factor was 1.42 as suggested by [124] for the ECTOL, stopped-rotor and tilt-wing . Due to the shear size of the battery pack for the multi-rotor, a lower factor of 1.1 is used. The optimization approach to determine the number of cells required to achieve these missions is given below where (*) is used above to signify the intended design range for sizing and the subscript *EOF* denotes the condition at the end of flight

$$\begin{aligned} & \min_{\vec{X}_{bat}} TOGW(\vec{X}_{bat}) \text{ where, } \vec{X}_{bat} = [n_s, n_p] \\ \text{s.t. } & Range_{EOF} = Design\ Range^* \\ & SOC_{EOF} \geq 0.1 \\ & C \leq 30 \end{aligned} \quad (5.5)$$

NMC Cell & Pack Parameters	
Property	Value
Mass (g)	48
Height x Diameter (mm)	65.3 x 18.5
Density (kg/m ³)	1760
Specific Heat (J/kgK)	1108
Nominal Voltage (V)	3.6
Nominal Capacity (Ah)	3.55

Table 5.2: NMC 18650 cell properties.

5.2.2 Aircraft Weight Breakdown

Figure 5.2 portrays the mass fractions of the components of the four models. Examining the doughnut charts, it can be seen that battery mass is a significant fraction of TOGW, ranging between 35% of the ECTOL to 65% of the multi-rotor. This reinforces the assertion of many that for battery-powered aircraft, the importance of the rate of battery technology improvement, specifically in the domains of specific energy and specific power, outweighs that of other components of the powertrain such as superconducting electric motors or rotor blade design. This also conveys that, to a large degree, vehicle flight stability and handling quality will heavily depend on weight distribution of the battery pack around the airframe. The inherent nature of EV battery packs to be assembled as separate modules that can be positioned around the vehicle rather than situated in one location as a lumped mass does offer some consolation; designers have some flexibility in positioning modules around the airframe and even in the wings to achieve favorable trim and dynamic stability characteristics. Ultimately, not having to rely on large control surfaces as actuators that contribute to additional weight leads to simpler flight control laws. From the doughnut charts below, other significant contributors to TOGW of the four electric aircraft were the motors (in light blue), wiring (dark green) through the fuselage and wings to power propulsors, passengers (red), fuselage and booms (brown) and wings (yellow).

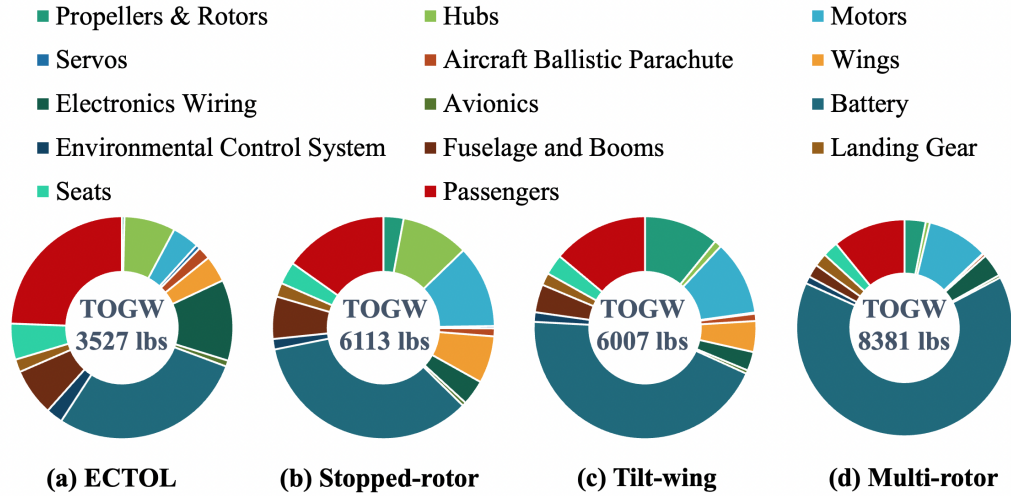


Figure 5.2: Weight fractions of RUAM Aircraft.

5.3 Vehicle Flight Profiles

Realistic flight profiles that conform to regulations documented in the Code of Federal Regulations (CFR)¹ were constructed keeping mission objectives outlined in Section 1.4 of Chapter 1 in mind. Examples of such flight restrictions include service ceilings, maximum air speeds as well as bounds on the climb rates. More specifically, 14 CFR §23 was used for the flight profile of the ECTOL while a combination of 14 CFR §23, 27 and 135 was used for the EVTOL aircraft since policies for such aircraft have yet to be established. In terms of the flight profiles, vehicle trajectories and flight dynamics were meticulously constructed to enforce continuity in rigid body kinematics between adjacent flight segments. Such attention to detail in simulating flights enables us to ascertain trustworthy approximations of vehicle performance. It also offers more valuable perspectives on vehicle performance and one moves away from a system feasibility mindset to a more detailed-oriented approach that benefits personnel working on the aircraft. For instance flight loads engineers can ascertain better estimates of asymmetric loads producing during wind-gusts and other off-design conditions and flight-controls engineers can acquire valuable non-linear coefficients required to construct state-space models representing vehicle dynamics.

¹All CFR Title 14 references in this paper were from the electronic Code of Federal Regulations, <http://www.ecfr.gov>, retrieved from the version updated Apr 23, 2021

Table 5.3: Electric aircraft flight segments.

Segment	ECTOL Aircraft	Stopped-rotor	Tilt-wing	Multi-rotor
1	Take-off	Vertical Climb	Vertical Climb	Vertical Climb
2	Departure End of Runway	Vertical Transition	Vertical Transition	Vertical Transition
3	Initial Climb Area	Climb Transition	Climb Transition 1	Climb
4	Climb	Climb 1	Climb Transition 2	Cruise
5	Cruise	Climb 2	Climb	Descent
6	Descent	Cruise	Cruise	Descent Transition
7	Downleg	Descent	Descent	Vertical Descent
8	Baseleg	Approach Transition	Approach Transition	
9	Final Approach	Descent Transition	Descent Transition	
10	Landing	Vertical Descent	Vertical Descent	
11	Reverse Thrust			

Figures 5.3 and 5.4 depict characteristic flight profiles for ECOL performing a conventional, ground-accelerated takeoff and an EVTOL aircraft performing a vertical ascent respectively. These illustrations serve as the focal point summary of the mission segments for each vehicle is presented in Table 5.3, and are not drawn to scale. This is followed by a more detailed description of the types of flight segments modeled is provided in Table 5.4 and values used to parameterize the flight segments of each simulated aircraft in Table 5.5. This includes altitude, speed, climb rate, rotor orientation angle and pitch command for each segment. These rotor orientation angles are given relative to the body-frame of the aircraft where the positive x points out the nose of the aircraft. For example, a rotor angle of [0°, 90°, 0°] indicates a 90° clockwise rotation about the y-axis pointing out the starboard wing. The axis new about on which the rotor blades revolve about would therefore now aligned with the positive z-axis in the body frame. For brevity in Table 5.5, only the rotations about the positive y-axis rotation are provided since no orientations out of the x-z plane were simulated. The blade pitch commands provided in the 8th column of Table 5.5 is the additional angle added to each blade in the BEVT method described in Chapter 2. For the stopped-rotor, the first value in the rotor orientation and blade pitch command columns correspond to the propeller while the second column corresponds to the lift-rotor. For the tilt-wing , the incidence angles of both the rear main wing and the lower forward tandem wing are also equivalent to rotor orientation angles throughout the mission. Reverse thrust segment for the ECTOL are omitted from the simulation. This is followed by illustrations of the flight profile for the ECTOL and the EVTOL aircraft in Figures 5.3 and 5.4 respectively.

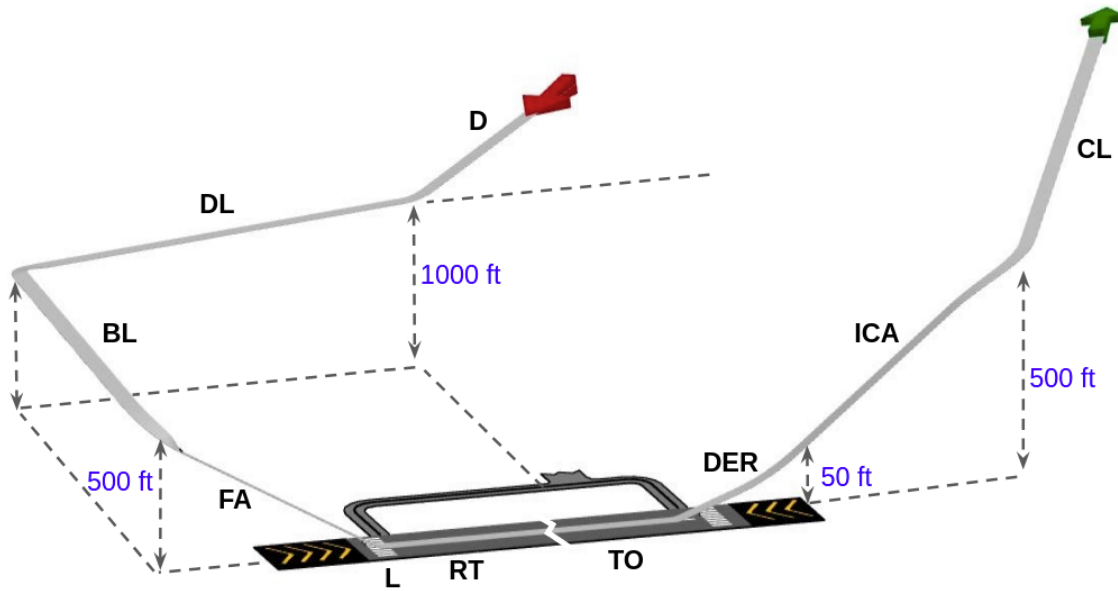


Figure 5.3: Flight profile of an ECTOL aircraft.

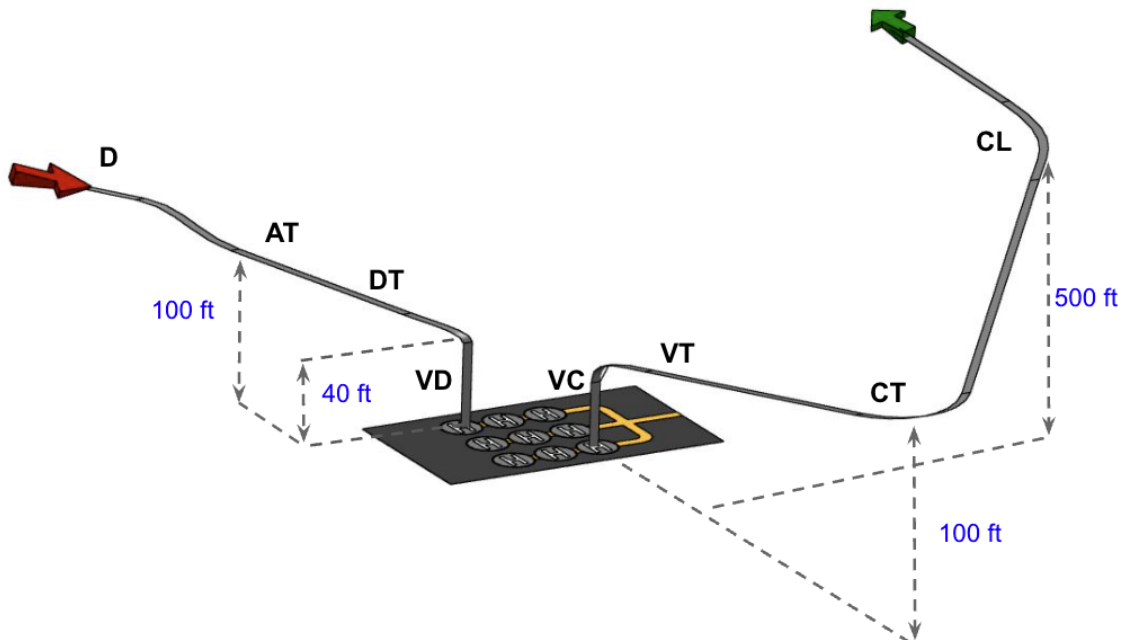


Figure 5.4: Flight profile of an EVTOL aircraft.

Table 5.4: Flight segment kinematics.

Segment	Symbol	Segment Kinematics
Approach Transition	AT	Constant-Acceleration-Constant-Angle-Linear-Climb
Baseleg	BL	Linear-Speed-Constant-Rate
Climb	CL	Linear-Speed-Constant-Rate
Climb Transition	CT	Constant-Acceleration-Constant-Angle-Linear-Climb
Cruise	CR	Constant-Speed-Constant-Altitude
Departure End of Runway	DER	Linear-Speed-Constant-Rate
Descent	D	Linear-Speed-Constant-Rate
Descent Transition	DT	Constant-Acceleration-Constant-Pitchrate-Constant-Altitude
Downleg	DL	Constant-Acceleration-Constant-Altitude
Final Approach	FA	Linear-Speed-Constant-Rate
Initial Climb Area	ICA	Linear-Speed-Constant-Rate
Landing	L	Ground Deceleration
Reverse Thrust	RT	<i>Not Modeled</i>
Takeoff	TO	Ground Acceleration
Vertical Climb	VC	Vertical Ascent
Vertical Transition	VT	Constant-Acceleration-Constant-Pitchrate-Constant-Altitude
Vertical Descent	VD	Vertical Descent

5.4 Assessment of Mission Simulations: Single-Flight Comparisons

Presented in this following sections are the results of the flight simulations for the four electric aircraft and a qualitative assessment of the isolated component of the energy networks. However, before we begin it is important that we establish grounds for performance these comparisons. Unless otherwise state, the x-axis depicting flight time is normalized by the total time for each vehicle whereby $\hat{t} = t/t_{EoF}$. Additionally the abbreviations SR, TW and MR refer to the stopped-rotor, tandem tilt-wing and multi-rotor EVTOL concepts respectively. This normalization allowed the compression of information from the four aircraft onto a reduced number of figures. We begin by recognizing the slight differences in flight profile as shown in Figure 5.5, particularly in the exploded window highlighting the departure of each aircraft. This is expected as they correspond to the dissimilar maneuvers given in Table 5.3. By scrupulously modeling these departure and approach maneuvers, one can obtain more a deeper understanding of the behaviour of the aircraft during the first few minutes of flight. The subsequent stages of climb vary from aircraft to aircraft. For instance, the multi-rotor uses its lift-rotors mounted at 90° to climb while the tilt-wing relies upon a combination of wing incidence angle and oriented lift-rotors to gain altitude. Because the

Table 5.5: Flight profile parameters and engine settings for electric aircraft

Flight Segment	Initial Altitude (ft)	Final Altitude (ft)	Initial Speed (mph)	Final Speed (mph)	Climb Rate (ft/min)	Rotor Orientation Angle (deg.)	Blade Pitch Command (deg.)
ECTOL Aircraft							
TO	0	0	7	77	0	0	0
DER	0	50	77	84	600	0	0
ICA	50	500	84	92	600	0	0
CL	500	2500	92	175	500	0	0
CR	2500	2500	175	175	0	0	0
D	2500	1000	175	100	-300	0	0
DL	1000	1000	100	92	0	0	0
BL	1000	500	92	84	-300	0	0
FA	500	0	84	77	-300	0	0
L	500	0	77	7	-300	0	0
Stopped-rotor EVTOL Aircraft							
VC	0	40	0	5.6	500	0, 90	0, 0
VT	40	40	5.6	87	0	0, 90	0, 0
CT	40	100	87	95	*	0, 90	0, 0
CL No.1	100	300	95	160	500	0, 90	0, 0
CL No.2	300	2500	160	175	500	0, 90	0, 0
CR	2500	2500	175	175	0	0, 90	0, 0
D	2500	300	175	117	-300	0, 90	2, 0
AT	300	40	117	103	*	0, 90	0, 0
DT	40	40	103	3.4	0	0, 90	0, 0
VD	40	0	3.4	0	-300	0, 90	0, 0
Tandem tilt-rotor EVTOL Aircraft							
VC	0	40	0	3.4	300	90	-5
VT No.1	40	40	3.4	40	0	45	3
VT No.2	40	40	40	80	0	45	3
CT No.1	40	100	80	100	500	15	5
CT No.2	100	500	100	125	0	15	20
CL	200	2500	125	175	500	0	16
CR	2500	2500	175	175	0	0	16
D	2500	200	175	100	-300	0	16
AT	200	140	100	55	-300	15	15
DT	140	140	55	3.4	*	25	5
VD	140	100	3.4	0	-300	90	-5
Multi-rotor EVTOL Aircraft							
VC	100	140	0	3.4	300	90	0
VT	140	140	3.4	35	0	90	3
CL No.1			35	75	500	90	2
CL No.1	140	2500	35	75	500	90	2
CR	2500	2500	75	75	0	90	5
D	2500	100	75	35	-200	90	5
DT	140	140	35	3.4	*	90	3
VD	140	100	3.4	0	-300	90	0

rotors for these two aircraft were designed for a larger airspeed range than the rotors of the stopped-rotor, the ascent stages can occur sooner. This is depicted on plot by steeper local gradients of the red and green lines compared to the stopped-rotor's in blue on the plot.

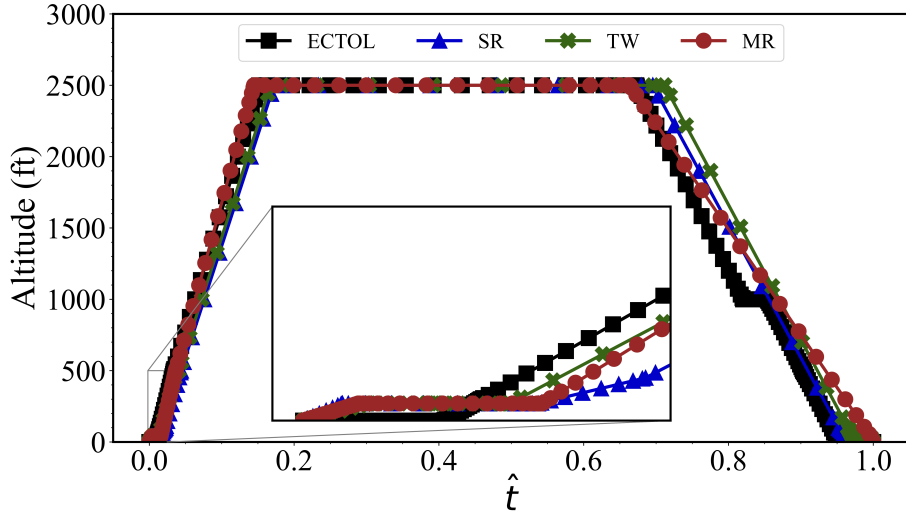
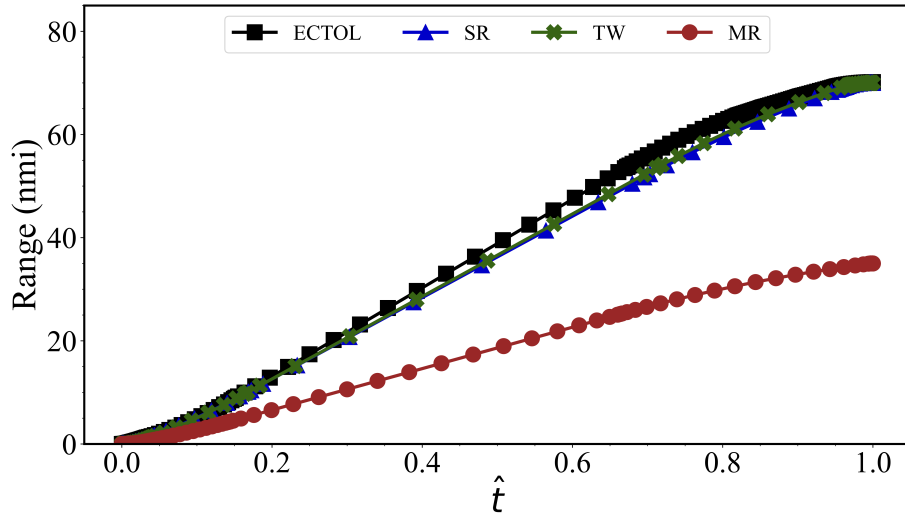


Figure 5.5: Altitude profiles of electric aircraft for a single-leg mission.

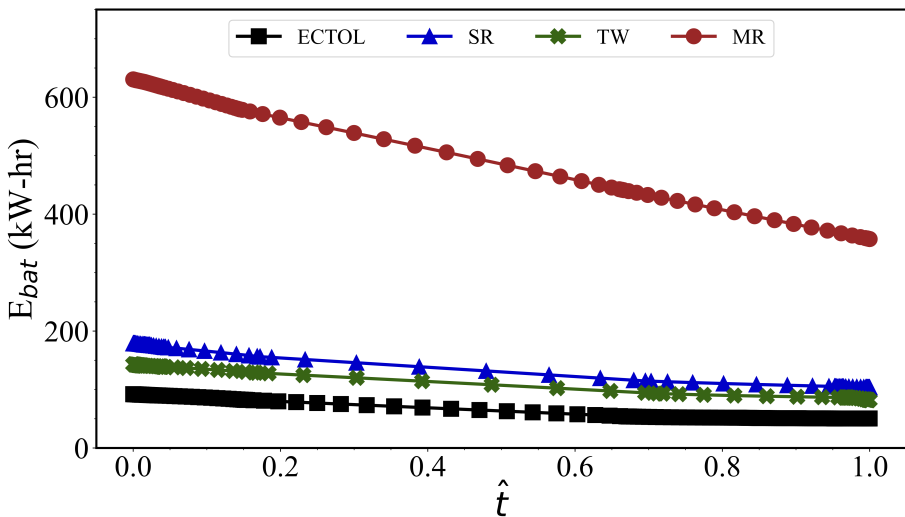
5.4.1 Battery Pack Performance System

Aircraft range, battery energy and state of charge shown in Figure 5.6 collectively conveys a common oversight of aircraft designers developing RUAM concepts, the choice of vehicle configuration plays a significant role in the ability of an aircraft to successfully complete a mission of a given range. Recalling from Chapter 1, the original goal of this research was to compare four aircraft operating comparable flight profiles. By inspection of Figure 5.6(a), it is clearly evident that this was not achieved. Only three of the four aircraft, the ECTOL, the stopped-rotor and tilt-wing successfully closed the specified mission. During preliminary sizing it was discovered that given the using current state of the art batteries, there was no feasible multi-rotor design capable of reaching the target range of 70 nmi. This observation would not have been possible had batteries with exaggerated performance been used. The multi-rotor fell significantly short of this range, reaching a maximum distance of approximately 37 nmi. Even with a battery pack roughly three times the size of the other two EVTOL aircraft, the aircraft was incapable of performing the 70 nmi mission with

net-positive energy. This disparity in the range can be attributed to the large power requirements wingless aircraft have to sustain to perform altitude-changing maneuvers such as vertical climb as well as forward flight. With the weight penalty caused by adding batteries in series (increasing I) or in parallel (increasing V), it can be gathered that simply increasing the size of the battery pack does not guarantee a feasible mission. What transpires is an iterative, diverging sizing loop - a larger



(a) Mission range.



(b) Pack energy.

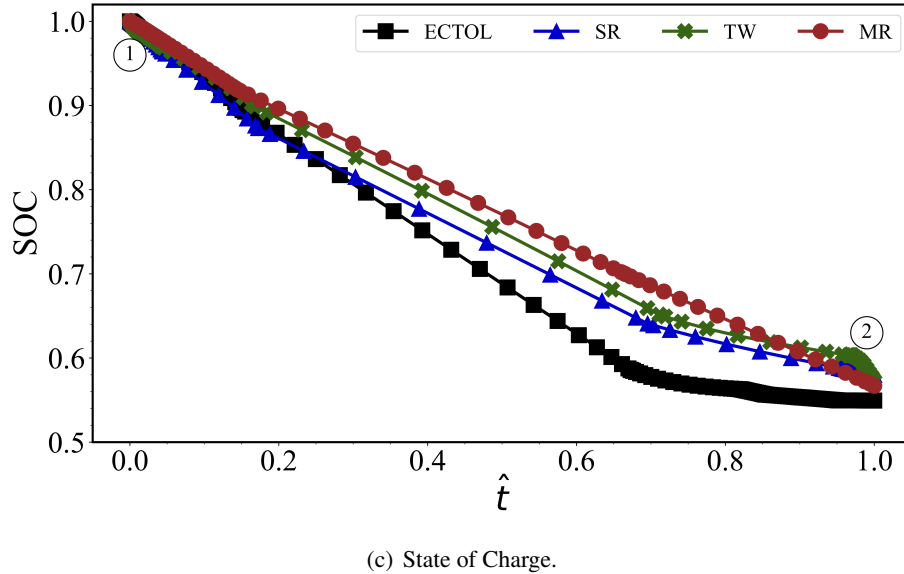


Figure 5.6: Vehicle range and battery pack discharge characteristics on board electric aircraft for a single-leg mission.

battery pack capable of supplying more energy and power will increase the weight of the aircraft, which in turn increases energy and power requirements of the propulsion network.

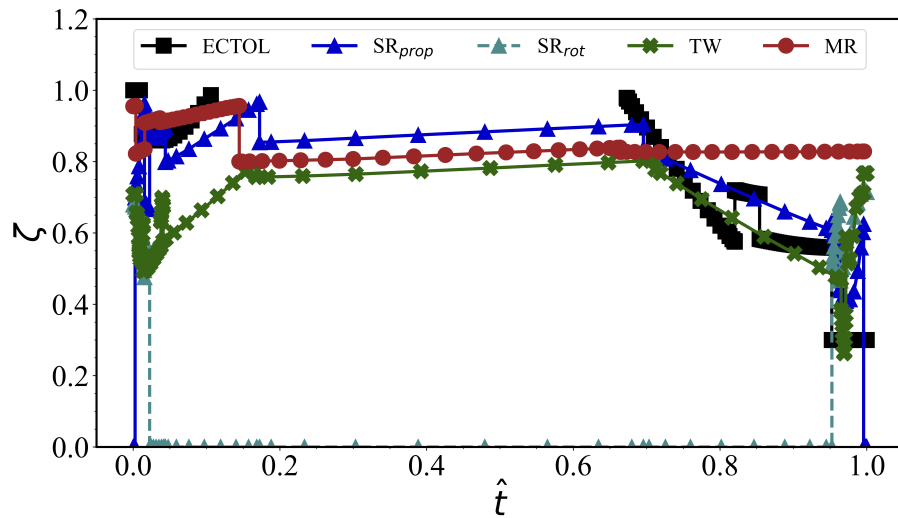
Figure 5.6(b) provides a clearer interpretation of the size of the battery pack. The ECTOL aircraft has a significantly smaller pack than the EVTOL aircraft, with stopped-rotor's battery being 179 kW-hr, the tilt-wing being 249 kW-hr, and the multi-rotor 631 kW-hr. This large battery pack of the multi-rotor is roughly 65% of TOGW, suggesting that battery module placement around the airframe will be a significant issue. The associated SOC curves describing the discharge as a function of time are shown in Figure 5.6(c). Here we draw the reader's attention to two local areas denoted ① and ②. They denote the beginning ($\hat{t} \approx 0.05$) and the final descent ($\hat{t} \approx 1$) respectively. The changes in gradient in these regions highlight greater power draw during vertical flight and climb segments. High power loading of the multi-rotor through the flight compared to the stopped-rotor and tilt-wing aircraft result in a pronounced drop in SOC. Locating where these drops occur in the discharge curve of a cell is crucial to understanding how system behavior at specific points can prompt irreversible electrochemical phase changes occurring within the electrodes battery cell during cycling.

Next, we correlate battery performance to other powertrain components such as lift-rotors, propellers and motors. It has already been established that the vertical climb and transition segments consume more power than the cruise and descent segments of flight. The throttles in Figures 5.7(a) offer insight into the non-linear behavior in power consumption throughout the mission as SOC falls. This phenomenon can be more explicitly shown through C-rate in Figure 5.7(b). Here, C-rate is defined here as the rate at which the cell's energy is being discharged relative to the remaining capacity within the cell. As the energy in the battery pack falls and SOC decreases, there is an associated voltage drop. This voltage deficit leads to the system drawing higher current loads to meet the power requirements of motors and on-board avionics, even in a constant-airspeed-constant-altitude segment such as cruise. Accordingly, we observe the increase in C-rate by as much as 160% of what is experienced in the initial climb stages of flight. From an aircraft certification perspective, understanding such behavior of the battery is necessary for battery management system design to ensure safe operation during repeated use.

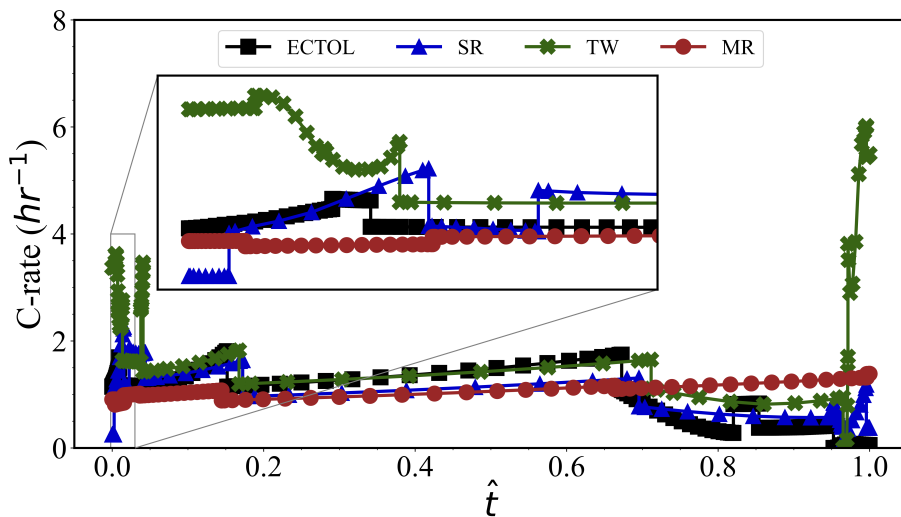
The use of a medium-fidelity battery model makes the determination of the cell temperature with the module becomes possible. Shown in Figure 5.7(c) are the variations of cell temperature predicted for each aircraft throughout a single leg of the mission. As expected, the segments characterized by high C-rates shown in the previous figure contribute more to the increase of temperature across all battery packs. In the case of the ECTOL aircraft, these particular high-power demanding segments are the initial climbing stages. What is interesting to note that the landing segments of this aircraft do not have a significant influence of cell temperature as the aircraft is performing decelerating descent maneuvers. This runs contrary to all the EVTOL aircraft whose battery packs are subjected to high power draw at both the beginning and end of the flight profile. The thermal responses of the cells also provides engineers, particularly those involved with BMS thermal management and idea of where additional attention must be placed to mitigate high loads. Examining the cell of the tilt-wing for instance, it can be noted that the rapid increase in temperature near the end of the flight is a major cause of concern. In the event of a touch-and-go scenario where the vehicle has to reroute to another landing site, the subsequent climbing segments may cause the battery to overheat to a point where a catastrophic failure becomes imminent.

5.4.2 Rotor Performance

Continuing the discussion of the energy network, we now turn our attention to the propulsion architecture and the ability of the mounted rotors to deliver the required thrust. Across all quantities reported below, it can be seen that the mission solver was able to capture the wide variation of loads with little convergence issues, suggesting that lifting surfaces and powertrain components of



(a) Rotor engine throttle.



(b) Battery C-rate.

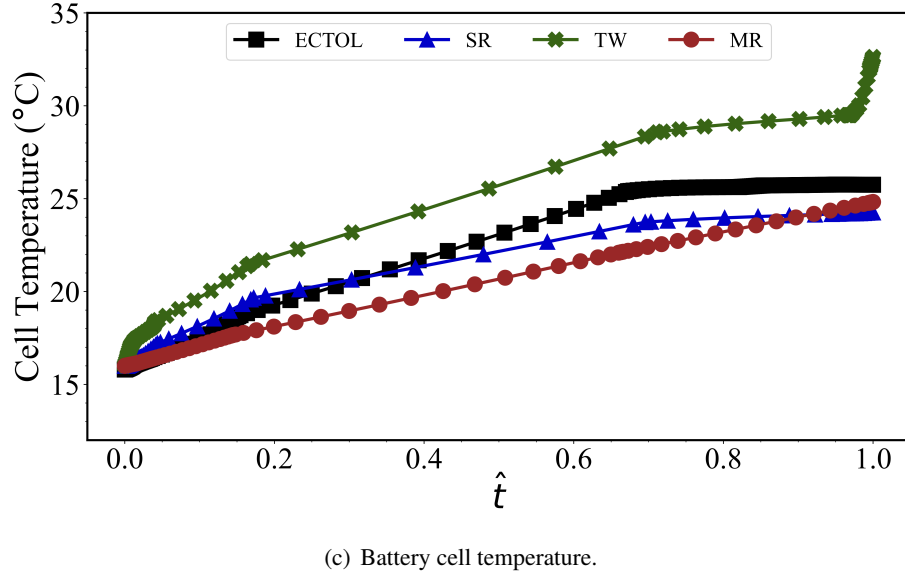
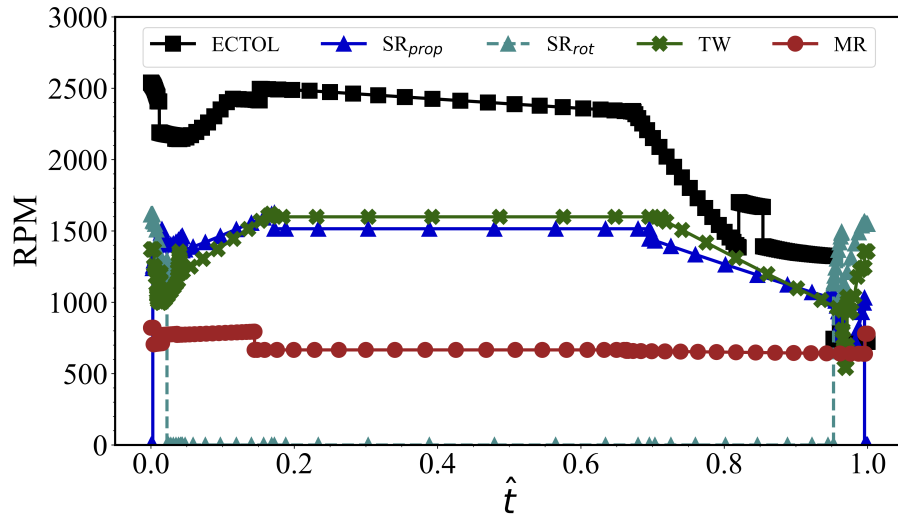


Figure 5.7: Battery cell characteristics on board electric aircraft for a single-leg mission.

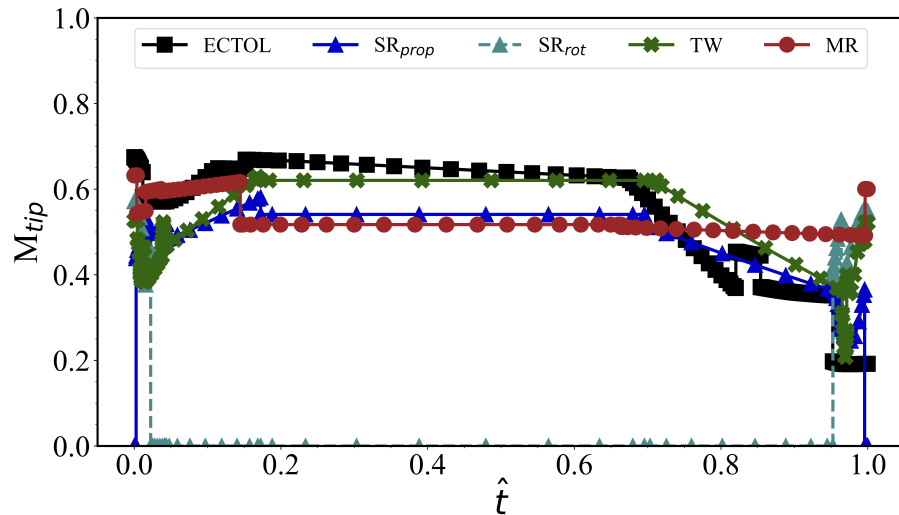
these baseline aircraft were appropriately sized. Figures 5.8(a) and 5.8(b) portraying rotor RPM and blade tip Mach number permit the identification of specific regions of the flight envelope where undesirable performance warrant further investigation and subsequent improvement to effect desired performance characteristics. One example of such modifications is varying blade pitch as airspeed changes to reduce power drawn from the battery, particularly near the end of cycle life. For the stopped-rotor configuration, both the lift-rotors (in teal) and propellers (in blue) are provided. Additionally for this aircraft, the simultaneous throttling down of the lift-rotors and throttling up of the propeller from zero to full power that was anticipated is observed as the aircraft transitions from vertical flight to a forward climb. This demonstrates the robustness of the mission solver to balance the forces at low air speeds using the rotors situated around the vehicle. Figures 5.8(c) and 5.8(d) depict how much the resultant rotor thrust and torque loads vary during transition maneuvers compared to more conventional segments such as climb, cruise and descent. Through capturing performance in off-design points of the flight profile, these figures highlight the importance of component sizing.

5.4.3 Aerodynamics and Flight Mechanics

The predicted flying dynamics of each configuration solidifies some of the observations that separate groups of vehicle designers, from government to industry, have started to witness during the preliminary prototype flight tests. Covered in this section is an in depth discussion on vehicle aerodynamics and the associated significance for the exploration of future intra-city passenger carrying



(a) Rotor RPM.



(b) Rotor tip Mach number.

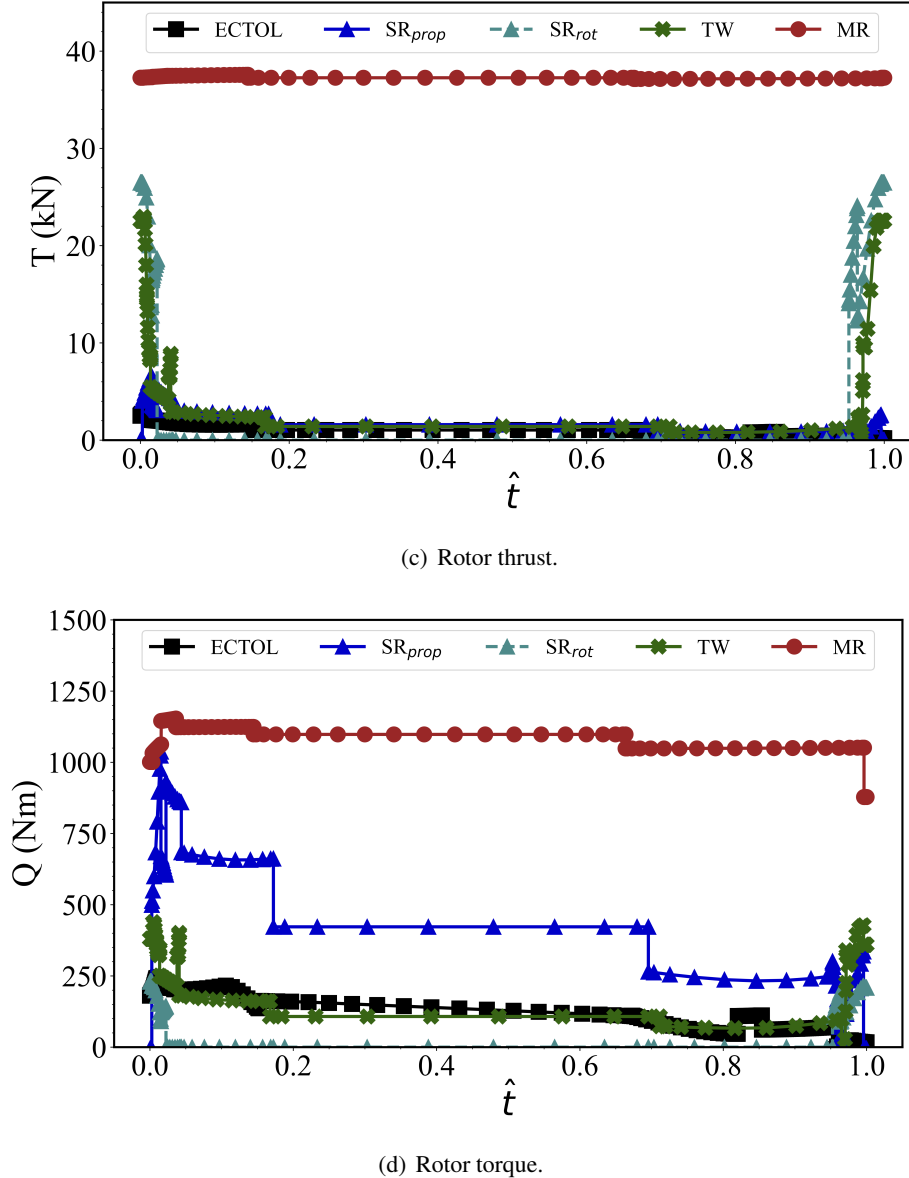


Figure 5.8: Rotor performance of electric aircraft for a single-leg mission.

aircraft. The orientation of passengers within each vehicle can be computed from Figure 5.9(a) of angle of attack (AoA) profiles together with the orientation of the vehicle relative to the wind frame. This is the same as the stability frame in this study. First, examining the conventional tube and wing aircraft, it can be seen that the ECTOL aircrafts' AoA profile closely agrees with flight data of ICE

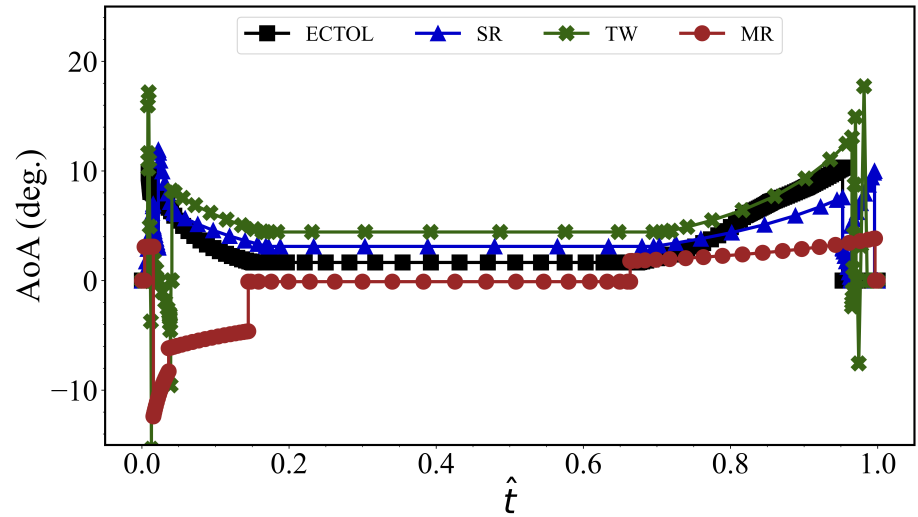
general aviation aircraft of equivalent size. High AoA during the climb and descent states of flight to generate more lift and a cruise AoA around 3° corroborate the computational approaches used in this study.

The more eccentric flight profiles of the three EVTOL aircraft offer more interesting perspectives on the maneuvers performed. They underscore the unbiased and unconstrained nature of the mission solver when computing the state variables that satisfy the conservation equations. The multi-rotor and tilt-wing configurations have similar accelerating phases of flight where the aircraft are transitioning out of vertical climbs to a low forward airspeed. During this phase, a downward pitching rotation of these two aircraft was observed as the mission solver orients the lift-rotors in the direction of the positive x-axis to generate forward thrust. As these two aircraft gain air speed however, their flight dynamics diverge. For the tilt-wing aircraft, the incidence angles of the wings reduces to generate more forward thrust. On the other hand, similar to a helicopter in forward flight, the multi-rotor aircraft remains to pitched downward to accelerate. This results in negative lift from the fuselage surfaces modeled in the VLM. It must be noted that the AoAs of the EVTOL aircraft during the hover/vertical climb segments were omitted as they alternate between $+/- 90^\circ$ depending on the motion of the vehicle. This is solely put down to how the AoA variable is computed in SUAVE using body angle and the velocity vector.

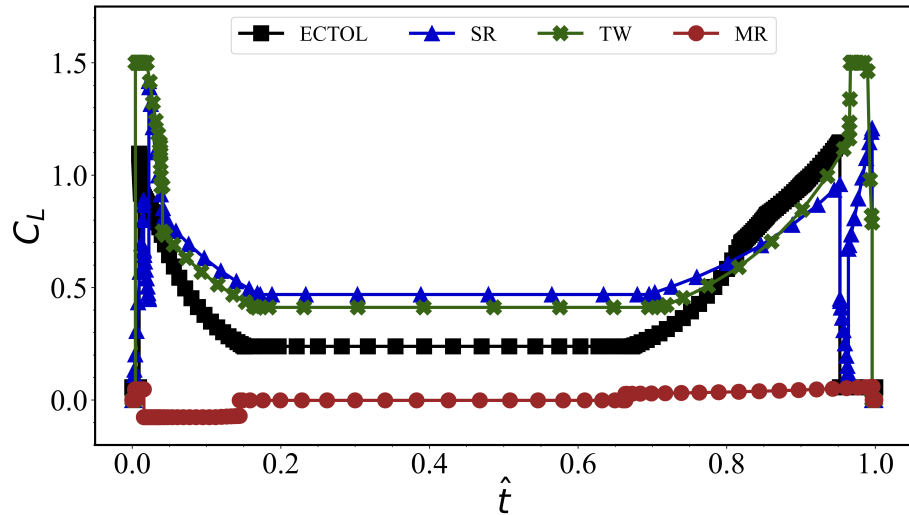
In the case of the stopped-rotor EVTOL aircraft in transition, the aircraft tends to pitch up at high AoAs as the mission solver seeks to orient the vehicle in such a manner to generate lift using both the rotors together with the main wing. At this stage, lift-rotors that are used to produce the initial vertical lift begin to power down while the rear propellers begin to spin to generate forward thrust. As this aircraft gains airspeed, the AoA reduces to cruise values around 3.4° . The observed behavior of the simulated stopped-rotor and tilt-wing mirror the flight dynamics observed of their respective flight demonstrators built by Wisk [125] and Acubed [126], further validating the preliminary findings presented here. In climb and cruise segments, these two vehicles take to more fixed-wing conventional performance, with recorded L/D values around 15.6 for the stopped-rotor and 15.9 for the tilt-wing as depicted in Figure 5.9(d).

5.4.4 Noise Footprint

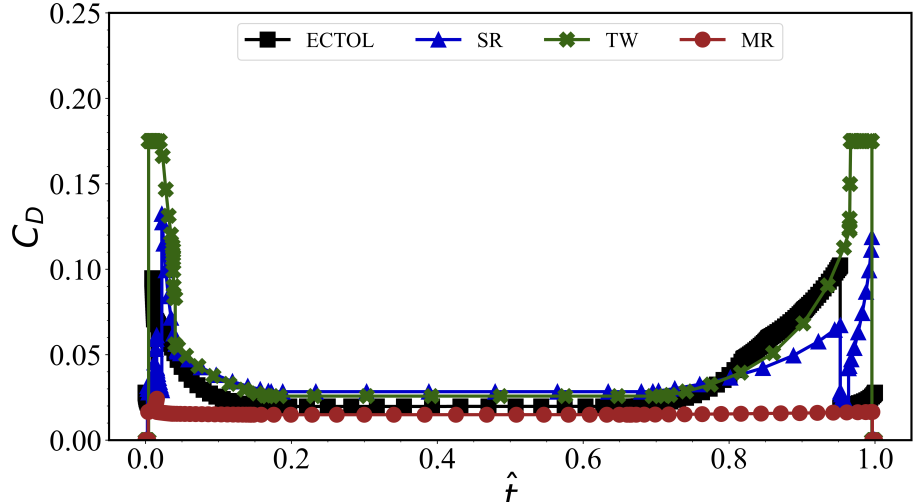
Apart from energy network performance, reduction of the noise footprint of RUAM service providers stands in the way of public acceptability of this mode of transportation in cities and residential areas across the world. Vehicle noise will not only dictate approach and departure paths, but the frequency of flight operations. It is therefore critical that a framework capable of providing



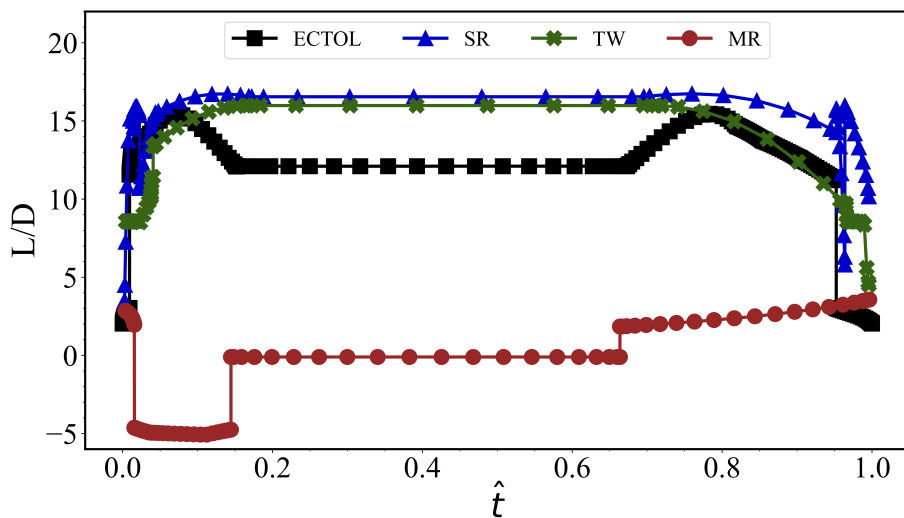
(a) Flight AoA.



(b) Lift coefficient.



(c) Drag coefficient.



(d) Lift-to-drag ratio.

Figure 5.9: Aerodynamic characteristics of electric aircraft for a single-leg mission.

fast but reliable estimates of noise footprint be developed to accelerate early conceptual design. We answer this need in this section with the presentation of vehicle noise measured from ground level. Figure 5.11 depicts the SPL_{Amax} recorded directly beneath the aircraft, i.e. $y = 0 \forall \hat{t}$. Below, attention is placed on the portion of the flight profile where the human annoyance is expected to

be a significant issue - near the vertiport. Correspondingly, the flight profiles of the four aircraft under examination model their respective approach, landing, takeoff and departure segments in that order. All flight profiles start at 500 ft and follow the segment kinematics outlined in Table 5.3 for arrival and landing. Without intermission, the takeoff and climb segments are subsequent modelled to simulate a "touch-and-go" scenario. An illustration of this maneuver is illustrated in Figure ?? where the tilt-wing model shown flies over a regular array of ground microphones where the sound pressure level is evaluated. To reiterate, both the dominant harmonic (periodic) component and the broadband components of the acoustic spectrum are encompassed in the prediction of the total radiated noise of the aircraft here. Airframe noise and unsteady-wake interaction noise are neglected in the computational analysis. As the aircraft gains altitude, the distance between the observer locations and the aircraft increases and so the noise level drops significantly.

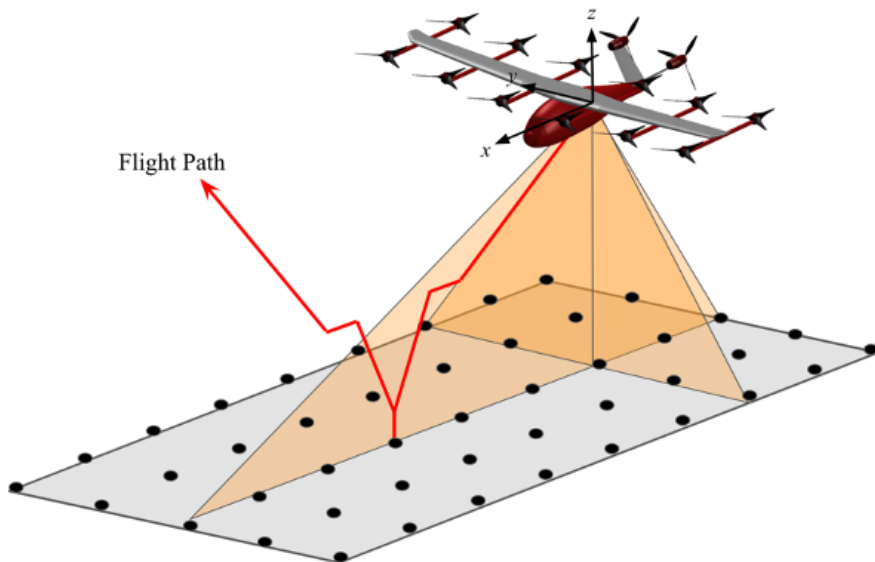


Figure 5.10: Stopped-rotor aircraft touch and go scenario.

Next, we examine the noise contour plots provided in Figure 5.12. The simulations to amass these results were done on a single desktop machine with 8 processors and 16 GM of RAM and the run-times are provided in Table 5.6 provide the reader with a sense of how expensive these such computations are. It must be noted here that attempts made to run simulations on servers within the Aerospace Design Lab proved to be futile as the nature of the problem required large amounts

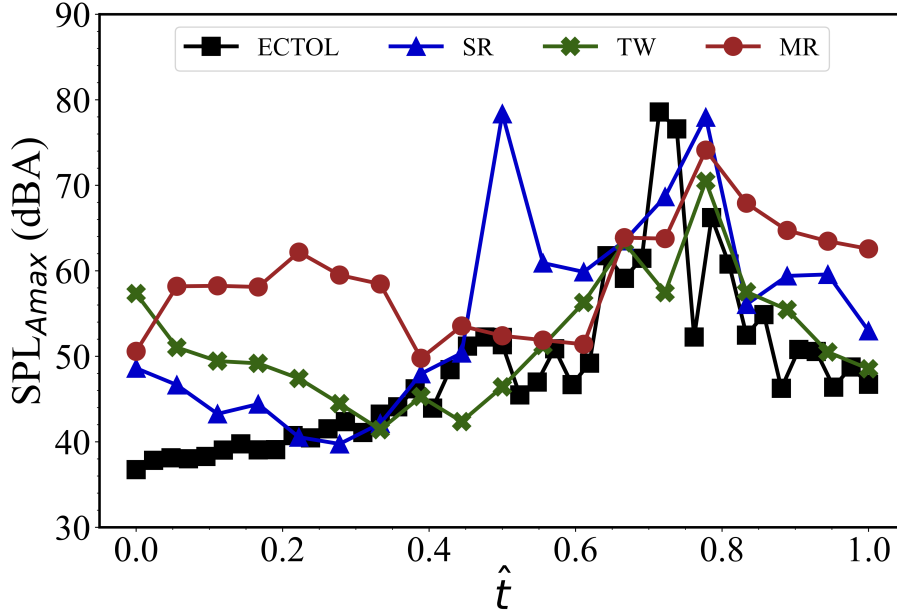


Figure 5.11: SPL_{Amax} of electric aircraft for a single-leg mission at microphone location $y = 0 \forall \hat{t}$.

of memory on each node. This runs contrary to other commonly parallelizable problems such as CFD and FEA where the memory required for computation is small, allowing for the use of several, low-memory nodes.

Table 5.6: Simulation settings and computation times used in electric aircraft noise footprint study

	ECTOL Aircraft	Stopped-rotor	Tilt-rotor	Multi-rotor
Control Points Per Flight Segment	22	10	10	20
Microphone Array (longitudinal \times transverse)	44×10	20×10	20×10	20×10
Number of Microphones	440	200	200	200
Simulation Time (hrs)	2.0	4.4	2.8	4.6

The contour plots shown below provide an indication of how the radiated noise changes with vehicle orientation and flight maneuver and further explicate the trends in SPL_{Amax} observed in Figure 5.11. Starting with Figure 5.12(a) it can be observed that as the aircraft descents the SPL_{Amax} to a local maximum around $x_{fp} = 1.75$ nmi when a value around 60 dBA is recorded. The subsequent throttling down and deceleration of this aircraft as it moves along the runway can be seen by

the reduction in SPL_{Amax} between the $x_{fp} = 2$ and 2.5 nmi mark. During ground acceleration, SPL_{Amax} once again increases as the RPM and blade loading on the propeller increases. This is illustrated on the contour plot in the region $x_{fp} = 2.5$ to 2.8 nmi, at which point the vehicle climbs and the recorded level-ground noise correspondingly decreases. The width of contour bands from the takeoff decrease in width as the aircraft ascends to 500 ft. In contrast, the EVTOL aircraft exhibit higher noise levels near the ground irrespective of whether the three aircraft are landing or taking off. This is due to the heavily loaded rotor blades that these configurations experience during the transition and hover phases of flight. Starting with the examination of the stopped-rotor aircraft we see that the recorded level ground noise is affected by both directivity and distance. Starting at 500 ft, the noise level directly below the aircraft first reduces as the rear propeller engines throttle down as the aircraft decelerates in the air. At the point where the lift-rotors throttle up around $x_{fp} = 2.5$ nmi, we see a sharp increase in noise. What is interesting to notice is that during landing near $x_{fp} = 4$ nmi, the recorded noise is slightly lower (≈ 75 dbA) than when the vehicle is transitioning and all rotors are spinning (≈ 78 dbA). This observation can be attributed to the higher lobes of radiated rotor noise being directed away from the ground in vertical flight. If we recall from Figure 3.6 in Chapter 3, directly in front and behind the rotor plane, the predicted noise of the rotor is lower than experimental values, suggesting that there may be an under-prediction of total vehicle noise in this particular segment of the flight.

Though the tilt-wing aircraft noise contour plot follow a similar trend for radiated noise, lower SPL_{Amax} recording near the landing and vertical climb are predicted. Despite the disc loading at hover being slightly greater than the stopped-rotor, this RPM of rotor blades is about around 16 % less, resulting in values around 65 dbA. Last but not least, in examining the multi-rotor aircraft it can be deduced that despite high noise recordings existing directly below the aircraft, in part due to the high tip Mach number of the blades the noise depreciates quite rapidly in the lateral direction. One hypothesis for this phenomenon is the fact that the large lobes of radiated noise are more in line with the aircraft at the same altitude due to the positioning of the blades on the airframe. This suggests that though this particular configuration has the advantage of being relatively quiet for distant individuals on the ground, the noise radiated in an urban canyon with elevated indicates such as in a building will be significantly higher and must be assessed further. Because this aircraft

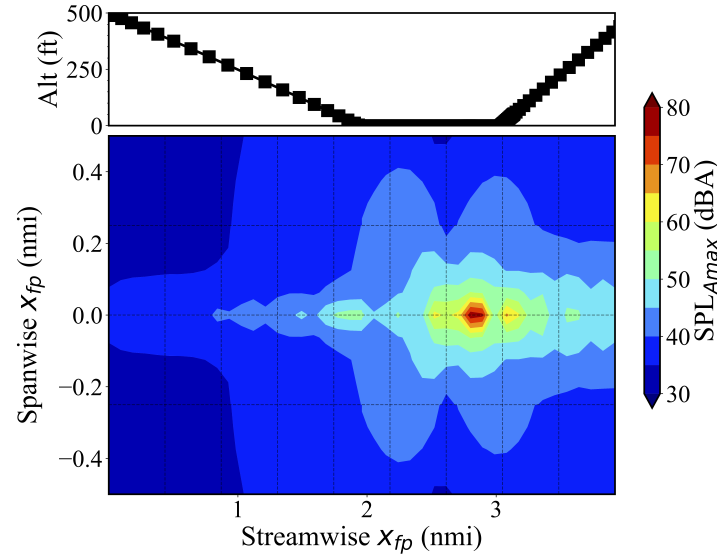
does not undergo any transition that seeks a significant change in blade axis, the maximum recorded sound pressure level occurs at the precise location where the vehicle lands and takes off at $x_{fp} = 1.8$ nmi.

That being said, the noise predicted near all aircraft on the ground fall above the milestone of 60-65 dBA proposed by lawmakers, making them, in their present state, unfit for RUAM service. As urban airspaces begin to open for business and EVTOL services start to launch hundreds of vehicles, noise exposure from low-altitude vehicles is expected to create a lower threshold for annoyance. Premature deployment could have a devastating impact on the future by resulting in local noise ordinances that restrict operations. To realize this form of transportation in large cities such as New York, San Francisco and Los Angeles, aircraft designers and engineers will need to reduce noise signatures or at least shift the dominant frequencies of the radiated acoustic spectrum to a region of lesser annoyance to the human ear. This can be achieved through phasing or rotor phasing, blade loading alteration through topology optimization and acoustic shield using cowlings. All of them however do come at the expense of propulsive efficiency. In the following chapter, one of these noise reduction strategies, namely blade optimization is examined.

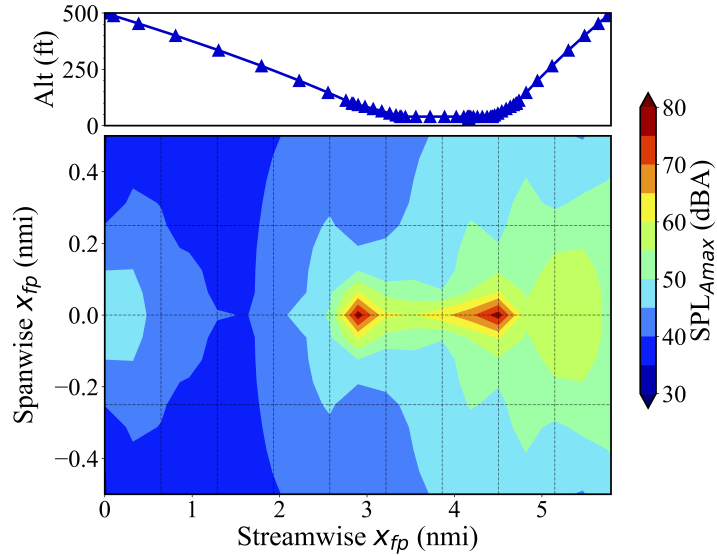
5.5 Assessment of Mission Simulations: Extended Operation Comparisons

The previous section summarized only a fraction of the results from the analyses to assess the performance of the electric aircraft under consideration in this work. In it, a concerted effort was made to stress the significance of some of the findings and connect predictions made with stories of many of the private companies in the race of commercialization leading the charge to develop non-conventional aircraft today. To remind the reader, these results are of a single leg of the missions outlined in Section 5.3. Now in this section, we shift our attention to examine prolonged flight operations. These missions comprise of identical flights over a realistic time frame whereby the time of day and year are factored into the flight simulations. Table 5.7 documents nine ranges that the aircraft are simulated under for each vehicle. The climb and descent segments detailed in Table 5.3 remain fixed while only the cruise segment is allowed to change to meet the specific

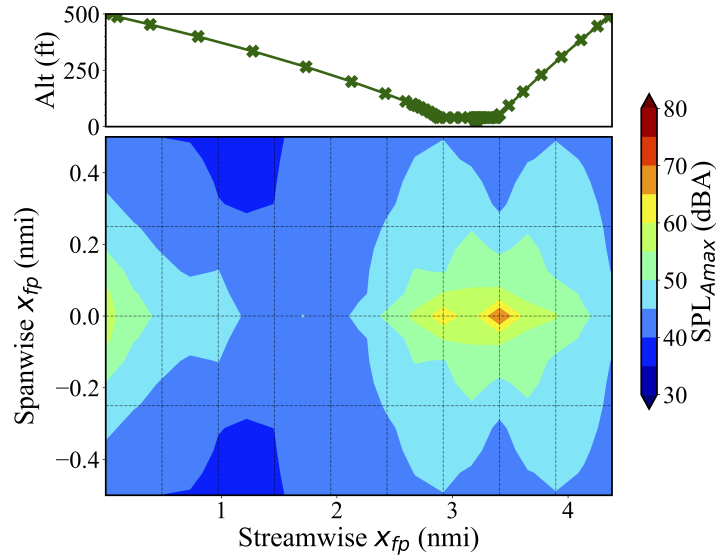
target range. As previously alluded to, the range of the multi-rotor fall well below that of the other three aircraft, underscoring this vehicle's inability to perform long-range missions. This is due to



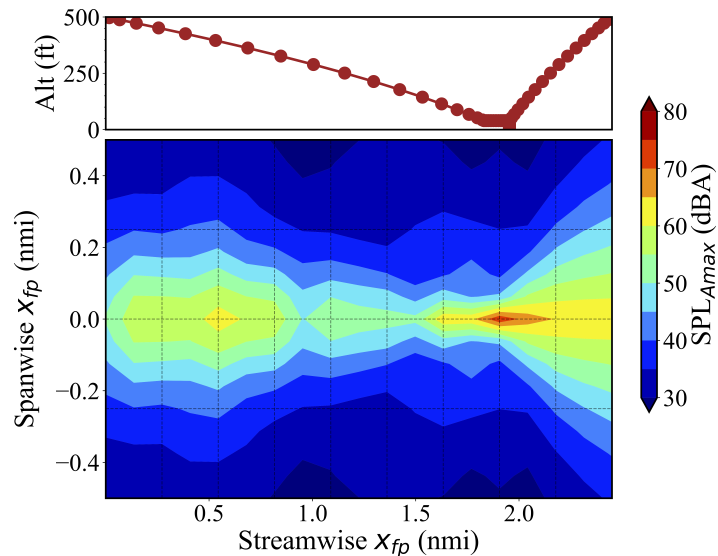
(a) ECTOL aircraft noise footprint for touch-and-go scenario.



(b) Stopped-rotor aircraft noise footprint for touch-and-go scenario.



(c) Tandem tilt-wing aircraft noise footprint for touch-and-go scenario.



(d) Multi-rotor aircraft noise footprint for touch-and-go scenario.

Figure 5.12: SPL_{Amax} footprint contours of touch-and-go scenarios for electric aircraft.

the large amounts of power required by this configuration to perform cruises without the benefit of wings that enable efficient long-range flight. Eight daily flights were simulated each day to reflect the continuous services that UAM businesses are expected to operate. Battery recharging at 1C from the end-of-flight SOC to 100% SOC was also simulated after each flight. This of course does not necessarily mean that the battery reaches the same capacity as its pristine state since the cell ages with time. Though the aforementioned rate of battery charging is on the lower end of the spectrum for EVs, a slow charging protocol enables us, to some degree, isolate this factor's impact of battery capacity fade and internal resistance growth among other things.

Table 5.7: Simulated ranges of the electric aircraft.

Aircraft	Range (nmi)								
	Case 1	Case 2	Case 3	Case 4	Case 5	Case 6	Case 7	Case 8	Case 9
Twin-engine ECTOL	60	65	70	75	80	85	90	95	100
Stopped-rotor EVTOL	60	65	70	75	80	85	90	95	100
Tilt-wing EVTOL	60	65	70	75	80	85	90	95	100
Multi-rotor EVTOL	20	22.5	25	27.5	30	32.5	35	37.5	40

Simulating extended periods of time presents two unique challenges: representing large amounts of information and determining how best to weigh the various aspects of vehicle performance. On top of this, with the incorporation of temperature as a function of both altitude and time of year, some observations exhibit strong bi-variance. We therefore rely on TAPOOL diagrams as a means of describing the behavior of an electric aircraft's battery pack under realistic flight and environmental conditions. This differs from traditional approaches of assessing battery-powered aircraft in two ways: first, time-dependency is introduced into the efficiency criteria of stored-energy systems; and secondly, the full flight profile which includes the climb and descent stages of a mission is used rather than the constant altitude and constant airspeed assumptions in the computation of range and endurance.

The performance of the battery in any given flight segment is also directly affected by its history, or rather the electrical load that pack is subjected to during the previous segment. This meant that simulations had to be performed in sequence and computational operations could not be parallelized. Depending on the aircraft configuration, simulations therefore took between 2-5 days on a single node on the in-house 8-node cluster of the Aerospace Design Lab at Stanford University.

Hence, the data presented in the study was amassed over a period of one month. This however is still significantly shorter than running capacity tests on cells within a laboratory setting on a programmable cycler. By and large, leveraging computer simulations has the potential to 1) fill the gaps of experimental data; 2) accelerate testing by addressing the information entropy problem, that is, determining the least amount of information required to fully characterize cell aging; and 3) predict battery end-of-life. The following subsections discuss the TAPOOL diagrams for battery cell capacity, maximum cell temperature and maximum instantaneous C-rate. These three variables were deemed to be the most significant given their implications on both safety and performance at the system level. In the figures below, simulations are terminated when the SOC at the end of a flight first reaches a lower threshold of 20%, signifying the end of useful life. The decision to use this cut-off value over other thresholds of 15% and even 10% suggested by German et al. [127] was due to the fact that as the cell degrades, the inflection point where there is a precipitous drop in voltage becomes increasingly difficult to predict in practice. The higher cut-off SOC therefore ensures that the simulated operations will be guaranteed. Infeasible regions of flight missions are hashed in black and white on the figures.

5.5.1 Battery Capacity

Arguably the most important metric in cell SOH, capacity fade is a measure of the change in the cell's charge storing potential relative to its pristine condition at the beginning of use. This degradation can be credited to several internal mechanisms including the deterioration of the rock salt structure of the cathode, exfoliation of the graphite structure at the anode resulting in a weakening of bonding potential, and the growth of the SEI layer that consumes active material. Figure 5.13 depicts the behavior of capacity fade as a function of range and number of days in operation. As expected, the general trend across configurations is that longer missions accelerate cell degradation and reduce the operational lifetime. In other words, the number of days that a particular aircraft can fly a given route decreases with increasing cruise distance. For the flight schedules defined in the previous section, it was observed that battery life of achievable missions can drop by as much as 45% by the end of a calendar year depending on vehicle configuration, range and battery pack size. From a purely utilitarian standpoint, the ECTOL aircraft, with the highest operational periods

across all ranges, is the most energy-efficient option. This however does not factor in the footprint needed for takeoff by such a configuration, which poses a significant dilemma for operating in urban spaces. Taking a step back to assess the implications of these trends on vehicle choice, we see from a graphical analysis that the lifetime of operation of the ECTOL, stopped-rotor EVTOL, tilt-wing EVTOL and multi-rotor decreases by 11, 8, 9 and 23 days respectively for every additional nautical mile flown. These linearized approximations were computed by examining end-of-life states at the 90 and 70 nmi ranges for the first three vehicles and 37.5 and 30 nmi for the multi-rotor. It is important to note that these rates are not necessarily a comparison of energy consumption in the respective battery packs but rather the rate at which this energy depletes. These rates do however provide direction in constructing more appropriately size battery packs.

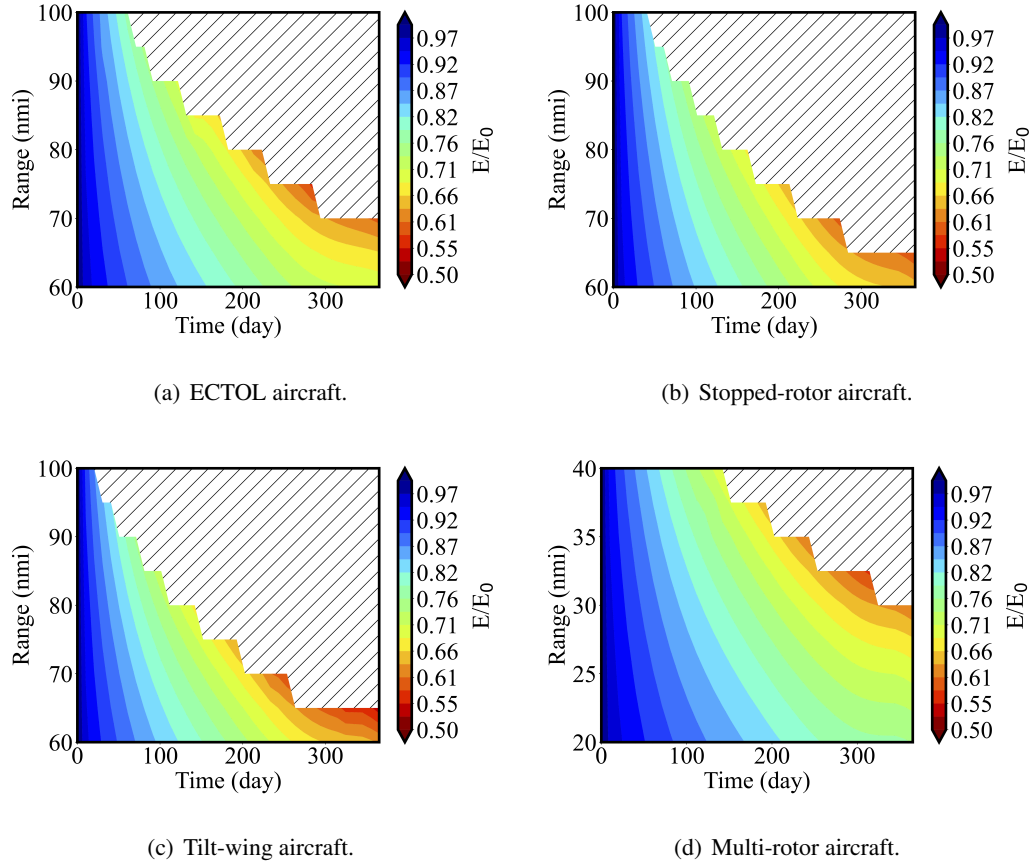


Figure 5.13: Battery cell capacity TAPOOL contours of electric aircraft.

These plots also lend key insights into what strategies air-shuttle and air-taxi services should adopt to maximize the potential of both brand-new and used aircraft. Taking San Francisco for example, we can infer from Figure 5.13(a) that a service using a new twin-engine ECTOL aircraft between Oakland International Airport (OAK) and Sacramento International Airport (SMF) will last around 200 days. As another example using Figure 5.13(d), we can arrive at a service period of 350 days for multi-rotor operating non-stop between Norman Y. Mineta San Jose International Airport (SJC) and either OAK or San Francisco International Airport (SFO), which are roughly the same distance apart. On the other hand, if we have a tilt-wing EVTOL that has been providing a 90-nmi regional service in the New-York Metropolitan Area between Philadelphia International Airport (PHL) and Lower Manhattan (LMX) for 100 days, it can be repurposed for flights between John F. Kennedy International Airport (JFK) and Long Island MacArthur Airport (ISP) to extend of service life by another 200 days before battery pack replacement is needed.

5.5.2 Maximum Instantaneous C-Rate

Shown in Figure 5.14 are the changes in current severity passing through a cell at any given instant in time. Before we elaborate on these trends, it is important to first remind readers of the terminology concerning C-rate used in this study. Continuing the discussion from Section 5.4, nominal C-rate can be viewed as the current through the battery divided by the current draw under which the battery would deliver its rated capacity in one hour. For example, a discharge of 2-C of a 1Ah cell indicates that the cell would be fully-discharged in 30 minutes. This rated capacity is typically provided by the manufacturer but can be experimentally determined in the lab [128]. Conversely in this study, we utilize instantaneous C-rate, defined as the rate at which a battery is being discharged relative to the cell's capacity at that current state in time. This was the preferred metric as it allows us to understand the differences between discharges of equivalent magnitude at opposite ends of the SOC range, that is, fully-charged and fully-discharged. Instantaneous C-rate conveys how severe discharges near the end-of-cycle are to battery health.

As the battery ages and the voltage, as a function of SOC, drops, more current is required to supply the same power to the powertrain. The maximum C-rate for the four aircraft therefore all increase with increasing range and length of operation. We can also deduce from Figure 5.14(c) that

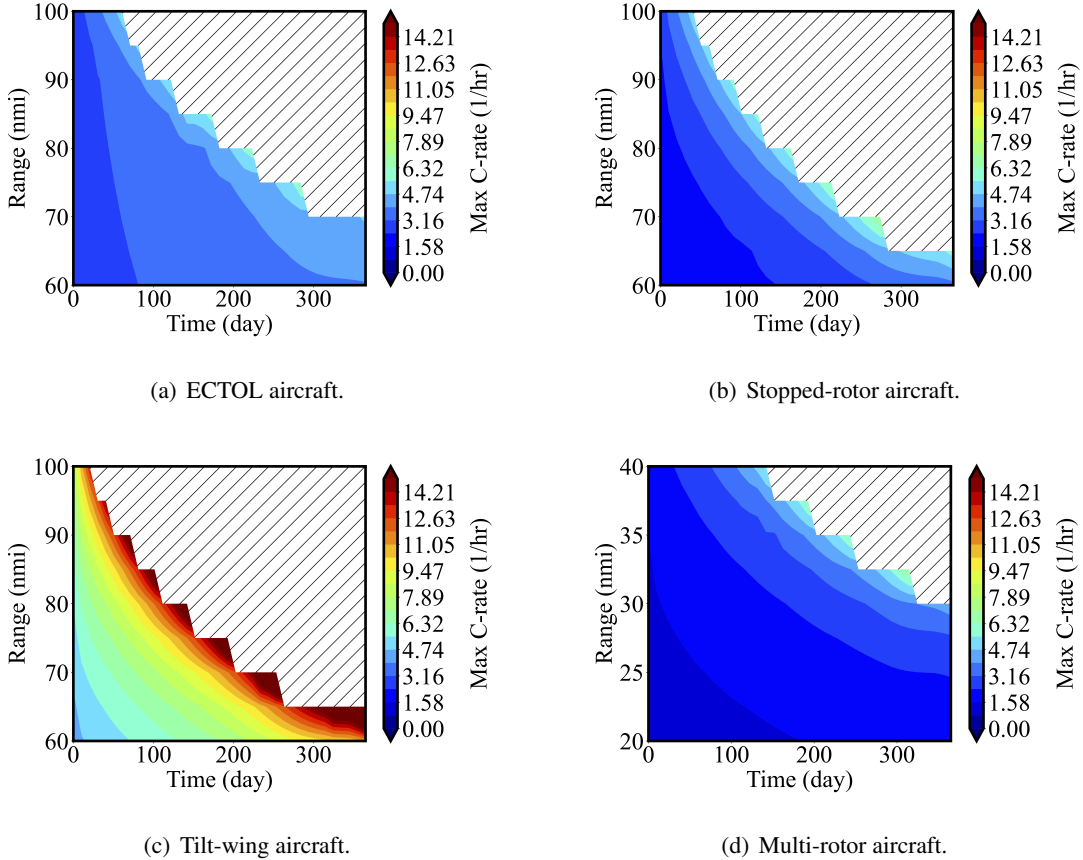


Figure 5.14: Maximum instantaneous C-rate TAPOOL contours of electric aircraft.

despite the battery pack of the tilt-wing EVTOL aircraft being sized to meet mission specifications at the beginning of service, the electrical layout (number of cells in series and parallel) was not copiously done, resulting in extremely high C-rates as time progresses. These trends could not have been observed in a single-flight analysis, further demonstrating the versatility of TAPOOL diagrams.

5.5.3 Maximum Cell Temperature

Accompanying the increase in ohmic resistance within the battery cell is the increase in temperature. Unlike the prior two quantities discussed above, the heat generated by the cells over the aircraft's operational lifetime exhibits strong bi-variance as its behavior is somewhat offset by the

ambient temperature which changes year-round. For example, if we examine a 65 nmi mission of the twin-engine ECTOL aircraft in Figure 5.15(a), we witness that during the months of August and September, the temperature within the battery module can reach 318 K or 45 °C. In longer-range missions, temperatures can even reach 324 K or 50 °C earlier in the year as a result of a rise in accumulated heat energy during cruise segments of the flight profile. This temperature increase is a direct result of the constant airflow of the cooling air in the simulations which governs heat rejection.

Generally speaking, all electrochemical cells have an optimum temperature range of operation, lithium-ion battery cells included. Operating within this window not only guarantees that the battery performs at its full potential, but prolongs the life of the cell. The temperature TAPOOL diagram

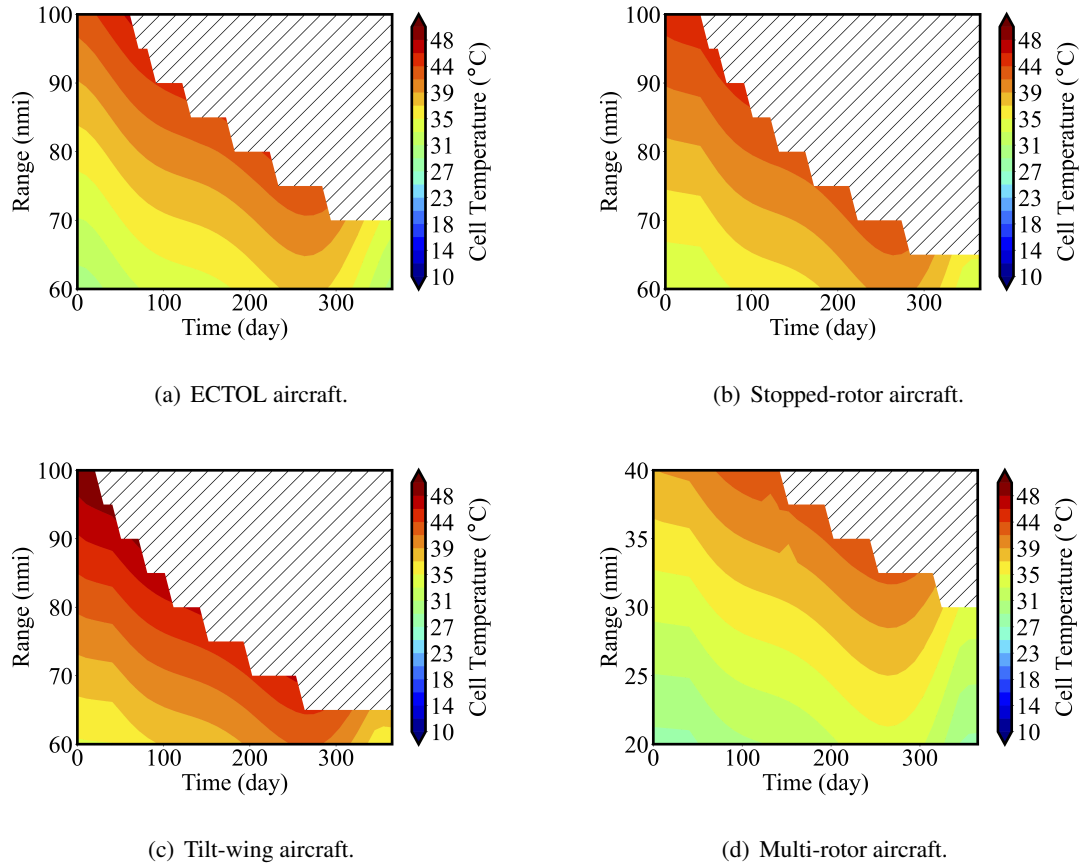


Figure 5.15: Maximum temperature TAPOOL contours of electric aircraft.

hence provides system designers with critical insights into the design of the thermal management system and the cell layout needed to achieve ideal operating conditions within the module.

5.5.4 Comparison with Traditional Electric Aircraft Performance Metrics

Early studies by Retana and Rodriguez-Cortes [129] and Lawrence and Mohseni [130] paved the way for the widely used formulations by Traub [131] for estimating range and endurance of battery-powered aircraft. These formulations start with the simple energy balance in Equation 5.6a below where the power required for steady, level flight is balanced with the speed and drag of the aircraft. As shown in Equation 5.6b, the drag force can be further deconstructed into its zero-lift component, which captures profile drag and skin friction, and the drag due to lift, corrected by a factor to account for aerodynamic phenomena such as viscous pressure drag and vortex drag. With suitable substitutions to express lift in terms of vehicle weight, lift coefficient and wing area, the required power can be expressed as the product of the drag force, D and airspeed, U .

$$P_{req} = D * U = \frac{1}{2}\rho U^2 S C_D * U, \quad (5.6a)$$

$$C_D = C_{D_0} + k C_D^2, \quad (5.6b)$$

$$P_{req} = \frac{1}{2}\rho U^2 S C_{D_0} + \frac{2W^2 k}{\rho U S}. \quad (5.6c)$$

In steady, continuous flight, this power is balanced by that supplied by the battery given by:

$$P_{bat} = V * i, \quad (5.7)$$

which, using modification of Peukert's equation in Equation 5.8 for the current of an electrochemical cell can be expressed as:

$$i^n = \frac{Rt}{t} \left(\frac{C}{Rt} \right)^n, \quad (5.8)$$

is given by:

$$P_{bat} = V * \frac{Rt}{t} \left(\frac{C}{Rt} \right)^n. \quad (5.9)$$

Here, V is the voltage, Rt is the hour rating, C is the battery capacity in ampere-hours, i is the discharge current and n is a hyper-parameter that accounts for the physical properties of the cell as well as its operating conditions. It is important to note here that this is but one of the many proposed expressions to represent the available electrical load on discharge, oftentimes chosen due to its ease of implementation. More accurate methods worth mentioning for estimating the current drawn at a particular SOC include higher fidelity, physics-based methods such as the pseudo-two-dimensional or porous electrode diffusion models and medium-fidelity methods such as the equivalent circuit model which used in this study.

Through energy balance of the system, Equations 5.6c and 5.9 can be rearranged to obtain the endurance, t , given as:

$$t = Rt^{1-n} \left[\frac{\eta_{tot} VC}{\frac{1}{2} \rho U^3 S C_{Do} + (2W^2 k / \rho U S)} \right]^n \quad (5.10)$$

where η_{tot} is the combined efficiency of the system subcomoments. A simpler form of this expression can be obtained without the decomposition of drag into its components and using the assumption that V is the nominal voltage, allowing the substitution for battery energy $E = VC$, and the assumption that $n = 1$.

$$t = \eta_{tot} \frac{E L/D}{WU} \quad (5.11)$$

where η_{tot} is the combined system efficiency and L/D is the lift-to-drag ratio at steady, level flight and E is the available energy, taken as 80% to the total energy of the pack. We can use Equation 5.11 to compare this tradition approach for estimating endurance to the findings in this paper. Shown in Figure 5.16 is the maximum achievable range over time for three of the four aircraft, superimposed on by trend lines corresponding to different system efficiencies. Not withstanding the constant airspeed and altitude assumption, a noticeable disparity in performance can be observed as the battery pack ages. Moreover, we see that for the two winged EVTOL aircraft in Figures 5.16(b) and 5.16(c), the low system efficiencies bisecting the aircraft limits predicted by the model suggest that the use of traditional approaches are not suitable for estimating endurance.

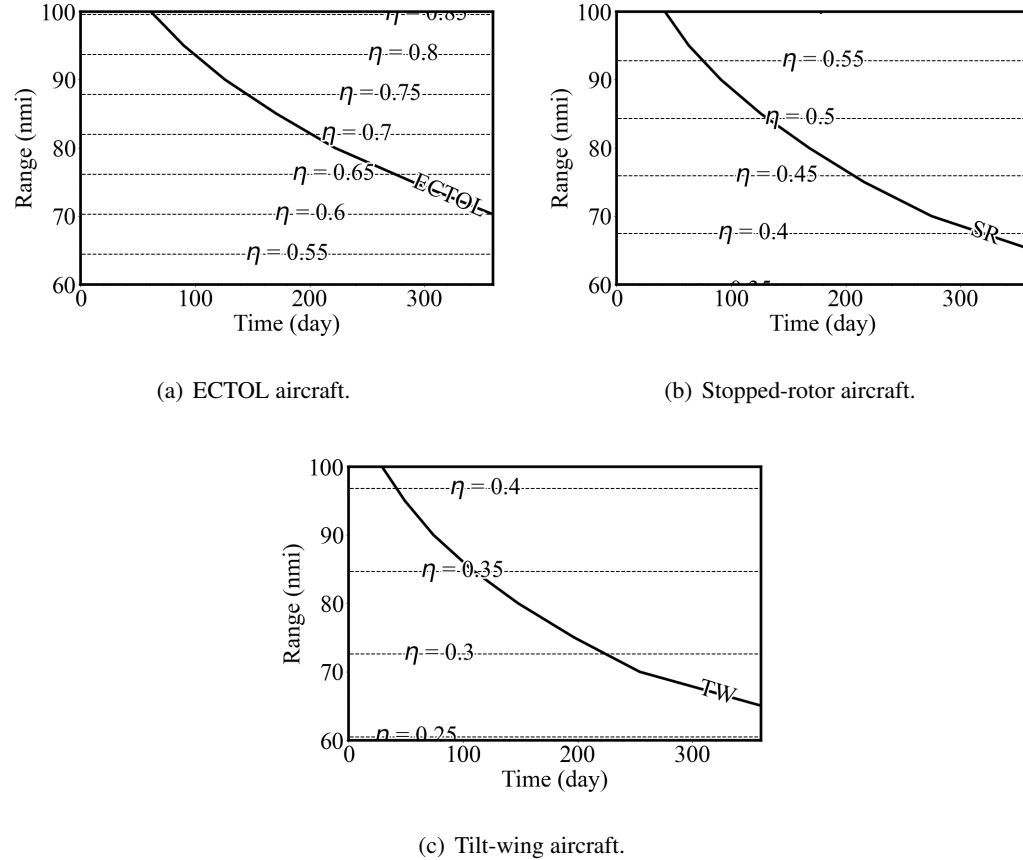


Figure 5.16: Comparison of Aircraft Endurance Trends Using Battery Degradation Modeling and Traditional Electric Range Equation.

5.6 Chapter Summary

In this chapter, we demonstrate the use of medium-fidelity tools and physics-based approaches to design and analyze electric aircraft operating mission profiles symbolic of those envisioned for regional and urban air mobility. Although this approach presents challenges related to convergence, the act of using realistic estimates of vehicle weight, including technology limitations and modeling vehicle geometry in great detail allows for a deeper understanding of the interactions between subsystems. Moreover, as shown by the nuances in battery performance throughout the flight profiles, this approach allows for the identification of phenomena that commonly go unnoticed when using

simpler models are employed.

From the comparison of the modeled aircraft configurations, it was observed that battery technology and noise emission at low altitude emerge as the most significant issues to be addressed if designers hope to reify the integration of electric aircraft into urban airspaces. On the topic of batteries, it was observed that vehicle configuration has a strong correlation the weight fraction, being as much as 65 % of wingless multi-rotor. The development of batteries with higher specific energy and specific power is therefore essential for reducing TOGW. With respect to radiated noise, any attempt to reduce the acoustic signature of these aircraft will first require the capturing of all generating sources. This includes rotor-on-rotor wake interactions and unsteady wing loads in a propeller slipstream. This will be the focal point of future studies. Design optimization of these aircraft can subsequently be carried out upon obtaining more accurate predictions of the emitted noise. Additionally, we intend to explore methodologies for propulsion network optimization that more tightly couple rotor blade design and motor sizing. In particular, future lift-rotor design will take into consideration both geometric and acoustic constraints.

Another area of future research is the examination of vehicle stability, principally in transition by way of modeling propeller-motor and rotor-motor combinations around the aircraft as separate systems with unique throttles. This undertaking will be preceded by a reformulation of the mission solver to allow for the use of gradient information which is expected to significantly improve convergence. Lastly, it was previously mentioned that the impact of cycling and calendar aging on the battery is not considered in this study. Upcoming research will look at the inclusion of mechanistic models that capture some of the chemical state changes occurring within the battery cell together with thermal fatigue from repeated operations.

Chapter 6

Multidisciplinary Analysis and Design Trade Studies

6.1 Introduction

The advantages of adopting a detailed approach to modeling components on board the aircraft, followed by simulation over realistic flight profiles, were made evident in the previous chapter. Not only did the results help us ascertain a better understanding of the performance of drastically different vehicle configurations, but they also highlighted what attributes of the aircraft itself as well as the operation over repeated flights require further attention. In this chapter, we examine a few of these areas, particularly rotor blade design to address vehicle noise and battery pack layout for reducing the thermal load on battery cells.

This chapter consists of five main sections, the first of which provides an overview of rotor blade optimization. Following this in Section 6.3 is an in depth examination of how changes in rotor design and operating conditions affect performance and radiated noise. Sections 6.4 and 6.5 discussion approaches developed for designing lift-rotors and prop-rotors respectively. Provided in the last subsection is a practical application of the lift-rotor design methodology covered in Section 6.6. Here, the stopped-rotor is used as the baseline aircraft to study the aeroacoustic and system efficiency impacts of blade selection.

6.2 Rotor Design Blade Optimization

One of the most effective means of reducing the acoustic footprint of propeller-driven aircraft and rotorcraft is through the design and operating conditions of the rotor blades. In the absence of noisy ICE turbo-machinery, the rotor blade and its generated wake stand out as the main sources of electric-powered aircraft noise. Accordingly, developers of new vehicle concepts spend considerable time designing quiet architectures that will meet the stringent targets put forth by regulators and representatives of local governments. Presented in this section is a new, robust methodology for designing low-noise rotors. Before this approach is discussed, however, the historical approach to blade design is expanded upon to provide context to strategies taken in subsequent subsections.

In 1999, Roger Scherer published an article in *Renewable Energy* 6.1 that summarized the several aspects of blade design. In this manuscript, he noted that blade design was split among two domains, aerodynamic design and structural design (weight and strength). Though interest in low noise blades was present at the time, its place in the design process took a backseat, oftentimes left as a post-optimization step or being omitted altogether. Today, increased air traffic and the emergence of new applications such as RUAM have resulted in the higher annoyance of communities in the vicinity of airports. Consequently, incorporating noise objectives or thresholds into the design process rotors have become commonplace. With this in mind, Sheherer's original flowchart of parameters for blade design can be modified to include acoustics. This is provided in Figure 6.1 where the three methods are elaborated below:

- Aerodynamic design - for the desired thrust, the aerodynamic efficiency is typically computed as a function of the power coefficient (cp) and advance ratio, λ . The main parameter for obtaining an optimum power curve, that is a board curve where performance is high over a wide range, are the rotor diameter, rotational speed and pitch angle.
- Structural design - this can be interpreted as the combination of the weight of the blade and the strength of the blade. First, with respect to weight, dynamic loads incurred during operation are proportional to the wight of the blade and impact the power requirement of the motor. As a result, full system efficiency decreased with heaver blades as more energy is required to

overcome both in-plane and out-of-plane torques. Secondly, the blade strength and durability of the rotor are governed by the properties of a particular material. More specifically, the choice of material dictates the stiffness, modulus of resilience which is the area under the linear portion of the stress-strain curve up to the proportional limit, and fatigue limits the blade can incur after repeated loading and cycling.

- Aeroacoustic Design - Blade geometry and loading, interactions radiated pressure fluctuations over time from multiple blades and interaction of wake on other components of the airframe such as wings and fuselage all contribute to the total acoustic spectrum recorded at a given observe. Generally speaking, reducing the interference experienced when generating lift reduces the sound generated for a rotor blade. This will be expounded upon in the following section.

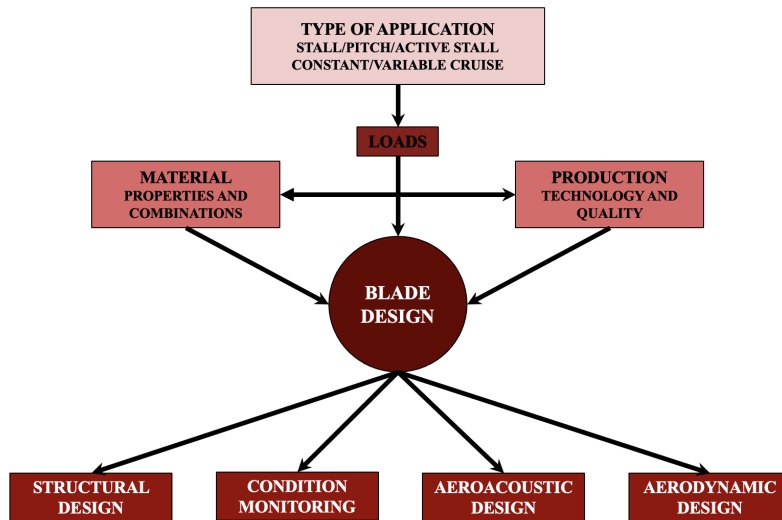


Figure 6.1: Rotor Blade Design. Adapted from Scherer [6]

6.3 The Impact of Rotor Geometry and Performance Parametric on Radiated Noise and Aerodynamic Efficiency Spectrum

Understanding how geometric parameters and performance characteristics affect the total acoustic spectrum is crucial to interpreting the behavior of the variables during the optimization process and the arrived solution. These geometric variables include properties such as blade twist and chord distribution while aerodynamic characteristics like sectional blade loading as well as how this loading changes along the span of the blade. Provided in below is the impact of isolated parameters on the noise and aerodynamic efficiency impact. We begin with the assertions that:

- We start from a generic rotor designed to produce a given thrust, T_0 and a given advance ratio, λ_0
- This rotor is operating at the peak power.
- This baseline rotor has a simple chord and twist distribution, for example, constant chord and linear washout twist from rotor hub to tip.
- One parameter can be isolated and studied at a time.

Tip Speed

Acoustic Impact: Increasing the tip speed of a rotor rapidly increases the noise generated by a propeller. As the tip speed decreases, the contribution of thickness noise decays faster suggesting that this component is the more sensitive rotational noise parameter in the total radiated noise.

Aerodynamic Impact: Assuming that rotor is operating at its ideal conditions, any change in tip speed will reduce the efficiency of the rotor blade. Increasing tip speed will increase thrust, but also the induced losses incurred from drag on the blades. A reduction in tip speed will reduce blade thrust below the designed requirement.

Blade Solidity

Acoustic Impact: Rotor solidity, σ , is the ratio of the total blade area to the rotor disk area. Low blade solidity (higher aspect ratio blades) means smaller chords which result in a reduction in thickness noise because the volume displaced by each blade decreases. A reduction in solidity does however mean that either the loading on each blade must change or the number of blades must be increased to supply the same thrust at a given RPM. In the second case, the blade passing frequency will increase, and depending on where these frequencies are in the acoustic spectrum can be more or less important after applying the A-weighting scaling.

Aerodynamic Impact: Holding rotor diameter constant, decreasing rotor solidity improves the Figure of merit for rotor or efficiency propellers. If the rotor solidity is too low, however, high angles-of-attack are needed to achieve the required lift, and as a result the profile drag increases. Therefore the rotor should have as small a solidity as possible with an adequate stall margin.

Disc Loading

Acoustic Impact: Lowering disc loading results in a reduction in loading noise emanating from the rotor. To generate a given thrust, however, the area of the rotor itself or the number or number of rotors must increase. The first leads to increasing tip speed so we refer the reader to that row in this table. In the second case, multiple rotors can have both positive and negative impacts on the overall acoustic spectrum depending on their phasing. If the rotors are in phase, the sound pressure level at the characteristic frequencies will be amplified, which may offset the decrease in disc loading. If the rotors are out of phase, cancellations could lead to a redistribution of energy across the frequency spectrum leading to lower noise.

Aerodynamic Impact: For the rotary wing in hover, the induced power loading is inversely proportional to the square root of the rotor disk loading. Hence the efficiency of rotor thrust generation increases as the disk loading decreases.

Number of Blades

Acoustic Impact: Increasing the number of blades increases the fundamental blade passing frequency which can diminish the effect of A-weighting scaling.

Aerodynamic Impact: Increasing the number of blades reduces the efficiency of the rotor due to wake interference and aerodynamic drag.

Blade Cross Section: Local Chord and Thickness

Acoustic Impact: First with respect to thickness noise, increasing blade sectional area increases this harmonic noise component of rotational noise. Examining the integral in Equation 3.29 for thickness noise in Chapter 3, the factors influenced by airfoil section geometry at a given radius are the section thickness-to-chord ratio, t_b and the section chord-to-diameter ratio, B_d . Since the product $t_b B_d$ is proportional to the airfoil cross-sectional area, the noise from a radial strip dz is proportional to $t_b * B_d * dz$, to the volume displaced by the strip.

With respect to loading noise, the blade cross-sectional properties impact the loading term, Ψ_L , in Equation 3.30 which itself is a function of the sectional lift coefficient and the chord to diameter ratio. Thus, loading noise is proportional to $C_L * B_d$ or sectional lift. In the scenario where we are using a particular airfoil for a section and we seek to keep the sectional lift fixed, increasing blade chord implies there must be a reduction in section lift coefficient. the associated increase in blade thickness however does results in an increase in thickness noise. Secondly with respect to loading noise, Hanson [62] highlights why strong peaks in the chordwise loading distribution should be avoided in order to benefit from chordwise noncompactness, particularly for the prop fan cruise conditions. He further goes on to show how chordwise distribution also affects the phase of loading. Shifting the load toward the trailing edge causes a phase lag which could in theory be used to promote phase cancellation between signals from different radii on the blade. This would be difficult in practice.

Aerodynamic Impact: Increasing blade cross-sectional area decreases the efficiency

6.3. THE IMPACT OF ROTOR GEOMETRY AND PERFORMANCE PARAMETRIC ON RADIATED NOISE AND VIBRATION

of the rotor as parasitic drag increases

Rotor Radius

Acoustic Impact: To keep the required thrust produced by a single rotor fixed, reducing the radius of the propeller will require an increase in blade loading which will correspond to an increase in the sound radiated. If however we fix the RPM and choose to increase the number of rotors, reducing the radius of the rotor can lower the sound pressure level as load distribution and move inward to the rotor hub, causing more noise to be radiated at the lower harmonics which, once taking into account perceive noise weighting results in a lower overall sound pressure level.

Aerodynamic Impact: In the first case, decreasing rotor radius lowers efficiency as the solidity increases causing a reduction in aerodynamic efficiency as induced losses increase.

Blade Spacing

Acoustic Impact: Uneven blade spacing results in the redistribution of harmonic energy over the acoustic spectrum – the blades produce a greater number of lower amplitude harmonic tones resulting in the redistribution of acoustic intensity similar to a “broadband-like” spectrum. This phenomenon essentially follows the principle of sinusoidal modulation where negative pressure fluctuations can cancel out positive amplitudes. Large amounts of acoustic intensity were shifted into the lowest frequency tone (occurring at half of the blade passage frequency of the propeller with evenly spaced blades), resulting in reductions of A-weighted overall sound pressure levels.

Aerodynamic Impact: The generated tip vortex from the preceding blade can reduce the efficiency of the following blades leading to a reduction in lift, increase in drag, and an overall drop in aerodynamic efficiency.

Blade Twist

Acoustic Impact: Keeping the planform (chord distribution) constant and radius fixed, retwisting the blade to move radial load distribution inboard leads to a shifting of the strength of harmonics within the spectrum. This shifting will place more emphasis on the lower harmonics that are significantly penalized in the A-weighting leading to an overall reduction in overall sound pressure levels.

Aerodynamic Impact: The optimal loading of rotors for minimum induced losses is typically around the 80% radial location. Shifting the load distribution inboard will result in an increase in operating lift coefficient of blade sections near the hub. With airfoils no longer operating at their design lift coefficient, the section performance degrades (sectional drag coefficient increases) and thus the overall propeller efficiency reduces.

Blade Chord

Acoustic Impact: Increasing the blade chord near the rotor hub is another way to increase the lift on inboard sections of the blade and thus altering radial load distribution without changing the sectional lift coefficient. It was found that chord distribution alterations to rotor blade can produce a similar acoustic signature to retwisting with a lesser impact on efficiency

Aerodynamic Impact: Larger inboard chords will produce greater parasitic drag and degrade performance. Similar to retwisting the rotor blade, a redistribution of load will cause a drop in overall efficiency.

Blade Sweep

Acoustic Impact: There are two benefits associated with sweeping a rotor blade. The first is the reduction of transonic compressibility effects similar to the principles used for swept-wing design on high-speed aircraft. Studies have shown that this reduces the strength of the quadrupole sources as they are primarily transonic flow phenomena

[62]. The second effect is the dephasing of noise radiating from different portions of the blade resulting in the redistribution of acoustic energy.

Aerodynamic Impact: Heavily loaded blade tips will generate strong tip vortices that reduce overall efficiency.

6.3.1 Parameterization Shape Functions

Optimization of the rotor blade typically involved discretizing the blade into equally spaced sections along from the hub to the tip, then performing geometric alterations to meet a desired performance. Even with a coarse rotor blade characterized by 20 radial stations, the design problem can become quite large, with over 100 parametric variables; 20 sections chords, 20 sectional twists, 20 airfoil cross-sections, 20 sectional sweep angles and 20 sectional face alignment angle. Obtaining design objective and performance constraint sensitivities to each of these variables would be extremely memory intensive. If inadequate or insufficient parametric constraints are defined, the resultant optimized blade may have peculiar deformities that would be expensive to reproduce using modern day manufacturing techniques. Moreover, with so many design variables, the propensity of the optimizer to be stuck in local minima significant rises and objective functions become highly non-linear. To combat such a scenario, a new approach that parameterizes the variations of attributes along the blade is adopted. Gaining inspiration from work by Traub et al. [132] that adopted a similar approach for the optimization of low Reynolds number planar wings, the shape function below yields a variety of permissible planform shapes including elliptic and rectangular and shown in Figure 6.2, making it suitable for blade design applications.

$$c_n = c_r (1 - \eta_n^p)^q c_t \eta_n \quad (6.1)$$

where p and q are hyperparameters and c_r and c_t are pivot points near the root and tip section. The normalized spanwise location along the blade, η_n is given as

$$\eta_n = \left| \frac{y_n}{b} \right|. \quad (6.2)$$

The location of spanwise station denoted y_n is given by

$$y_n = b \cos(\theta_n), \quad (6.3)$$

where θ_n defined below is angular spanwise location varying, with n ranging from 0 to $N-1$, where N the total number of stations used to define the rotor blade

$$\theta_n = \frac{n\pi}{2r}. \quad (6.4)$$

In the above expressions, b is the non-dimensional radius at the tip. During optimization, characteristics of the blade can therefore be represented by a total of four values – the two pivot points and two hyperparameters – rather than 20 sectional values. This reduces the size of the Jacobean and Hessian matrices that contain gradient information used by the optimizer. What is ultimately observed is a reduction in computational time to obtain a optimal solution.

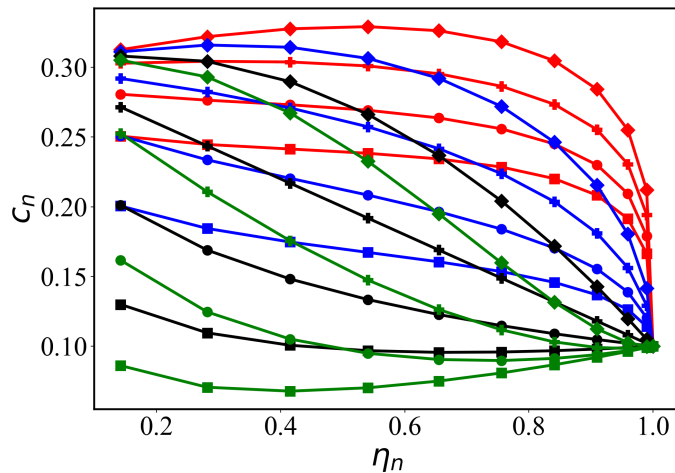


Figure 6.2: Rotor blade parameterization shape functions with $c_r = 0.3$ and $c_t = 0.1$. Markers: ■ for $p = 0.25$, ● for $p = 0.5$, + for $p = 1$, ♦ for $p = 2$. Lines: red for $q = 0.25$, green for $q = 0.5$, blue for $q = 1$, black for $q = 1.5$.

6.4 Lift-Rotor Design

6.4.1 Formulation of Lift-Rotor Design Problem

Now that a comprehensive understanding of how blade design and operating conditions impact the acoustic signature emanating from a rotor, we can turn our attention to design optimization. A weighted-sum approach was selected to solve this multi-objective problem where both performance and noise are considered. In the first case presented below, the planform of a rotor blade intended for vertical flight is covered. The design conditions were taken from that of one lift-rotor of the stopped-rotor aircraft, implying a design load of 2207 N. The design variables in this optimization were chord and twist distribution, along with tip mach number. Lastly, the NACA 4412 airfoil was selected as the single cross-sectional profile along the entire span of the blade. Once again, aerodynamic coefficient surrogates were first constructed, reducing evaluation time each iteration of the BEVT during the optimization routine. This optimization problem is presented below:

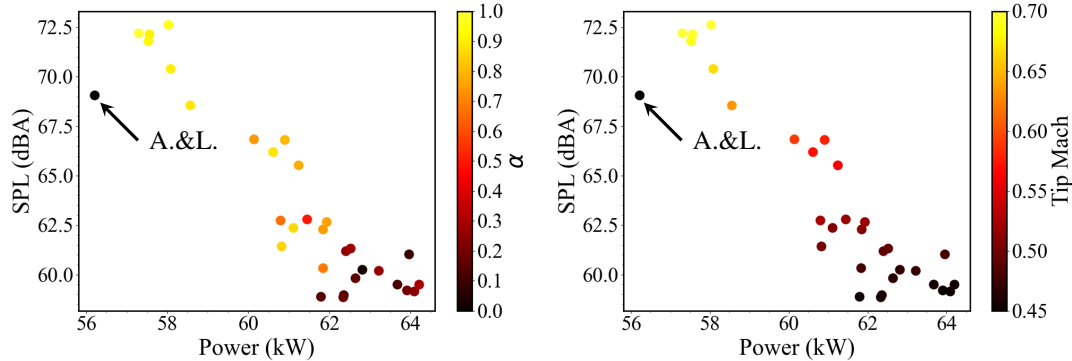
$$\begin{aligned}
 \min \quad & f(X) \text{ where, } f = \left(\left| \frac{(FM - FM^*)}{FM^*} \right| \right) \alpha + \left(\left| \frac{(\overline{SPL} - SPL^*)}{SPL^*} \right| \right) (1 - \alpha) \\
 \text{s.t.} \quad & T = T_{design} \\
 & C_{l_{max}} \leq 0.8 \\
 & 0.3 \leq \lambda \leq 0.7 \\
 & \frac{c_p}{c_q} \geq 0.5 \\
 & \frac{\beta_p}{\beta_q} \geq 0.5
 \end{aligned} \tag{6.5}$$

where α is an aeroacoustic objective weight, FM is the Figure of Merit, \overline{SPL} is mean the sound pressure level of the rotor measured in dBA. The (*) is used to signify the ideal Utopian points in this weighted optimization. Here FM^* is taken as 1 and SPL^* is taken as 45 dBA. As can be seen from Equation 6.5, a minimum taper of 0.3 was implemented to ensure that the blades were structurally sound at the tip since no aero-structural analysis was performed – very thin blade tips

have the propensity to break when heavily loaded. This third discipline will be considered however in future work. Optimizations were executed using SUAVE's nexus framework with the Scipy's native Sequential Least Squares Programming (SLSQP) optimizer [133]. Due to the precision of the BEVT and aeroacoustic analysis, a step size of 1×10^{-4} was chosen with a termination tolerance of 1×10^{-3} .

6.4.2 Lift-Rotor Design Optimization Results

The trade-off between aerodynamic-focused optimization and aeroacoustic-focused optimization can be seen in Figures 6.3(a) and 6.3(b) with the formation of Pareto frontiers capturing their inverse relationship. This relationship can be summarized as follows: Aerodynamically efficient blades that consume less power generate stronger pressure signatures that result in higher noise signatures. On the other hand, rotor blades that emit lower noise signatures are less aerodynamically efficient, requiring high power. The distribution of optimized designs followed the expected trend in α whereas alpha decreases from 1 to 0, that is, moves from favoring aerodynamic efficiency to aeroacoustic performance, the noise level drops and power consumption increases. Figure 6.3 suggests that reducing the blade tip speed is an effective way of reducing radiated noise from the blade. This can be explained with the aid of the A-weighting scale depicted in Figure 3.10 in Chapter 3. Tailored for the human ear, this scale applies an increasing penalty to the raw dB prediction, with



(a) Aeroacoustic objective distribution of optimized lift-rotor designs. (b) RPM distribution of optimized lift-rotor designs.

Figure 6.3: Objective weight and RPM distribution of optimized rotors.

readings below 1 kHz attaining a more negative weighting as one moves further away. By lowering the rotor tip speed, the tonal noise will be produced at lower blade passing frequencies, this experience is a more significant reduction in weighing. Figure 6.4 below depicting the acoustic signature for $\alpha = 1$ and $\alpha = 0.5$ can be used to further elucidate this point.

Figures 6.5(a) to 6.5(d) provide more insightful takes on the design of low-noise rotors that must be overlooked. Shown here is the comparison of optimized blade planforms using the new design approach to a planform obtained using the Adkins and Liebeck (A. & L.) [123] (black line) approach in which the blade twist and chord distributions are designed to achieve a constant sectional lift-coefficient along the span of the blade. It can be seen that A. & L.'s approach is not suited for rotor design as the absence of constraints on the blade shape results in highly tapered, unrealistic designs. Investigating the governing principles behind their approach, it can be gathered that the creation of a blade was precisely what was expected as the optimizer would seek to increase the chord near the hub, where the airspeed is low, generate similar sectional lift coefficients as the tip. Examining the first two figures in the top row of Figure 6.5, we see that low-noise rotors are characterized by thicker chord distributions and a smaller variation of twist from root to tip than more efficient, noisier blades. If the taper constraint of the blade was not instituted, the most aerodynamically efficient blade, $\alpha = 1$, would see the planform approach distributions similar to the A. & L. method. Moreover, it is important to note that however increase in blade solidity as the blade designs generate lower noise. In fact, this along with the increasing load on the blade as

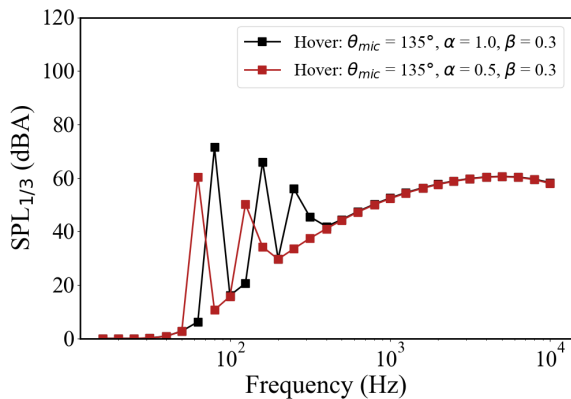


Figure 6.4: 1/3 Octave-band spectrum comparison of optimized rotor designs.

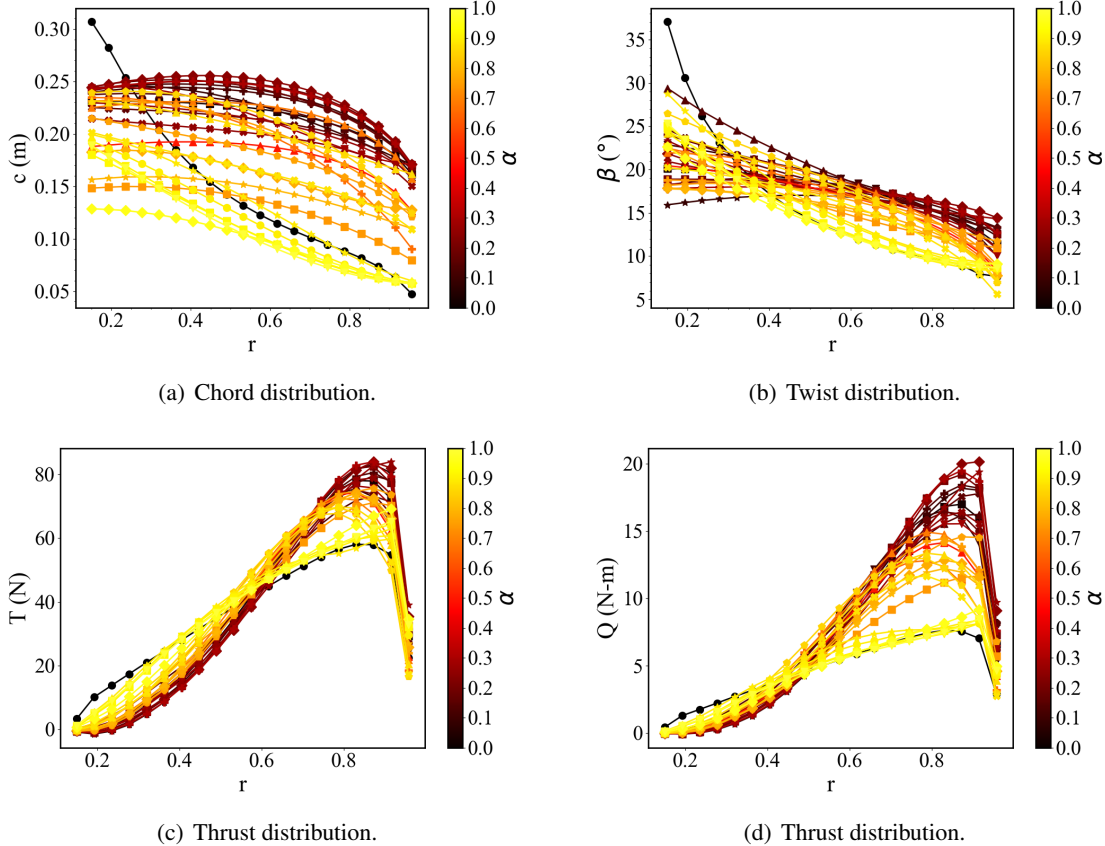


Figure 6.5: Comparison of rotor blade designs from $0 \geq \alpha \leq 1$.

alpha decreases from 1 to 0 both run contrary to the previously discussed design trends in Section 6.3 on the effect of operating conditions on the acoustic signature of the blade. However, if we recall that these observed trends manifest with an associated decrease blade tip Mach number, it can be concluded that in the aeroacoustic optimization of rotors for low noise, the impact of angular velocity dominates.

6.5 Prop-Rotor Design

6.5.1 Formulation of Prop-Rotor Design Problem

The design of rotors that serve to generate lift during hover and vertical climbs as well as propeller the aircraft in high-speed cruises is somewhat more involved as there are endless flight conditions between these two extremities. In practice, these prop-rotors are operating with the aid of variable pitch control, granting the propulsion architecture the achieve better efficiency depending on the flight regime. At low air speeds, the blade pitch-command is low or fine. At higher air speeds, pitch-command increases or becomes coarse. Such changes in blade pitch have already been shown but not explicitly highlighted in Table 5.5 of Chapter 5 where the flight profile and aircraft power-train settings are discussed. With respect to the design of the blade itself, there are a few common strategies typically used to generate a given a prop-rotor. The first of which is to design the rotor blade for one design load and flight condition and use variable pitch to tailor the performance of the blade. An issue with this approach however is that this single design point must be chosen with caution. Moreover, in practice, pitch command can only be varied so much, typically between $\pm 30^\circ$. The second approach is the chose two design conditions, lets say the extremities (hover and cruise) and use a weighted optimum to arrive an a single design. These two approaches do not necessarily require complete mission analysis a priori. The third and final approach however does, and involved mission analytics to determine an optimization strategy. For example, for a specific mission, one may opt to first determine what flight condition dominates in terms of energy conception and use this as the focal design point. Whatever rotor blade design strategy, be it one of the three listed here, a combination of, or a completely different approach all together, a final comprehensive assessment of the rotor blade over a full mission must be performed to ensure that the selected design possesses desired traits.

The approach selected for further discussion in this section is the second one, where the design thrust for hover and cruise were taken to be 2820 N and 176 N respectively. The tip mach of the blade was allowed to vary between a range of 0.65 and 0.3, and the pitch command between the range $\pm 30^\circ$. In addition to the aeroacoustic objective weight, α discussed in the previous section,

two additional objectives weights, β and γ are introduced into the weighted-sum objective function. These two weights enables the designer to tailor the trajectory of the design, that is, to prioritize the hover segment performance over the cruise segment performance in the first instance or to prioritize the hover segment noise over the cruise segment noise in the second instance. The optimization problem is provided below. The subscripts *hov.* and *cr.* denote hover and cruise receptively.

$$\begin{aligned}
 \min \quad & f(x) \text{ where, } f = f_{aero.}(\alpha) + f_{acous.}(1 - \alpha) \text{ and} \\
 f_{aero.} &= \left(\left| \frac{(FM_{hov.} - FM^*)}{FM^*} \right| \right) \beta + \left(\left| \frac{(\eta_{cr.} - \eta^*)}{\eta^*} \right| \right) (1 - \beta), \\
 f_{acous.} &= \left(\left| \frac{(\overline{SPL}_{hov.} - SPL^*)}{SPL^*} \right| \right) \gamma + \left(\left| \frac{(\overline{SPL}_{cr.} - SPL^*)}{SPL^*} \right| \right) (1 - \gamma), \\
 \text{s.t.} \quad & T_{hov.} = T_{hov.}^*, \\
 & T_{cr.} = T_{cr.}^*, \\
 & C_{l_{hov,max}} \leq 1.0 \\
 & C_{l_{cr,max}} \leq 0.8 \\
 & 0.3 \leq \lambda \leq 0.7 \\
 & \frac{c_p}{c_q} \geq 0.5 \\
 & \frac{\beta_p}{\beta_q} \geq 0.5
 \end{aligned} \tag{6.6}$$

The above methodology can be simplified with the assertion that we are not interested in aircraft noise at high altitudes in cruise but near the ground in hover. With that, γ in Equation 6.6 is fixed at $\gamma = 1$. This reduces the number of weights to two – α and β . Highlighted below are two design studies, the first keeping β fixed while examining optimized blades using different α values. The second study holds α constant and examines a variation in the β value.

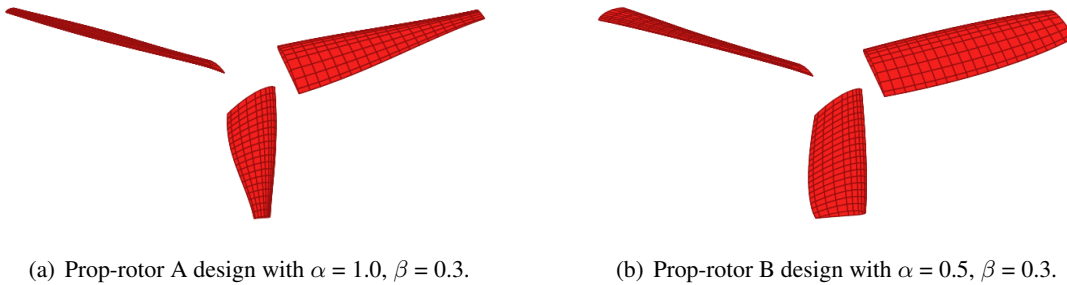
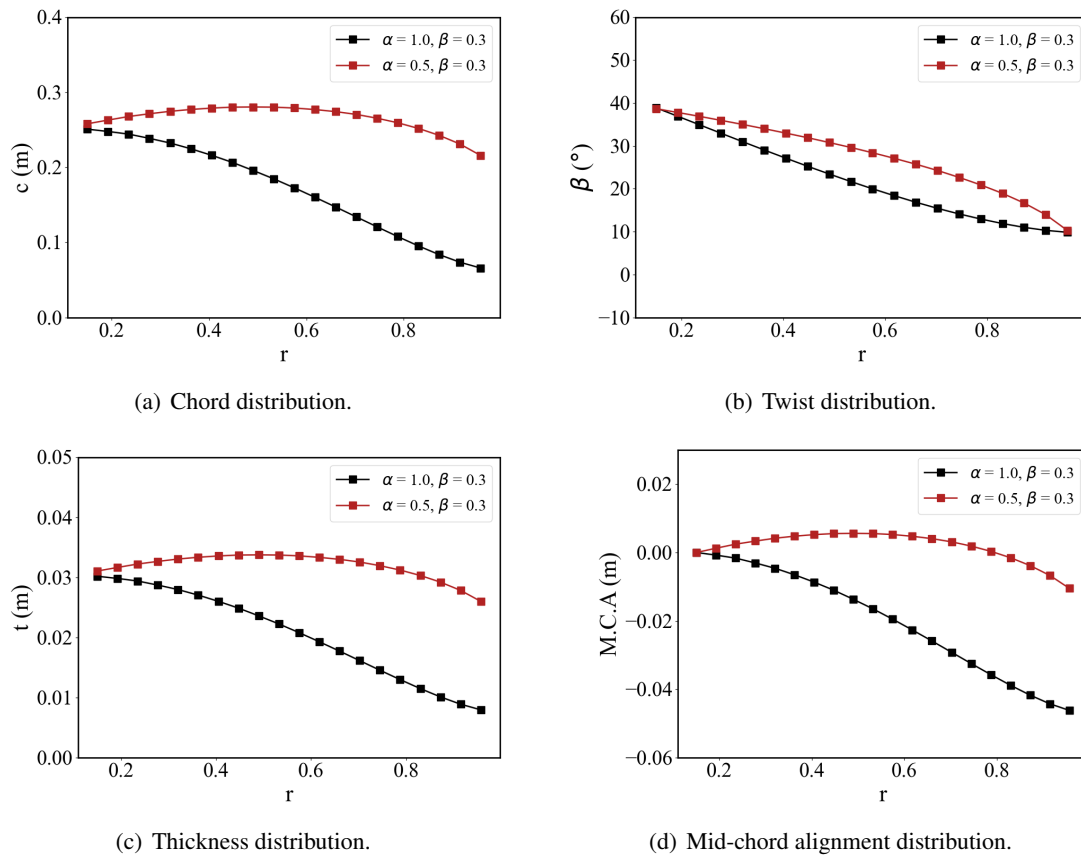
6.5.2 Prop-Rotor Optimization Results: Case 1 - Alpha Variation

In this section a comparison of two prop-rotor designs is made. The first design favors aerodynamic performance with $\alpha = 1$ while the latter prioritizes noise in the optimization with $\alpha = 0.5$.

The hover/cruise segment performance weight, β is held fixed at 0.3 implying that in the objective function, cruise is favored slight more. The results presented below corroborates the conclusions made from findings of the previous section about lift-rotor design. Table 6.1 provides a summary of the optimization results. We see that prop-rotor A does indeed does have better performance than blade B, requiring 5.3 % less power in hover and 22 % less power in cruise. This however comes at the expense of noise where in the hover condition, this blade is about 5 dBA louder than prop-rotor B. It can also be gathered from the results that the optimal commands did not reach the extremities of the bounds specified in the optimization problem, implying that the aircraft does have some bandwidth, albeit little, for both off design operation and certification test flights where the plane is pushed beyond its limits. From depictions of the rotors in Figure 6.6 and the profile of geometric properties in Figure 6.7, it can be inferred that low-noise prop-rotor designs are indeed characterized by high solidity. Another important observation here can been seen in the comparison of performance in Figures 6.8(a) to Figures 6.8(d). For prop-rotors, the tradeoff in blade performance typically implies a reduction in overall blade twist meaning a significant portion of the lift in the hoer is carried on the outboard sections of the blade. In cruise, even with the aid of pitch command to improve aerodynamic performance, such a twist distribution can result in stall near the hub of the blade. This phenomenon is can been identified in Figure 6.8(a).

Table 6.1: Summary of optimized rotor blade characteristics at design conditions for the first prop-rotor design case.

	Parameter	Rotor A	Rotor B
Optimization Weights	α	1.0	0.5
	β	0.3	0.3
	γ	1.0	1.0
Hover Flight Condition	Pitch Command ($^{\circ}$)	-5	-7
	SPL (dBA)	74.28	69.66
	Power (kW)	75.56	79.84
	Tip Mach	0.65	0.45
	RPM	1703	1191
Cruise Flight Condition	Pitch Command ($^{\circ}$)	29	22
	SPL (dBA)	-	-
	Power (kW)	16.98	21.87
	Tip Mach	0.30 0.30	0.30
	RPM	786	786

Figure 6.6: Optimized rotor blade designs constant β of 0.3.Figure 6.7: Geometry of two rotor blade designs. Rotor A (black) with $\alpha = 1.0, \beta = 0.3$ and Rotor B (dark red) with $\alpha = 0.5, \beta = 0.3$.

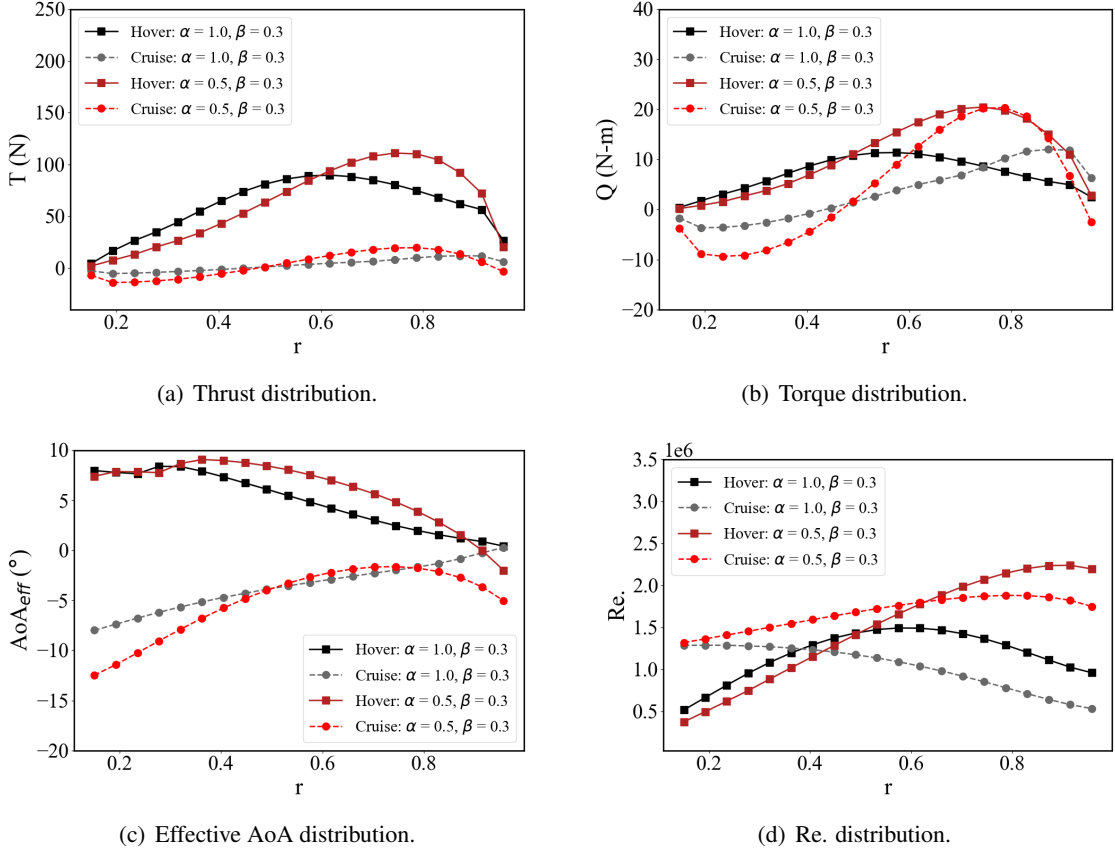


Figure 6.8: Performance of two rotor blade designs. Rotor A (black and gray) with $\alpha = 1.0, \beta = 0.3$ and Rotor B (dark red and red) with $\alpha = 0.5, \beta = 0.3$.

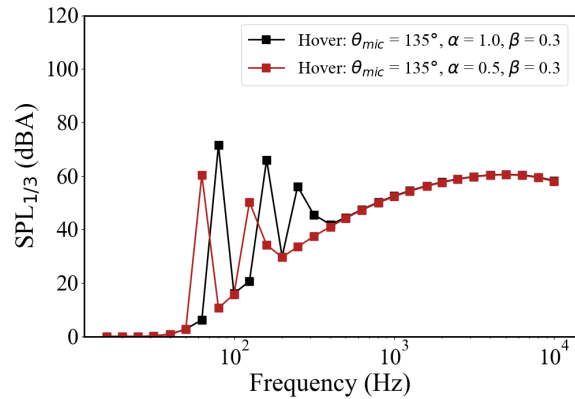


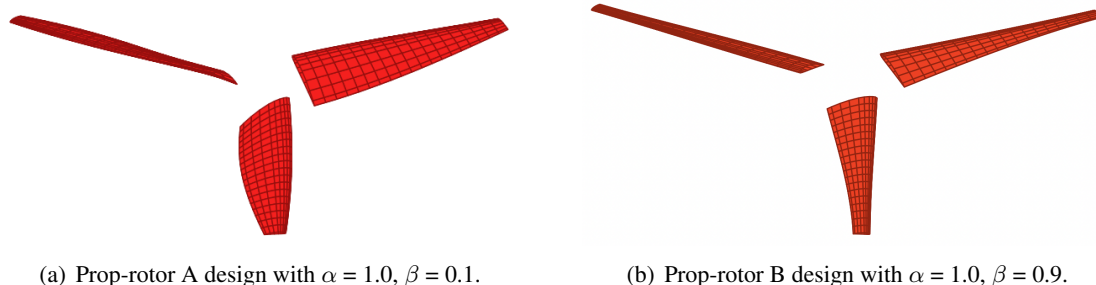
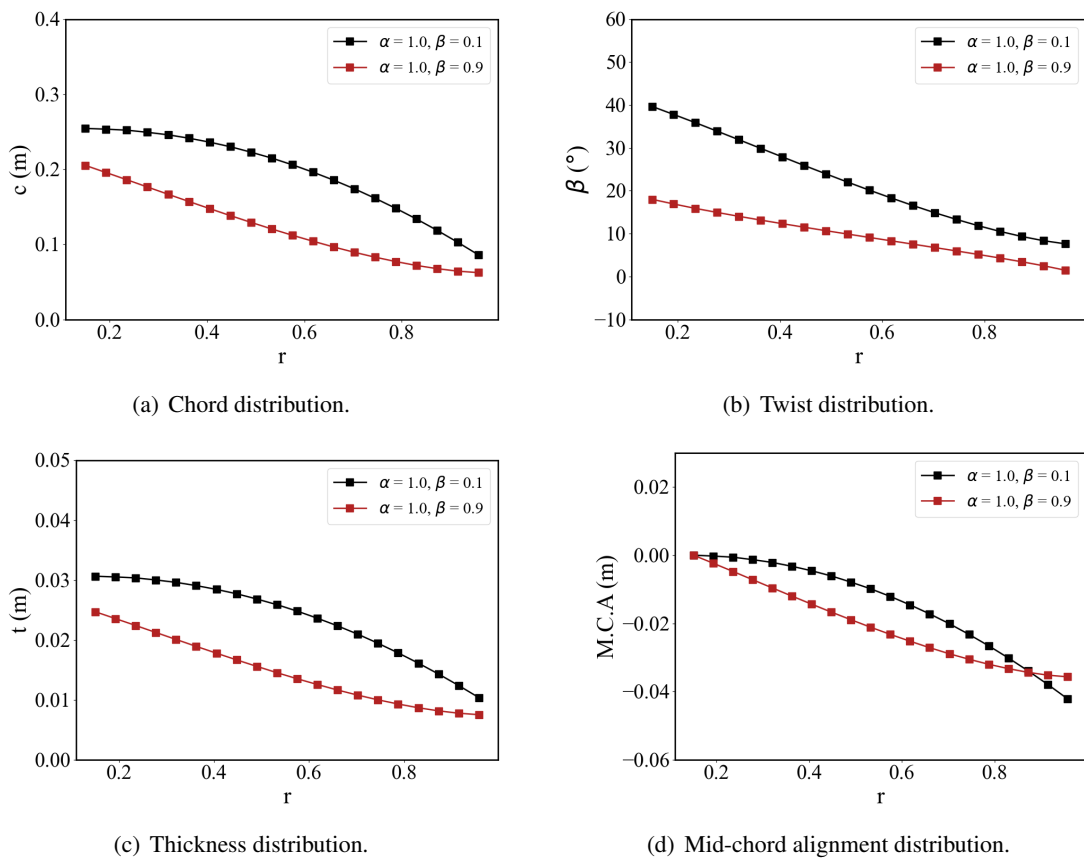
Figure 6.9: 1/3 Octave-band spectrums of two rotor blade designs. Rotor A (black) with $\alpha = 1.0, \beta = 0.3$ and Rotor B (dark red) with $\alpha = 0.5, \beta = 0.3$.

6.5.3 Prop-Rotor Optimization Results: Case 2 - Beta Variation

In the second design study, the aeroacoustic objective weight is held fixed at $\alpha = 1$ while the hover/cruise segment performance weight is varied. Recalling that with $\alpha = 1$, noise is not considered in the design problem and correspondingly aeroacoustic analyses are omitted in this optimization routine. Going back to formulation of the design problem in Equation 6.6, we see that the higher a value of β , the more hover performance is favored. This implies that prop-rotor A prioritizes cruise performance while prop-rotor B prioritizes hover performance. The results shown in Table 6.2 confirm this with prop-rotor A outperforming prop-rotor B in cruise but requiring more power in hover. From the planforms of the two prop-rotors shown in Figure 6.10 along with the distributions of geometric parameters in Figures 6.11, it can be inferred that to achieve better performance in hover, the use of pitch command is preferred to increasing chord as shown by the slender blades of prop-rotor B. This makes sense, as lowering solidity increase aerodynamic efficiency. More importantly, it suggests that changes in sectional chord have a greater impact on drag than changes in sectional twist. Moreover, given that both blades operate at similar RPMs in hover, the higher SPL recorded for prop-rotor A can be attributed to the higher thickness noise contribution to the overall acoustic spectrum as shown in Figure 6.13. This verifies the expected behaviour discussed in Section 6.3.

Table 6.2: Summary of optimized rotor blade characteristics at design conditions for the second prop-rotor design case.

	Parameter	Rotor A	Rotor B
Optimization Weights	α	1.0	1.0
	β	0.1	0.9
	γ	1.0	1.0
Hover Flight Condition	Pitch Command ($^{\circ}$)	-5	6
	SPL (dBA)	76.24	72.96
	Power (kW)	81.49	66.91
	Tip Mach	0.65	0.65
	RPM	1703	1703
Cruise Flight Condition	Pitch Command ($^{\circ}$)	29	28
	SPL (dBA)	-	-
	Power (kW)	16.86	25.26
	Tip Mach	0.30	0.46
	RPM	786	1204

Figure 6.10: Prop-rotor blade designs at constant α of 1.0.Figure 6.11: Geometry of two rotor blade designs. Rotor A (black) with $\alpha = 1.0, \beta = 0.1$ and Rotor B (dark red) with $\alpha = 1.0, \beta = 0.9$.

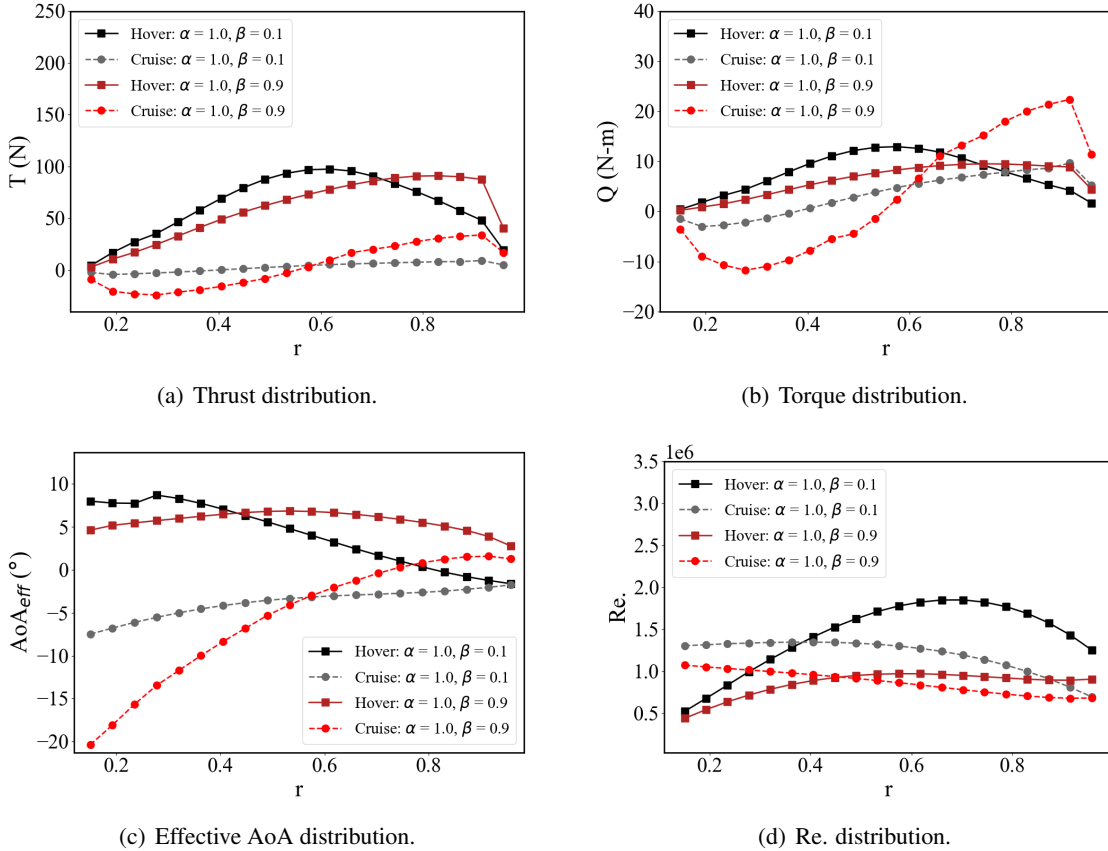


Figure 6.12: Performance of two rotor blade designs. Rotor A (black and gray) with $\alpha = 1.0, \beta = 0.1$ and Rotor B (dark red and red) with $\alpha = 1.0, \beta = 0.9$.

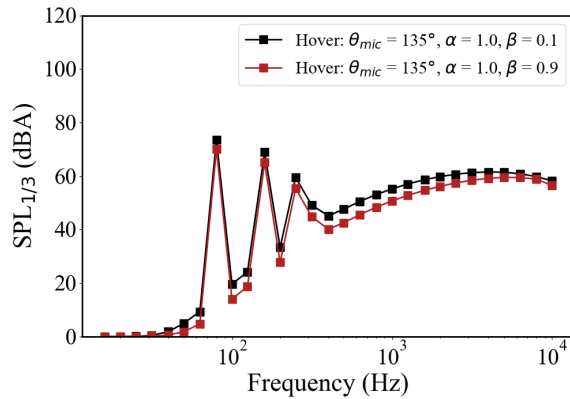


Figure 6.13: 1/3 Octave-band spectra of two rotor blade designs. Rotor A (black) with $\alpha = 1.0, \beta = 0.1$ and Rotor B (dark red) with $\alpha = 1.0, \beta = 0.9$.

6.6 Mission Simulation Case: Stopped-Rotor EVTOL Aircraft Touch-and-Go Mission

Despite the approaches outlined in prior sections to design optimal lift-rotors and prop-rotors are sufficient to move forward in the conceptual design stage of vehicle design, the simulation of their performance on an aircraft executing a mission profile will help to cement some of aforementioned conclusions. In this last section, the comparisons of energy consumption segment and maximum A-weighted sound pressure level for two lift-rotor blade designs of the stopped-rotor aircraft operating a the touch-and-go flight profile detailed in Chapter 5 is presented. After preliminary examination of the SPL_{Amax} contours, a decision was made to change the design point of the rotors in the optimization routine to reflect the most problematic regions of the radiated noise – rather than choosing hover as the design point, the blade loads corresponding altitude and freestream conditions were selected. Intuitively this is more practical as there is no use creating quite rotors in hover if the blade performance worst in the actually mission where there may be little to no hover period. And in fact, such a discovery was made in the initial attempts to optimize blades – the aircraft with lift-rotors designed for low noise in hover were indeed quieter at this design point but turned out be nosier than the aircraft with lift-rotors designed for high aerodynamic efficiency in the transition stages of flight.

The temporal snapshots presented in Figure 6.14 portray the radiated noise of the stopped rotor. The first column of snapshots correspond to an aircraft with lift-rotors designed for low-noise with an $\alpha = 0.0$ while the second column corresponds to an aircraft with lift-rotors designed for high efficiency where $\alpha = 1.0$. The design thrust used in the optimization was around 1600 N with a freestream velocity of 52 m/s or 116 mph. The evaluation point for the sound pressure level in the optimization was 40 ft measured from 175 degrees from the front rotor axis. This directivity angle corresponded to the aircraft with an angle of attack of 5° in the transition stage of flight. In the optimization, the tip radius and the hub cutout fraction were held fixed at 1.15m and 0.15 respectively implying that only changes in sectional twist, chord, sweep and thickness were permissible. Though the final designs are not presented below, the optimization times for the two

rotors was around 75 minutes each.

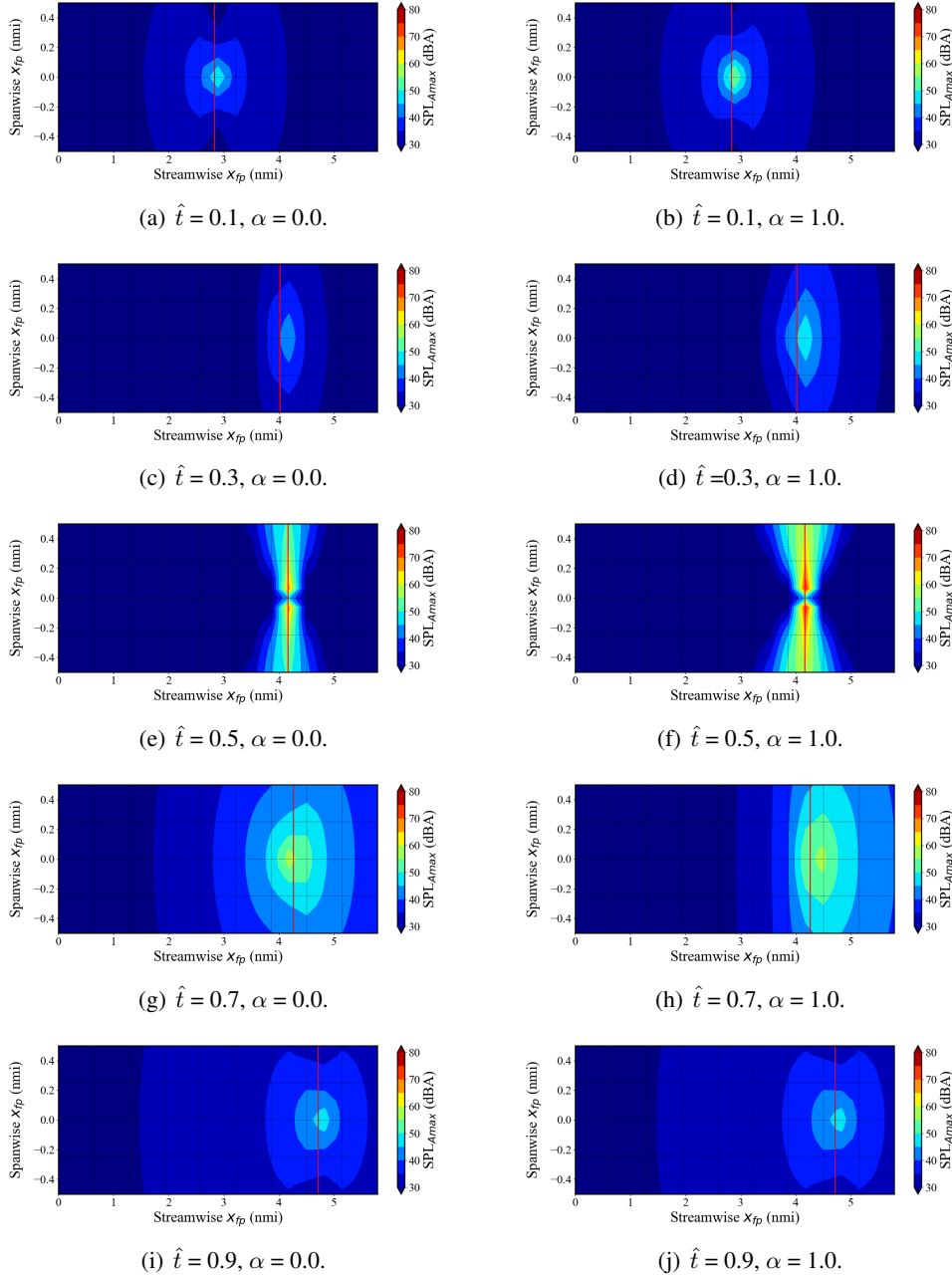


Figure 6.14: Touch-and-go noise contour comparisons of stopped-rotor aircraft with two different rotors of $\alpha = 0.0$ (left column) and 1.0 (right column).

From the naked eye alone, one can deduce from examining the two columns of contour plots that right images a larger acoustic noise footprint than those on the left. This is particularly evident at $\hat{t} = 0.5$ where the stopped-rotor is performing a vertical maneuver and as well as $\hat{t} = 0.7$ where the aircraft is picking up speed once again to climb. In the first instance, the more acoustically optimized aircraft whose 70 dBA line only reaches 0.08 nmi in Figure 6.14(e) compared to the aircraft with the high-performance blade produces a 70 dBA contour line that stretches to approximately 0.2 nmi in the lateral direction in Figure 6.14(f). In the second case instance, Figure 6.14(g) shows that the 60 dBA contour line spans about 1.2 nmi in major-diameter versus 4.4 nmi major-diameter observed in Figure 6.14(h). As the aircraft climbs and gains altitude, the differences in noise footprint diminish as the lift-rotor blades are throttled down and similar propeller blades are spun up to generate forward thrust.

The spider charts provided in Figures 6.15(a) to 6.15(f) gives up a more systems level perspective of the tradeoff between high-performance and low-noise design targets. Shown on the next page is an overview of five key metrics – Battery Temperature, Maximum A-weighted SPL, Maximum Power, Total Energy Consumption and Maximum Tip Mach – for the Approach Transition to Climb Transition segments. As previously stated, the Descent and Climb segments were omitted as no significant differences will be observed. Across the board, it can be seen that there is around a 10% reduction in noise in each segment. This decrease in noise however does come with penalties in performance. All segments see an increase in the maximum power drawn from the battery, in some instances, exceeding 110%. Additionally, for longer segments such as the vertical Vertical Descent and Vertical Hover, there is a significant increase in energy consumed. Such an observation tells us that either the design range of aircraft would decrease or more energy in the form of batteries are required to meet the originally specified range. Once again however, the additional battery mass would change trigger a change in design load, meaning a re-design of the rotors and a corresponding change in acoustics signature.

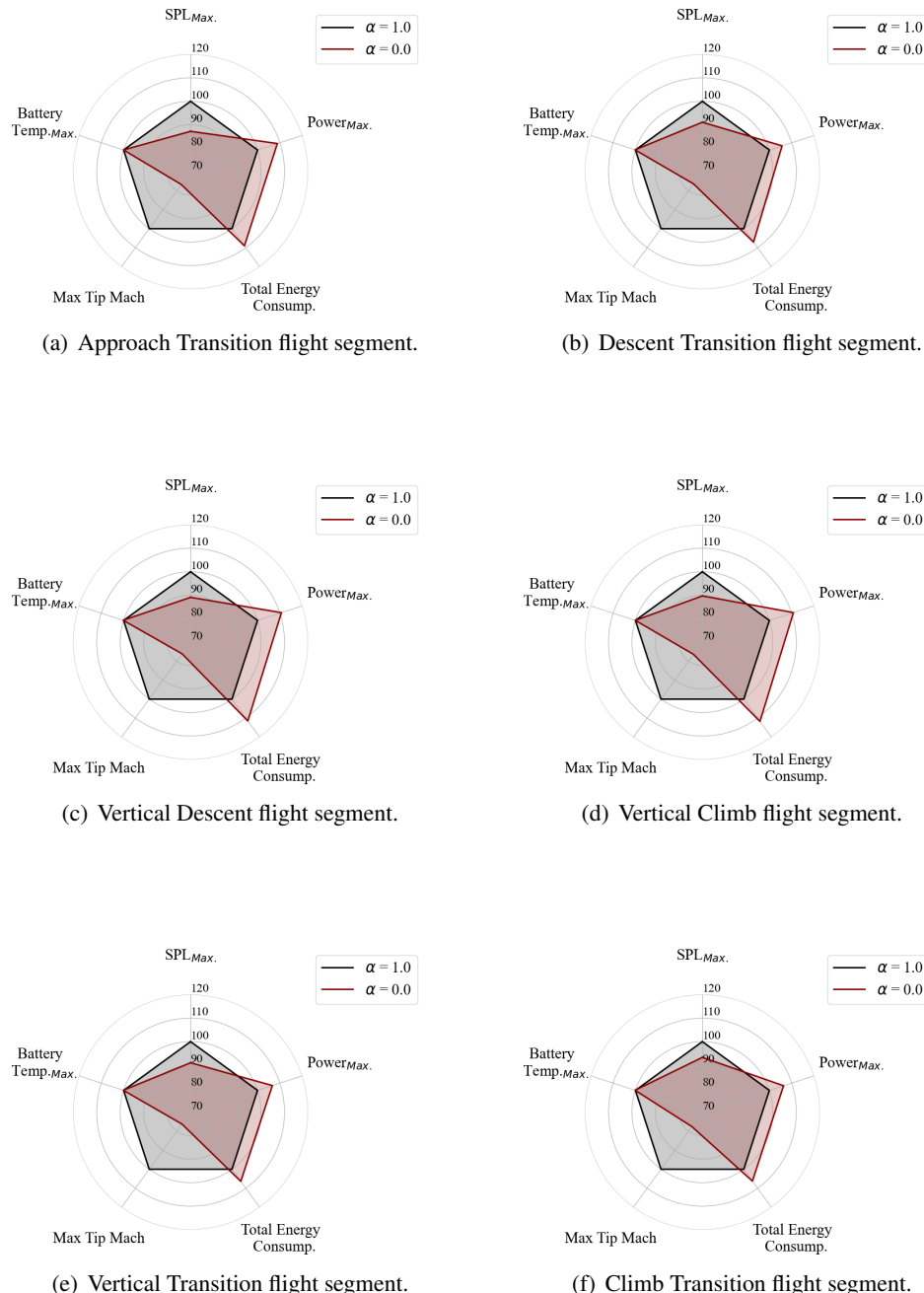


Figure 6.15: Comparisons of system performance of stopped-rotor aircraft with two different rotors of $\alpha = 1.0$ and 0.0 .

6.7 Chapter Summary

Bibliography

- [1] Portable Rechargeable Battery Business Division. Technical Information of NCR18650G. Technical Report 13H06BZGMIT, SANYO Electric Co., Ltd, . [retrieved 30 Jan. 2020].
- [2] Jack Moran. *An introduction to theoretical and computational aerodynamics*. Courier Corporation, 2003.
- [3] R. H. Schlinker and R. K. Amiet. Helicopter Rotor Trailing Edge Noise. Technical report, 1981.
- [4] D. Weir and J. Powers. Comparisons of predicted propeller noise with windtunnel and flyover data. 1987.
- [5] Matthew Clarke and Juan J Alonso. Lithium–ion battery modeling for aerospace applications. *Journal of Aircraft*, pages 1–13, 2021.
- [6] Roger Scherer. Blade design aspects. *Renewable Energy*, 16(1-4 -4 pt 2):1272–1277, 1999.
- [7] Colleen Reiche, Rohit Goyal, Adam Cohen, Jacqueline Serrao, Shawn Kimmel, Chris Fernando, and Susan Shaheen. Urban air mobility market study, 2018. [Retrieved 14 Nov. 2021].
- [8] National Academies of Sciences, Engineering, and Medicine and others. *Advancing aerial mobility: A national blueprint*. National Academies Press, 2020.

- [9] Rohit Goyal, Colleen Reiche, Chris Fernando, and Adam Cohen. Advanced air mobility: Demand analysis and market potential of the airport shuttle and air taxi markets. *Sustainability*, 13(13):7421, 2021.
- [10] E. Herman and M.A. Dymant. Urban air mobility-economics and global markets, 2018. [Retrieved 14 Nov. 2021].
- [11] Tom Major and Jono Anderson. Getting mobility off the ground;, 2019. [Retrieved 18 Nov. 2021].
- [12] Joseph N Robinson, Max-Daniel R Sokollek, Cedric Y Justin, and Dimitri N Mavris. Development of a methodology for parametric analysis of stol airpark geo-density. In *2018 Aviation Technology, Integration, and Operations Conference*, page 3054, 2018.
- [13] Uber. Fast-forwarding to a future of on-demand urban air transportation, 2016. [retrieved 23 Dec. 2020].
- [14] Robin Lineberger, Aijaz Hussain, Siddhant Mehra, and Deredk Pankratz. Elevating the future of mobility: Passenger drones and flying cars, 2018. [retrieved 20 Jul. 2021].
- [15] Bureau of Transportation Statistics. U.s. on-demand air taxi safety data, Oct 2020. [retrieved 15 Sep. 2021].
- [16] "BBC News". Uber's self-driving operator charged over fatal crash, Sep 2020. [retrieved 21 Jul. 2021].
- [17] Kevin R Antcliff, Mark D Moore, and Kenneth H Goodrich. Silicon valley as an early adopter for on-demand civil vtol operations. In *16th AIAA Aviation Technology, Integration, and Operations Conference*, page 3466, 2016.
- [18] Kevin Antcliff, Nicholas Borer, Sky Sartorius, Pasha Saleh, Robert Rose, Maxime Gariel, Joseph Oldham, Christopher Courtin, Marty Bradley, Satadru Roy, et al. Regional air mobility: Leveraging our national investments to energize the american travel experience. 2021.

- [19] Mark D Moore. Misconceptions of Electric Aircraft and their Emerging Aviation Markets. In *52nd Aerospace Sciences Meeting*, 2014.
- [20] John T Hwang and Andrew Ning. Large-scale multidisciplinary optimization of an electric aircraft for on-demand mobility. In *2018 AIAA/ASCE/AHS/ASC Structures, Structural Dynamics, and Materials Conference*, 2018.
- [21] Anna Straubinger, Raoul Rothfeld, Michael Shamiyah, Kai Daniel Büchter, Jochen Kaiser, and Kay Olaf Plötner. An overview of current research and developments in urban air mobility – Setting the scene for UAM introduction. *Journal of Air Transport Management*, 87(June), 2020.
- [22] Michael D. Patterson, Kevin R. Antcliff, and Lee W. Kohlman. A proposed approach to studying urban air mobility missions including an initial exploration of mission requirements. *Annual Forum Proceedings - AHS International*, 2018-May, 2018.
- [23] Federal Aviation Administration Advisory Council. Ac 150/5390-2: Heliport design, Apr 2012. [retrieved 30 Jan. 2020].
- [24] PA Henne. *Applied computational aerodynamics*, volume 125. AIAA, 1990.
- [25] Antony Jameson, Wolfgang Schmidt, and Eli Turkel. Numerical solution of the euler equations by finite volume methods using runge kutta time stepping schemes. In *14th fluid and plasma dynamics conference*, page 1259, 1981.
- [26] David Potter. Computational physics. 1973.
- [27] Bkam Van Leer. Towards the Ultimate Conservative Difference Scheme. V. A Second-Order Sequel to Godunov's Method. *Journal of Computational Physics*, 32:101–136, 1979.
- [28] Trent Lukaczyk, Andrew D. Wendorff, Emilio Botero, Timothy MacDonald, Timothy Mose, Anil Variyar, J. Michael Vegh, Michael Colonno, Thomas D. Economou, Juan J. Alonso, Tarik H. Orra, and Carlos Ilario da Silva. Suave: An open-source environment for multi-fidelity conceptual vehicle design. In *AIAA Aviation*, pages AIAA Paper 2015–3087, Dallas, TX, June 2015.

- [29] Emilio Botero, Andrew D. Wendorff, Timothy MacDonald, Anil Variyar, J. Michael Vegh, Juan J. Alonso, Tarik H. Orra, and Carlos Ilario da Silva. Suave: An open-source environment for conceptual vehicle design and optimization. In *54th AIAA Aerospace Sciences Meeting*, San Diego, CA, January 2016.
- [30] Timothy MacDonald, Matthew Clarke, Emilio M Botero, Julius M Vegh, and Juan J Alonso. Suave: an open-source environment enabling multi-fidelity vehicle optimization. In *18th AIAA/ISSMO Multidisciplinary Analysis and Optimization Conference*, page 4437, 2017.
- [31] Thomas D Economou, Francisco Palacios, Sean R Copeland, Trent W Lukaczyk, and Juan J Alonso. Su2: An open-source suite for multiphysics simulation and design. *Aiaa Journal*, 54(3):828–846, 2016.
- [32] Emilio M. Botero, Matthew A. Clarke, Racheal M. Erhard, Jordan T. Smart, Juan J. Alonso, and Aaron Blaufox. Aerodynamic Verification and Validation of SUAVE. pages 1–16, 2022.
- [33] Mark Drela and Harold Youngren. Athena Vortex Lattice. page 3, 2015.
- [34] David A Spera. Models of lift and drag coefficients of stalled and unstalled airfoils in wind turbines and wind tunnels. Technical report, 2008.
- [35] John J. Bertin and Russell M. Cummings. *Aerodynamics for Engineers Sixth Edition*, volume 6. Prentice Hall Upper Saddle River, NJ, 2015.
- [36] Joseph Katz and Allen Plotkin. *Low-Speed Aerodynamics*, volume 13. Cambridge University Press, 2001.
- [37] Leonardus Louis Maria Veldhuis. Propeller wing aerodynamic interference, 2005.
- [38] Fabrizio Nicolosi, Pierluigi Della Vecchia, and Salvatore Corcione. Design and aerodynamic analysis of a twin-engine commuter aircraft. *Aerospace Science and Technology*, 40:1–16, 2015.
- [39] Seung Yoo and Jared Duensing. Computational Analysis of the External Aerodynamics of the Unpowered X-57 Mod-III Aircraft. (June):1–18, 2019.

- [40] Mark Drela. Qprop formulation. 2006.
- [41] Mark Drela. Xfoil: An analysis and design system for low reynolds number airfoils. In *Low Reynolds number aerodynamics*, pages 1–12. Springer, 1989.
- [42] Racheal M Erhard and Juan J Alonso. A comparison of propeller wake models for distributed electric propulsion and evtol aircraft in complex flow conditions. In *AIAA SCITECH 2022 Forum*, page 1676, 2022.
- [43] Ohad Gur and Aviv Rosen. Comparison between blade-element models of propellers. *The Aeronautical Journal*, 112(1138):689–704, 2008.
- [44] John L Hess and A_M O Smith. Calculation of potential flow about arbitrary bodies. *Progress in Aerospace Sciences*, 8:1–138, 1967.
- [45] Bryan Thwaites. Approximate calculation of the laminar boundary layer. *Aeronautical Quarterly*, 1(3):245–280, 1949.
- [46] MR Head and P Bandyopadhyay. New aspects of turbulent boundary-layer structure. *Journal of fluid mechanics*, 107:297–338, 1981.
- [47] R Michel. Etude de la transition sur les profiles d'aile. Technical report, ONERA Report 1/1578-A., 1951.
- [48] Sukhvinder PS Badwal, Sarbjit S Giddey, Christopher Munnings, Anand I Bhatt, and Anthony F Hollenkamp. Emerging electrochemical energy conversion and storage technologies. *Frontiers in chemistry*, 2:79, 2014.
- [49] Richard Shepherd Shevell. *Fundamentals of flight*. Pearson Education India, 1989.
- [50] Jordan T Smart and Juan J Alonso. Primary weight estimation for evtols via explicit analysis and surrogate regression. In *AIAA Aviation*, pages AIAA Paper 2019–3679, 2019.
- [51] Emilio Botero, Matthew Clarke, Tim MacDonald, Julius Micheal Vegh, Trent Lukaczyk, Racheal Erhard, Carlos Roberto Ilário da Silva, Tim Momose, Aaron Blaufaux, Jordan Smart,

- Tarik Orra, Andrew Wendorff, and Juan Alonso. suavicode/suave: Suave 2.5.0, November 2021.
- [52] JE Ffowcs Williams and David L Hawking. Sound generation by turbulence and surfaces in arbitrary motion. *Philosophical Transactions for the Royal Society of London. Series A, Mathematical and Physical Sciences*, pages 321–342, 1969.
- [53] editor Hubbard, Harvey. Aeroacoustics of Flight Vehicles: Theory and Practice. Volume 2: Noise Control. *NASA Langley Research Center*, 1991.
- [54] editor Hubbard, Harvey. Aeroacoustics of Flight Vehicles: Theory and Practice. Volume 1: Noise Sources. Technical report, 1991.
- [55] Harvey H. Hubbard. Aeroacoustics of Flight Vehicles: Theory and Practice Volume 1: Noise Sources. *NASA Reference Publication*, 1(1258):610, 1991.
- [56] DB Hanson. Sound from a propeller at angle of attack: a new theoretical viewpoint. *Proceedings of the Royal Society of London. Series A: Mathematical and Physical Sciences*, 449(1936):315–328, 1995.
- [57] A Fm' Deming. Noise from propellers with symmetrical sections at zero blade angle. 1937.
- [58] L Gutin. On the sound field of a rotating propeller. *Physikalische Zeitschrit der Sowjetunion: Physical magazine of the Soviet Union volume 9 number 1*, 9(NACA-TM-1195), 1948.
- [59] IE Garrick and Charles E Watkins. A theoretical study of the effect of forward speed on the free-space sound-pressure field around propellers. 1953.
- [60] Robert A Arnoldi. *Propeller noise caused by blade thickness*. United Aircraft Corporation, Research Department, 1956.
- [61] Frank W Barry and Bernard Magliozzi. Noise detectability prediction method for low tip speed propellers. Technical report, United Technologies Corp Hamilton Standard Division, 1971.

- [62] Donald B. Hanson. Helicoidal surface theory for harmonic noise of propellers in the far field. *AIAA Journal*, 18(10):1213–1220, 1980.
- [63] Marvin E Goldstein. *Aeroacoustics*. 1976.
- [64] Thomas F. Brooks and Casey L. Burley. Rotor broadband noise prediction with comparison to model data. *7th AIAA/CEAS Aeroacoustics Conference and Exhibit*, 2001.
- [65] R. K. Amiet. Noise due to turbulent flow past a trailing edge. *Journal of Sound and Vibration*, 47(3):387–393, 1976.
- [66] Sicheng (Kevin) Li and Seongkyu Lee. Prediction of Urban Air Mobility Multirotor VTOL Broadband Noise Using UCD-QuietFly. *Journal of the American Helicopter Society*, 66(3):1–13, 2021.
- [67] Thomas F. Brooks, D. Stuart Pope, and Michael A. Marcolini. Airfoil self-noise and prediction. (August 1989), 2016.
- [68] Seongkyu Lee. Empirical wall-pressure spectral modeling for zero and adverse pressure gradient flows. *AIAA Journal*, 56(5):1818–1829, 2018.
- [69] Michael Goody. Empirical spectral model of surface pressure fluctuations. *AIAA journal*, 42(9):1788–1794, 2004.
- [70] Yannick Rozenberg, Gilles Robert, and Stéphane Moreau. Wall-pressure spectral model including the adverse pressure gradient effects. *AIAA journal*, 50(10):2168–2179, 2012.
- [71] M Kamruzzaman, D Bekirooulos, Th Lutz, W Würz, and E Krämer. A semi-empirical surface pressure spectrum model for airfoil trailing-edge noise prediction. *International Journal of Aeroacoustics*, 14(5-6):833–882, 2015.
- [72] M Ryan Catlett, Jason M Anderson, Jonathan B Forest, and Devin O Stewart. Empirical modeling of pressure spectra in adverse pressure gradient turbulent boundary layers. *AIAA Journal*, 54(2):569–587, 2016.

- [73] Harvey H Hubbard. Sound Measurements for Five Shrouded Propellers at Static Conditions. *National Advisory Committee for Aeronautics*, (April), 1950.
- [74] Nikolas S. Zawodny, Jr. Boyd, D. Douglas, and Casey L. Burley. Acoustic Characterization and Prediction of Representative, Small-Scale Rotary-Wing Unmanned Aircraft System Components. 2016.
- [75] Reda R. Mankbadi, Samuel O. Afari, and Vladimir V. Golubev. High-fidelity simulations of noise generation in a propeller-driven unmanned aerial vehicle. *AIAA Journal*, 59(3):1020–1039, 2021.
- [76] Kenneth S Brentner and Feridoun Farassat. Modeling aerodynamically generated sound of helicopter rotors. *Progress in aerospace sciences*, 39(2-3):83–120, 2003.
- [77] Chun Hern Tan, Keng Soon Voo, Wei Long Siauw, James Alderton, Amel Boudjir, and Fred Mendonça. CFD analysis of the aerodynamics and aeroacoustics of the NASA SR2 propeller, 2014.
- [78] James H Dittmar. Cruise Noise of the SR-2 Propeller Model in a Wind Tunnel. *Nasa Tm 101480*, (April 1989), 1989.
- [79] Theodore J Schultz. *Community noise rating*. Elsevier Applied Science, 1982.
- [80] Shashikant R More. *Aircraft noise characteristics and metrics*. PhD thesis, Purdue University, 2010.
- [81] National Institute of Advanced Industrial Science and Technology. [retrieved 03 Apr. 2022].
- [82] IRENA. Renewable power generation costs in 2020. *International Renewable Energy Agency*, page 160, 2021.
- [83] IEA. Global ev outlook 2020. *IEA*, 2020.
- [84] Andrea Cordoba-Arenas, Simona Onori, Yann Guezennec, and Giorgio Rizzoni. Capacity and power fade cycle-life model for plug-in hybrid electric vehicle lithium-ion battery cells

- containing blended spinel and layered-oxide positive electrodes. *Journal of Power Sources*, 278:473–483, 2015.
- [85] Alexandre Oudalov, Tilo Buehler, and Daniel Chartouni. Utility scale applications of energy storage. In *2008 IEEE Energy 2030 Conference*, pages 1–7. IEEE, 2008.
- [86] Mahammad A. Hannan, Md Murshadul Hoque, Aini Hussain, Yushaizad Yusof, and Pin Jern Ker. State-of-the-Art and Energy Management System of Lithium-Ion Batteries in Electric Vehicle Applications: Issues and Recommendations. *IEEE Access*, 6:19362–19378, 2018.
- [87] Domenico Di Domenico, Giovanni Fiengo, and Anna Stefanopoulou. Lithium-ion battery state of charge estimation with a kalman filter based on a electrochemical model. In *2008 IEEE International Conference on Control Applications*, pages 702–707. Ieee, 2008.
- [88] Gregory L. Plett. Extended Kalman filtering for battery management systems of LiPB-based HEV battery packs - Part 1. Background. *Journal of Power Sources*, 134(2):252–261, 2004.
- [89] Yasser Diab, François Auger, Emmanuel Schaeffer, and Moutassem Wahbeh. Estimating Lithium-Ion Battery State of Charge and Parameters Using a Continuous-Discrete Extended Kalman Filter. *Energies*, 10(8), 2017.
- [90] Hongwen He, Rui Xiong, and Jinxin Fan. Evaluation of lithium-ion battery equivalent circuit models for state of charge estimation by an experimental approach. *Energies*, 4(4):582–598, 2011.
- [91] Bernhard Schweighofer, Klaus M Raab, and Georg Brasseur. Modeling of high power automotive batteries by the use of an automated test system. *IEEE transactions on instrumentation and measurement*, 52(4):1087–1091, 2003.
- [92] Michael C Glass. Battery electrochemical nonlinear/dynamic spice model. In *IECEC 96. Proceedings of the 31st Intersociety Energy Conversion Engineering Conference*, volume 1, pages 292–297. IEEE, 1996.

- [93] Bolun Xu, Alexandre Oudalov, Andreas Ulbig, Göran Andersson, and Daniel S. Kirschen. Modeling of lithium-ion battery degradation for cell life assessment. *IEEE Transactions on Smart Grid*, 9(2):1131–1140, 2018.
- [94] Fabio Todeschini, Simona Onori, and Giorgio Rizzoni. An experimentally validated capacity degradation model for li-ion batteries in phevs applications. *IFAC Proceedings Volumes*, 45(20):456–461, 2012.
- [95] Caiping Zhang, Jiuchun Jiang, Linjing Zhang, Sijia Liu, Leyi Wang, and Poh Chiang Loh. A generalized SOC-OCV model for lithium-ion batteries and the SOC estimation for LNMCO battery. *Energies*, 9(11), 2016.
- [96] Marc Doyle, Thomas F Fuller, and John Newman. Modeling of galvanostatic charge and discharge of the lithium/polymer/insertion cell. *Journal of the Electrochemical society*, 140(6):1526, 1993.
- [97] Hongguang Sun and Regan Dixon. Development of cooling strategy for an air cooled lithium-ion battery pack. *Journal of Power Sources*, 272:404–414, 2014.
- [98] Jiateng Zhao, Zhonghao Rao, Yutao Huo, Xinjian Liu, and Yimin Li. Thermal management of cylindrical power battery module for extending the life of new energy electric vehicles. *Applied Thermal Engineering*, 85:33–43, 2015.
- [99] Tao Wang, K. J. Tseng, Jiyun Zhao, and Zhongbao Wei. Thermal investigation of lithium-ion battery module with different cell arrangement structures and forced air-cooling strategies. *Applied Energy*, 134:229–238, 2014.
- [100] Erik Alston, Shantha Jayasinghe, Craig Baguley, and Udaya Madawala. Thermal Management of an Electric Ferry Lithium-Ion Battery System. *2018 IEEE 4th Southern Power Electronics Conference, SPEC 2018*, pages 1–4, 2019.
- [101] Jens Vetter, Petr Novák, Markus Robert Wagner, Claudia Veit, K-C Möller, JO Besenhard, Martin Winter, Margret Wohlfahrt-Mehrens, Christoph Vogler, and Abderrezak Hammouche.

- Ageing mechanisms in lithium-ion batteries. *Journal of power sources*, 147(1-2):269–281, 2005.
- [102] Margret Wohlfahrt-Mehrens, Christian Vogler, and Jürgen Garche. Aging mechanisms of lithium cathode materials. *Journal of power sources*, 127(1-2):58–64, 2004.
- [103] Matthew Clarke, Jordan Smart, Emilio M. Botero, and Juan J Alonso. Strategies for Posing a Well-Defined Problem for Urban Air Mobility Vehicles. (January):1–14, 2019.
- [104] Yuan Zou, Xiaosong Hu, Hongmin Ma, and Shengbo Eben Li. Combined State of Charge and State of Health estimation over lithium-ion battery cell cycle lifespan for electric vehicles. *Journal of Power Sources*, 273:793–803, 2015.
- [105] Jeffrey C Chin, Sydney L Schnulo, Thomas B Miller, Kevin Prokopiis, and Justin Gray. "battery performance modeling on maxwell x-57". In *AIAA Scitech*, San Diego, CA, January 2019.
- [106] Mehmet Uğraş Cuma, Emrah Yirik, Çağla Dericioğlu, Erdem Ünal, Burak Onur, and M Tuğay. Design considerations of high voltage battery packs for electric buses. *Int. J. Adv. Automot. Technol.*, 1:73–79, 2017.
- [107] Dawn Bernardi, Ellen Pawlikowski, and John Newman. General Energy Balance for Battery Systems. *Electrochemical Society Extended Abstracts*, 84-2:164–165, 1984.
- [108] Dong Hyup Jeon and Seung Man Baek. Thermal modeling of cylindrical lithium ion battery during discharge cycle. *Energy Conversion and Management*, 52(8-9):2973–2981, 2011.
- [109] Rajib Mahamud and Chanwoo Park. Reciprocating air flow for li-ion battery thermal management to improve temperature uniformity. *Journal of Power Sources*, 196(13):5685–5696, 2011.
- [110] Venkat Srinivasan and CY Wang. Analysis of electrochemical and thermal behavior of li-ion cells. *Journal of The Electrochemical Society*, 150(1):A98, 2002.

- [111] Liwu Fan, JM Khodadadi, and AA Pesaran. A parametric study on thermal management of an air-cooled lithium-ion battery module for plug-in hybrid electric vehicles. *Journal of Power Sources*, 238:301–312, 2013.
- [112] Walter Van Schalkwijk and Bruno Scrosati. Advances in lithium ion batteries introduction. In *Advances in Lithium-Ion Batteries*, pages 1–5. Springer, 2002.
- [113] Said Al Hallaj, Hossein Maleki, Jong-Sung Hong, and J Robert Selman. Thermal modeling and design considerations of lithium-ion batteries. *Journal of power sources*, 83(1-2):1–8, 1999.
- [114] Qian Wang, Bin Jiang, Bo Li, and Yuying Yan. A critical review of thermal management models and solutions of lithium-ion batteries for the development of pure electric vehicles. *Renewable and Sustainable Energy Reviews*, 64:106–128, 2016.
- [115] Ralph E Williford, Vilayanur V Viswanathan, and Ji-Guang Zhang. Effects of entropy changes in anodes and cathodes on the thermal behavior of lithium ion batteries. *Journal of Power Sources*, 189(1):101–107, 2009.
- [116] Theodore L Bergman, Frank P Incropera, David P DeWitt, and Adrienne S Lavine. *Fundamentals of heat and mass transfer*. John Wiley & Sons, 2011.
- [117] D. Pastrascu. "Toyota Prius' Battery Recycling Plan, 2009. Accessed: 2020-05-14.
- [118] A Zukauskas et al. Heat transfer from tubes in cross flow. *Advances in heat transfer*, 8(1):93–160, 1972.
- [119] Madeleine Ecker, Nerea Nieto, Stefan Käbitz, Johannes Schmalstieg, Holger Blanke, Alexander Warnecke, and Dirk Uwe Sauer. Calendar and cycle life study of Li(NiMnCo)O₂-based 18650 lithium-ion batteries. *Journal of Power Sources*, 248:839–851, 2014.
- [120] Johannes Schmalstieg, Stefan Käbitz, Madeleine Ecker, and Dirk Uwe Sauer. A holistic aging model for Li(NiMnCo)O₂ based 18650 lithium-ion batteries. *Journal of Power Sources*, 257:325–334, 2014.

- [121] LH Saw, Yonghuang Ye, and AAO Tay. Electrochemical–thermal analysis of 18650 lithium iron phosphate cell. *Energy Conversion and Management*, 75:162–174, 2013.
- [122] Matthew A Clarke and Juan J Alonso. Evaluating the Performance and Acoustic Footprint of Aircraft for Regional and Urban Air Mobility. pages 1–31, 2021.
- [123] Charles N Adkins and Robert H. Liebeck. Design of optimum propellers. *Journal of Propulsion and Power*, 10(5):676–682, 1994.
- [124] J Michael Vegh, Emilio Botero, Matthew Clark, Jordan Smart, and Juan J Alonso. Current capabilities and challenges of ndarc and suave for evtol aircraft design and analysis. In *2019 AIAA/IEEE Electric Aircraft Technologies Symposium (EATS)*, pages 1–19. IEEE, 2019.
- [125] Wisk. Meet cora. discover the future., Jun 2020. [retrieved 6 Feb. 2021].
- [126] Acubed by Airbus. Welcome to vahana, Sep 2016. [retrieved 6 Feb. 2021].
- [127] Brian German, Matthew Daskilewicz, Thomas K Hamilton, and Matthew M Warren. Cargo Delivery in by Passenger eVTOL Aircraft: A Case Study in the San Francisco Bay Area. In *2018 AIAA Aerospace Sciences Meeting*, 2018.
- [128] Jon P Christophersen. Battery test manual for electric vehicles, revision 3. Technical report, Idaho National Lab.(INL), Idaho Falls, ID (United States), 2015.
- [129] Ezequiel Reyes Retana and Hugo Rodriguez-Cortes. Basic small fixed wing aircraft sizing optimizing endurance. In *2007 4th International Conference on Electrical and Electronics Engineering*, pages 322–325. IEEE, 2007.
- [130] Dale Lawrence and Kamran Mohseni. Efficiency analysis for long duration electric mavs. In *Infotech@ Aerospace*, page 7090. 2005.
- [131] Lance W Traub. Range and endurance estimates for battery-powered aircraft. *Journal of Aircraft*, 48(2):703–707, 2011.
- [132] Lance W. Traub, Emilio Botero, Rajmohan Waghela, Ryan Callahan, and Aaron Watson. Effect of taper ratio at low Reynolds number. *Journal of Aircraft*, 52(3):734–747, 2015.

- [133] Dieter Kraft. A software package for sequential quadratic programming. Technical report, DFVLR-FB 88-28, DLR German Aerospace Center – Institute for Flight Mechanics, Cologne, Germany, 1988.